

---

# Atypical Signals for Extra Dimensions at High Energy Colliders

---

A Thesis

Submitted to the  
TATA INSTITUTE OF FUNDAMENTAL RESEARCH, MUMBAI  
for the degree of DOCTOR OF PHILOSOPHY  
in PHYSICS

by

TOUSIK SAMUI

School of Natural Sciences  
Tata Institute of Fundamental Research  
Mumbai  
September, 2018  
Final Version Submitted in September, 2019



# Declaration

---

This thesis is a presentation of my original research work. Wherever contributions of others are involved, every effort is made to indicate this clearly, with due reference to the literature, and acknowledgement of collaborative research and discussions.

The work was done under the guidance of Professor Sreerup Raychaudhuri, at the Tata Institute of Fundamental Research, Mumbai.

Tousik Samui

(Tousik Samui)

Date: 26/09/2019

In my capacity as supervisor of the candidate's thesis, I certify that the above statements are true to the best of my knowledge.

Sreerup Raychaudhuri

(Prof. Sreerup Raychaudhuri)

Date: 26th September 2019



*to my parents*



# Contents

---

<b>List of Figures</b>	<b>v</b>
<b>List of Tables</b>	<b>vii</b>
<b>Acknowledgements</b>	<b>ix</b>
<b>List of Publications</b>	<b>xi</b>
<b>1 The Contemporary Case for Extra Dimensions</b>	<b>1</b>
1.1 One Extra Dimension: Unification of Long-range Forces . . . . .	1
1.1.1 Kaluza-Klein Modes . . . . .	2
1.2 Gauge Field Theories of Fundamental Interactions . . . . .	4
1.2.1 QED . . . . .	4
1.2.2 Non-Abelian gauge theories . . . . .	5
1.3 Construction of the Standard Model . . . . .	7
1.3.1 Strong interactions . . . . .	7
1.3.2 Electroweak interactions . . . . .	7
1.3.3 Electroweak symmetry-breaking . . . . .	8
1.3.4 The Hierarchy Problem . . . . .	10
1.3.5 Energy Momentum Tensor and Trace Anomaly . . . . .	12
1.4 Solving the Hierarchy Problem with Extra Dimensions . . . . .	14
1.4.1 Large Extra Dimensions . . . . .	14
1.4.2 Warped Extra Dimensions . . . . .	16
<b>2 Phenomenology of Extra Dimensions</b>	<b>19</b>
2.1 Einstein gravity in the weak-field limit . . . . .	19
2.2 Phenomenology of the ADD Model . . . . .	21
2.2.1 ADD Feynman rules . . . . .	21
2.2.2 ADD Mass Spectra of KK Modes . . . . .	26
2.2.3 Graviton Processes . . . . .	27
2.3 RS Model and Phenomenology . . . . .	29
2.3.1 RS Graviton . . . . .	29
2.3.2 Goldberger-Wise Stabilisation and the Radion . . . . .	30
<b>3 Mixed Higgs-Radion States at the LHC</b>	<b>35</b>
3.1 Introduction . . . . .	35
3.2 Radion-Higgs mixing . . . . .	37

3.3	Experimental Constraints . . . . .	41
3.4	Summary and Outlook . . . . .	48
<b>4</b>	<b>Radion Signals at the Conformal Point</b>	<b>51</b>
4.1	The Conformal Point . . . . .	51
4.2	Explaining the Erstwhile 750 GeV Resonance . . . . .	53
<b>5</b>	<b>LED Signals at the LHC</b>	<b>61</b>
5.1	Introduction . . . . .	61
5.2	Monojet + MET signals . . . . .	62
5.3	MET Signals in Association with $t\bar{t}$ . . . . .	63
5.3.1	Dilepton final states . . . . .	66
5.3.2	Single lepton final states . . . . .	68
5.3.3	Hadronic final states . . . . .	69
5.4	Correlation between monojet + MET and $t\bar{t}$ + MET . . . . .	71
5.5	Summary and Outlook . . . . .	72
<b>6</b>	<b>LED Signals at <math>e^+e^-</math> Colliders</b>	<b>75</b>
6.1	Introduction . . . . .	75
6.2	$t\bar{t}G_{\vec{n}}$ signal at the ILC . . . . .	76
6.2.1	Dilepton final states . . . . .	77
6.2.2	Single lepton final states . . . . .	78
6.2.3	Hadronic final states . . . . .	79
6.3	$t\bar{t}G_{\vec{n}}$ Signals at the CLIC . . . . .	80
6.4	Correlation between mono-photon + MET and $t\bar{t}$ + MET . . . . .	82
6.5	LED Signals at Very High Energy $e^+e^-$ Colliders . . . . .	83
6.6	Summary . . . . .	84
<b>7</b>	<b>Summary and Conclusions</b>	<b>85</b>
<b>A</b>	<b>Amplitudes for LED Signals at the LHC</b>	<b>87</b>
A.1	Radiated tensor graviton KK modes: . . . . .	87
A.2	Radiated Z boson: . . . . .	91
<b>B</b>	<b>Amplitudes for LED Signals at <math>e^+e^-</math> Colliders</b>	<b>95</b>
B.1	Radiated tensor graviton KK modes: . . . . .	95
B.2	Radiated Z boson: . . . . .	96
	<b>Bibliography</b>	<b>99</b>

# List of Figures

---

2.1	Feynman diagram of a process involving exchange of virtual KK states. . . . .	28
2.2	Branching fraction of lightest RS graviton in different decay channels. . . . .	30
3.1	The variation with $\xi$ of the mixing parameters . . . . .	39
3.2	The variation with $\xi$ of the scaling factors . . . . .	40
3.3	The variation of the predicted signal strengths with the mixing parameter $\xi$ . . . . .	42
3.4	Two-body branching ratios of the heavy scalar $\Phi$ . . . . .	43
3.5	Predictions of this model vis-á-vis LHC searches for a heavy ‘SM-like’ scalar . . . . .	45
3.6	Constraints from LHC data on the $\Lambda_\varphi$ - $M_\Phi$ plane . . . . .	46
3.7	Constraints from LHC data on the $\Lambda_\varphi$ - $\xi$ plane . . . . .	47
4.1	Branching ratios of the heavy scalar $\Phi$ in the neighbourhood of the conformal point . . . . .	52
4.2	Constraints on the conformal point $\xi_0$ . . . . .	53
4.3	Illustrating regions in the $c_\gamma$ - $c_g$ plane . . . . .	57
4.4	Cross-sections for diphoton production as a function of the radion vev $\Lambda_\varphi$ . . . . .	60
5.1	A sketch of representative subprocess for the process $pp \rightarrow jG_{\tilde{n}}$ . . . . .	62
5.2	Figure shows diagrams of the signal and background processes at the LHC. . . . .	64
5.3	Analysis of the $\ell^+\ell^- + \text{jets} + \text{MET}$ vis-á-vis background at the LHC . . . . .	67
5.4	Analysis of the $\ell^\pm + \text{jets} + \text{MET}$ signal vis-á-vis background at the LHC. . . . .	69
5.5	Analysis of the $\text{jets} + \text{MET}$ signal vis-á-vis background at the LHC. . . . .	70
5.6	Correlation plot showing events numbers for $\text{monojet} + \cancel{p}_T$ vs. $\ell^\pm + \text{jets} + \cancel{p}_T$ . . . . .	72
6.1	Tree-level Feynman diagrams for $e^+e^- \rightarrow t\bar{t}G_{\tilde{n}}$ . . . . .	76
6.2	Analysis of the $\ell^+\ell^- + \text{jets} + \text{MET}$ signal vis-á-vis background at the ILC. . . . .	78
6.3	Analysis of the $\ell^\pm + \text{jets} + \text{MET}$ signal vis-á-vis background at the ILC. . . . .	79
6.4	Analysis of the $\text{jets} + \text{MET}$ signal vis-á-vis background at a 1 TeV $e^+e^-$ collider. . . . .	80
6.5	Analysis of the signal vis-á-vis background at a 3 TeV $e^+e^-$ collider. . . . .	82
6.6	Analysis of the signal vis-á-vis background at a 3 TeV $e^+e^-$ collider. . . . .	82
6.7	Correlation plots for 1 TeV and 3 TeV machines. . . . .	83
6.8	Variation of cross-section as a function of machine energy for at an $e^+e^-$ collider. . . . .	84
A.1	Figure shows diagrams of the signal processes at the LHC. . . . .	87
A.2	Figure shows diagrams of the signal and background processes at the LHC. . . . .	92
B.1	Figure shows diagrams of the $t\bar{t}Z$ background processes at an $e^+e^-$ collider. . . . .	97



# List of Tables

---

1.1	Charges of lepton and quark fields. . . . .	8
3.1	LHC results on the Higgs signals strengths at 95% confidence level. . . . .	41
3.2	LHC 95% upper limits on the cross-section for a heavy scalar $S$ decaying to a $WW$ or a $ZZ$ pair. . . . .	44
5.1	Lower bound (in TeV) on $M_D$ for different values of extra dimensions $n$ from the LHC. . . . .	63
5.2	List of sets of cuts for $\ell^+\ell^- + \text{jets} + \text{MET}$ signal at $\sqrt{s} = 13$ TeV . . . . .	67
5.3	List of sets of cuts for $\ell^\pm + \text{jets} + \text{MET}$ signal at $\sqrt{s} = 13$ TeV. . . . .	68
5.4	List of sets of cuts for $\text{jets} + \text{MET}$ signal at $\sqrt{s} = 13$ TeV. . . . .	69
6.1	List of sets of cuts for $\ell^+\ell^- + \text{jets} + \text{MET}$ signal at $\sqrt{s} = 1$ TeV . . . . .	77
6.2	List of sets of cuts for $\ell^\pm + \text{jets} + \text{MET}$ signal at $\sqrt{s} = 1$ TeV. . . . .	78
6.3	List of sets of cuts for $\text{jets} + \text{MET}$ signal at $\sqrt{s} = 1$ TeV. . . . .	79
6.4	List of sets of cuts for three types of final states at $\sqrt{s} = 3$ TeV. . . . .	81



# Acknowledgements

---

I express my gratitude to all who have helped me in various ways during my Ph.D.

This part of my thesis is perhaps the most difficult one to write because, in these few years, I have received help and support from so many that it is difficult to remember all whom I should be thanking. Though I will try my best to be as exhaustive as possible, I would like to apologize in advance if I miss someone.

I would like to start by thanking my supervisor Professor Sreerup Raychaudhuri for his guidance and support. I learnt a lot of things from him during academic and non-academic interactions with him. I am also thankful to Dr. Tuhin Roy for many insightful discussions with him. I had very good collaborators during my Ph.D. I thank my collaborators Debjyoti Bardhan, Disha Bhatia, Amit Chakraborty and Ushoshi Maitra.

I was benefited by very good courses in TIFR and I would like to thank the instructors of the courses, including Profs. H.M. Antia, Amol Dighe, Gautam Mandal, Shiraz Minwalla, Sreerup Raychaudhuri and Sandip Trivedi.

I thank all the institute administrative members for their help whenever I needed it. I am really thankful to DTP's office members Raju N. Bathija, Aniket A. Surve, Mohan R. Shinde, Rajendra S. Pawar, Kapil S. Ghadiali, Ajay E. Salve and Girish V. Ogale for their help.

I am duly thankful to all my friends for encouraging me during my Ph.D. period. In TIFR, I enjoyed the wonderful company of Disha Bhatia, Shamik Bhattacharjee, Anirban Das, Chandan Ghosh, Manibrata Sen and many others. My friends outside TIFR also deserve acknowledgement. I would like to especially mention Satadru Bag, Sanjit De, Abira Dutta, Prasenjit Gayen, Bivash Kaity, Shinjini Ray for their support and encouragement.

I would also like to thank my childhood teacher Nimai Chandra Das from whom I learnt several important lessons, which helped me in many ways over the years.

Finally, I should mention the continuous support from my family, without which it would have been very difficult for me to pursue my Ph.D. at all. I especially thank my parents Asit Samui and Rupali Samui, sister Tayashri Samui, uncle Ranjit Samui, aunt Sushama Samui, and cousin Tapas Samui for their support towards my career in academics. In fact, I take this opportunity to acknowledge my family for always being supportive of whatever I do.

Tousik Samui



# List of Publications

---

PAPERS INCLUDED THIS THESIS:

1. **Mixed Higgs-Radion States at the LHC – a Detailed Study**  
Amit Chakraborty, Ushoshi Maitra, Sreerup Raychaudhuri, Tousik Samui  
[Nucl. Phys. B **922**, 41 (2017)]
2. **Radion Candidate for the LHC Diphoton Resonance**  
Debjyoti Bardhan, Disha Bhatia, Amit Chakraborty, Ushoshi Maitra, Sreerup Raychaudhuri, Tousik Samui  
[arXiv:1512.06674 [hep-ph]]
3. **Missing Energy Signals for Large Extra Dimensions in  $t\bar{t}$  Production at the LHC**  
Sreerup Raychaudhuri, Tousik Samui  
[In Preparation]
4. **Missing Energy Signals for Large Extra Dimensions in  $t\bar{t}$  Production at  $e^+e^-$  Colliders**  
Sreerup Raychaudhuri, Tousik Samui  
[In Preparation]



# CHAPTER 1

---

## The Contemporary Case for Extra Dimensions

---

### 1.1 One Extra Dimension : Unification of Long-range Forces

The idea of extra spacetime dimensions goes back to the early 20th century, when Nordström [1, 2], Kaluza [3] and Klein [4] first introduced it in the context of unification of gravitational and electromagnetic interactions – the two long-range interactions (and the only ones known in those days). The original Kaluza-Klein theory was motivated by Einstein’s theory of General Relativity where gravitational interactions are described by the geometrical features of the spacetime  $\mathbb{M}_4$  introduced by Minkowski. If an extra compact dimension is added to our known  $1 + 3$  spacetime dimensions (or 4D in short), then electromagnetic phenomena can also be explained as a characteristic of spacetime geometry. One thus has a *unified field theory* of both gravity and electromagnetism. For the simplest case, where the number of extra dimensions is unity, the compact extra dimension refers to a circle  $\mathbb{S}^1$ . Some general features which arise due to introduction of one circular extra dimension (or 5D in short) are discussed below.

In the following, we shall closely follow the notations and conventions of Ref. [5], viz.

- Greek indices for 4D, e.g.  $x^\mu$  with  $(\mu = 0, 1, 2, 3)$ .
- Upper case Latin indices for the full spacetime dimensions, including extra dimensions  $\vec{y} = \{y_1, y_2, \dots\}$ .
- A ‘hatted’ symbol (e.g.  $\hat{a}$ ) for a quantity in the full spacetime dimensions and ‘non-hatted’ (e.g.  $a$ ) for the corresponding 4D quantity.

As is usual in high energy physics, we shall set  $\hbar = c = 1$ .

The line element in a 5D space which is a simple extension of Minkowski space to  $\mathbb{M}_4 \times \mathbb{S}^1$ , can be written as

$$\begin{aligned} d\hat{s}^2 &= \eta_{\mu\nu} dx^\mu dx^\nu - dy^2 \\ &= \eta_{\mu\nu} dx^\mu dx^\nu - R_c^2 d\phi^2 \\ &\equiv \hat{g}_{MN} dx^M dx^N \end{aligned} \tag{1.1}$$

where  $\eta_{\mu\nu} = \text{diag}(1, -1, -1, -1)$  is the usual Minkowski metric in  $1 + 3$  dimension,  $0 \leq \phi < 2\pi$  is angular coordinate and  $R_c$  is the radius of the extra compact dimension, so that  $y = R_c\phi$ .

Introducing this one extra circular dimension, Kaluza and Klein showed that the Einstein-Hilbert action of General Relativity (GR)

$$\hat{S} = \frac{1}{16\pi\hat{G}_N} \int d^5x \sqrt{\hat{g}} \hat{\mathcal{R}} \quad (1.2)$$

in the 1+3+1 dimensional space  $(x^\mu, y)$ , in the limit  $R_c \rightarrow 0$  (called the *compactification limit*), can be decomposed as

$$\hat{S} \rightarrow \frac{2\pi R_c}{16\pi\hat{G}_N} \int d^4x \sqrt{-g} \mathcal{R} + \frac{2\pi R_c}{16\pi\hat{G}_N} \int d^4x \sqrt{-g} \left[ -\kappa^2 \frac{1}{4} F_{\mu\nu} F^{\mu\nu} \right] \quad (1.3)$$

where  $\hat{G}_N$  is the analogue of Newton's constant in five-dimension,  $\hat{\mathcal{R}}$  and  $\mathcal{R}$  are Ricci scalars in five and four-dimensions respectively,  $F_{\mu\nu} = \partial_\mu \hat{g}_{4\nu} - \partial_\nu \hat{g}_{4\mu}$  and  $\kappa$  is an adjustable constant. The first term is the action for the General Relativity in 4D while the second term is the action for 4D Maxwellian theory. Thus comparing with the usual action of electromagnetism it follows that the off-diagonal elements  $\hat{g}_{4\mu}$  of the metric tensor behave as the electromagnetic vector potential  $A_\mu$  and

$$\kappa^2 = \frac{16\pi\hat{G}_N}{2\pi R_c} = 16\pi G_N \quad \frac{\hat{G}_N}{2\pi R_c} = G_N \quad (1.4)$$

where  $G_N$  is Newton's constant in four-dimensional space.

It is clear from the above Kaluza-Klein reduction that the gravitational constant in 5D is different from the usual Newton constant in 4D and the difference is determined by the compactification radius  $R_c$ .

### 1.1.1 Kaluza-Klein Modes

If we consider a 5D scalar field,  $\hat{\Phi}(x^\mu, y)$  with mass  $M_0$ , the field should be periodic in the fifth dimension  $y$ , i.e.

$$\hat{\Phi}(x^\mu, y) = \hat{\Phi}(x^\mu, y + 2\pi R_c) \quad (1.5)$$

We can then expand  $\hat{\Phi}(x^\mu, y)$  as a Fourier series

$$\hat{\Phi}(x^\mu, y) = \sum_{n=0}^{\infty} \phi^{(n)}(x^\mu) e^{iny/R_c} \quad (1.6)$$

where the  $\phi^{(n)}(x^\mu)$  are Fourier coefficients. If, now, in this 5D bulk, the field  $\hat{\Phi}(x^\mu, y)$  satisfies Klein-Gordon equation

$$(\square - \partial_y^2 + M_0^2) \hat{\Phi}(x^\mu, y) = 0 \quad (1.7)$$

then substitution of the Eq. (1.6) gives a set of linearly independent equations

$$\left( \square + M_0^2 + \frac{n^2}{R_c^2} \right) \phi^{(n)}(x^\mu) = 0 \quad (1.8)$$

for all values of  $n$ . These fields  $\phi^{(n)}(x^\mu)$  are 4D scalar fields satisfying the Klein-Gordon equation and having masses

$$M_n = \sqrt{M_0^2 + \frac{n^2}{R_c^2}} \quad (1.9)$$

These 4D scalar fields are called *Kaluza-Klein modes* (KK modes) of the 5D scalar field  $\hat{\Phi}(x^\mu, y)$ . The mass of the KK modes increases monotonically with  $n$ . If the bulk mass is  $M_0 = 0$ , then these modes can still have mass except for the zero mode i.e.  $n = 0$ .

If we now consider a translation around the compact dimension  $y$

$$\begin{aligned} x^\mu &\rightarrow x'^\mu = x^\mu \\ y &\rightarrow y' = y + \kappa \xi(x^\mu) \end{aligned} \quad (1.10)$$

then the 5D scalar  $\hat{\Phi}(x^\mu, y)$  transforms as

$$\hat{\Phi}(x^\mu, y) \rightarrow \hat{\Phi}'(x^\mu, y) = \sum_0^\infty \phi^{(n)}(x^\mu) e^{in\{y - \kappa \xi(x^\mu)\}/R_c} = \sum_0^\infty \phi'^{(n)}(x^\mu) e^{iny/R_c} \quad (1.11)$$

where each KK mode  $\phi^{(n)}(x^\mu)$  transforms as

$$\phi'^{(n)}(x^\mu) = \phi^{(n)}(x^\mu) e^{-in\kappa \xi(x^\mu)/R_c} \quad (1.12)$$

This is clearly a gauge transformation of a charged 4D scalar field with charge

$$Q_n = n \left( \frac{\kappa}{R_c} \right) \quad (1.13)$$

In the original Kaluza-Klein formalism, we can identify  $\frac{\kappa}{R_c}$  to be the charge quantum  $e$  and this requirement, except for the zero mode, leads us to the condition that

$$\frac{1}{R_c} = \frac{e}{\kappa} = \sqrt{\frac{4\pi\alpha}{16\pi G_N}} \sim M_P \sim 10^{19} \text{ GeV} \quad (1.14)$$

where  $\alpha = \frac{e^2}{4\pi}$  is the fine structure constant. This means that all the KK modes – except the zero mode which gives Einstein gravity – lie at the Planck scale  $M_P$  and are not accessible to any experiments in the current and foreseeable future. Therefore, the only practical manifestations of the theory will be Einstein gravity and Maxwellian electrodynamics, both of which are well-tested as separate theories, but there is no way to test the unified theory or even the existence of an extra compact dimension. As a result, little progress was made in Kaluza-Klein theories during the rest of the twentieth century.

On the other hand, it was soon found that electrodynamics can be better understood in terms of a dynamical gauge symmetry of the action. Gauge symmetries extended to more complicated non-Abelian forms give us a formalism to understand the different non-gravitational interactions which appear in Nature in a systematic way. This framework is called the Standard Model (SM) of particle physics. However, the SM, though very successful in explaining the experimental results so far, has some theoretical problems when incorporated in a quantum field theory. Extra dimensions have been revived again to solve these problems in the gauge theory — such theories form the basis for a whole genre of contemporary research, including this thesis work. However, before taking up the current case for extra dimensions, we briefly review the SM and its most important aspects.

## 1.2 Gauge Field Theories of Fundamental Interactions

The simplest field theory of gauge interactions is the one that leads to Maxwell's equations in the classical case, and quantum electrodynamics (QED) when incorporated into a quantum theory. We review this first before going on to the SM. In this section, we consider only a 4D Minkowski space.

### 1.2.1 QED

The Dirac Lagrangian for a free (i.e. non-interacting) fermion with mass  $m$ , which can be written as

$$\mathcal{L}_0 = \bar{\psi}(x) (i\gamma^\mu \partial_\mu - m) \psi(x) \quad (1.15)$$

is invariant under a global phase transformation of the field

$$\psi(x) \rightarrow \psi'(x) = e^{iq\alpha} \psi(x) \quad (1.16)$$

where  $\alpha$  is the (constant) parameter of the transformation and  $q$  is a constant specific to the fermion  $\psi$ . This invariance guarantees that the set of all transformations obtained by varying  $\alpha$  form a Lie group, denoted by  $U(1)$ . By Nöther's Theorem, this symmetry then leads to the conservation of a current given by

$$J^\mu(x) = q\bar{\psi}(x)\gamma^\mu\psi(x) \quad (1.17)$$

with a constant charge given by

$$\int d^3\vec{x} J^0(x) = q \int d^3\vec{x} \bar{\psi}(x)\gamma^0\psi(x) \quad (1.18)$$

which is just  $q$  for a normalised field. The constant  $q$  is, therefore, the conserved  $U(1)$  charge of the fermion field.

The above global transformation requires instant transmission of information as the change must happen at every point in space simultaneously. This is in violation of special relativity. It is more realistic if the transformation were to be local, i.e.  $\alpha = \alpha(x)$ . This local transformation, however, does not keep the Lagrangian of Eq. (1.15) invariant, as an extra term is generated from  $\partial_\mu$  acting on  $\alpha(x)$ . However, we can still retain gauge invariance with the help of an additional vector field  $A_\mu$ , called a *gauge field* which transforms as

$$A_\mu \rightarrow A'_\mu = A_\mu + \partial_\mu\alpha \quad (1.19)$$

simultaneously with the fermion field  $\psi(x)$ . This can be used to define a covariant derivative

$$D_\mu = \partial_\mu - iqA_\mu \quad (1.20)$$

which then transforms as

$$D_\mu\psi(x) \rightarrow [D_\mu\psi(x)]' = e^{iq\alpha(x)} D_\mu\psi(x) \quad (1.21)$$

One can also show that the kinetic term of the gauge field

$$\mathcal{L} = -\frac{1}{4} F_{\mu\nu} F^{\mu\nu}, \quad (1.22)$$

where  $F_{\mu\nu} = \partial_\mu A_\nu - \partial_\nu A_\mu$ , is also invariant under the gauge transformation. Now, we can write the full QED Lagrangian for a fermion with mass  $m$  as

$$\mathcal{L} = \bar{\psi}(x) (i\gamma^\mu D_\mu - m) \psi(x) - \frac{1}{4} F_{\mu\nu} F^{\mu\nu} \quad (1.23)$$

which is invariant under the local gauge transformations for  $\psi(x)$  and  $A^\mu(x)$  simultaneously. We can expand the covariant derivative to write this in the form

$$\mathcal{L} = \mathcal{L}_0 - \frac{1}{4} F_{\mu\nu} F^{\mu\nu} + qJ^\mu(x)A_\mu(x) \quad (1.24)$$

where the first two terms on the right correspond to free fields and the last term is a *gauge interaction*. The Euler-Lagrange equations for this are

$$\partial_\mu F^{\mu\nu} = -qJ^\nu \quad (1.25)$$

which is identical in form with the Maxwell equations, and

$$i\gamma^\mu (\partial_\mu - iqA_\mu) \psi(x) - m\psi(x) = 0 \quad (1.26)$$

which is identical in form with the Dirac equation for a pointlike charged fermion in an electromagnetic field. To obtain a gauge theory of electromagnetism, we only have to identify the conserved Nöther charge  $q$  with the electric charge of the fermion and the gauge field  $A^\mu(x)$  with the electromagnetic four-potential. If we set  $q = -e$ , the quantum version of this theory will be QED, with the  $\psi$  and the  $A^\mu$  fields representing electron and photon respectively.

One important thing to notice is that the gauge field  $A^\mu$  cannot have a mass term,  $\frac{1}{2}M_A^2 A^\mu A_\mu$  since inclusion of such a mass term no longer keeps the Lagrangian gauge invariant. This is, of course, consistent with the well-known massless nature of the photon.

This elegant formalism thus enables us to develop the theory of the electromagnetic interaction from the principle of local gauge symmetry. Similarly, theories of the strong and weak interactions between elementary particles can also be developed from local gauge symmetries of a somewhat more complicated form, but with essentially the same structure.

### 1.2.2 Non-Abelian gauge theories

The idea of a gauge transformation and symmetry under the gauge transformation can be extended to more complicated cases. Suppose we have  $N$  degenerate Dirac fermions ( $\psi_1, \psi_2, \dots, \psi_N$ ), each with mass  $m$ . Now, as before, we write down the Lagrangian for this system of  $N$  free fermions as

$$\mathcal{L}_0 = \bar{\Psi}(x) (i\gamma^\mu \partial_\mu - m) \Psi(x) \quad (1.27)$$

where

$$\Psi = \begin{pmatrix} \psi_1 \\ \psi_2 \\ \vdots \\ \psi_N \end{pmatrix} \quad (1.28)$$

then, as before, a global  $N \times N$  unitary transformation on  $\Psi$  is

$$\Psi \rightarrow \Psi' = U\Psi \quad (1.29)$$

where the unitary matrix  $\mathbb{U}$  can be written in terms of a set of Hermitian generators  $\mathbb{T}_a$  ( $a = 1, 2, \dots, n$ ) as

$$\mathbb{U} = e^{ig\alpha_a \mathbb{T}_a} \quad (1.30)$$

with a summation over  $a$  implied, and the set of  $\alpha_a$  are constants. The constant  $g$  is analogous to  $q$  in the Abelian case and is known as the *coupling constant*. This transformation clearly keeps the Lagrangian invariant, which means that the set of  $\mathbb{U}$  matrices forms a Lie group, which is defined by the Lie algebra of generators

$$[\mathbb{T}_a, \mathbb{T}_b] = if_{abc} \mathbb{T}_c \quad (1.31)$$

where the  $f_{abc}$  are the structure constants. This symmetry then leads to a conserved Nöther current (or a set of Nöther currents)

$$J_a^\mu = g \bar{\Psi}(x) \mathbb{T}_a \gamma^\mu \Psi(x) \quad (a = 1, \dots, n) \quad (1.32)$$

and a set of constant Nöther charges

$$Q_a = \int d^3 \vec{x} J_a^0 = g \int d^3 \vec{x} \bar{\Psi}(x) \mathbb{T}_a \gamma^0 \Psi(x) . \quad (1.33)$$

As in the Abelian case, a local transformation with  $\mathbb{U} = \mathbb{U}(x)$  does not keep the Lagrangian invariant because it generates extra terms proportional to  $\partial_\mu \mathbb{U}$ . In this case, we again need to add gauge fields in order to retain the symmetry of the Lagrangian. Following the previous – Abelian – case, we replace  $\partial_\mu$  by a covariant derivative

$$\mathbb{D}_\mu = \mathbb{I} \partial_\mu - ig \mathbb{A}_\mu \quad (1.34)$$

where  $\mathbb{A}_\mu$  is a  $N \times N$  matrix transforming as

$$\mathbb{A}_\mu \rightarrow \mathbb{A}'_\mu = \mathbb{U}(x) \left[ \mathbb{A}_\mu - \frac{i}{g} \mathbb{U}^\dagger(x) \partial_\mu \mathbb{U}(x) \right] \mathbb{U}^\dagger(x) \quad (1.35)$$

so that the covariant derivative transforms as

$$\mathbb{D}_\mu \Psi(x) \rightarrow [\mathbb{D}_\mu \Psi(x)]' = \mathbb{U}(x) \mathbb{D}_\mu \Psi(x) \quad (1.36)$$

from which it is easy to see that the replacement  $\partial_\mu \rightarrow \mathbb{D}_\mu$  in Eq. 1.27 is sufficient to create a (local) gauge invariant Lagrangian.

Since the number of independent gauge fields should be the same as the number of free parameters of the transformation, it is usual to define  $\mathbb{A}_\mu(x) = A_\mu^a(x) \mathbb{T}_a$  and

$$\mathbb{F}_{\mu\nu}(x) = \frac{i}{g} [\mathbb{D}_\mu, \mathbb{D}_\nu] . \quad (1.37)$$

The gauge kinetic term can be written

$$\mathcal{L} = -\frac{1}{2} \text{Tr} (\mathbb{F}_{\mu\nu} \mathbb{F}^{\mu\nu}) \quad (1.38)$$

or, expanding  $\mathbb{F}^{\mu\nu} = F_a^{\mu\nu} \mathbb{T}_a$ ,

$$\mathcal{L} = -\frac{1}{4} \sum_a F_{\mu\nu}^a F^{\mu\nu,a} \quad (1.39)$$

where

$$F_{\mu\nu}^a = \partial_\mu A_\nu^a - \partial_\nu A_\mu^a + gf^{abc} A_\mu^b A_\nu^c \quad (1.40)$$

The gauge-invariant Lagrangian for this theory can now be written

$$\mathcal{L} = \bar{\Psi}(x) (i\gamma^\mu \mathbb{D}_\mu - m\mathbb{1}) \Psi(x) - \frac{1}{2} \text{Tr} (\mathbb{F}_{\mu\nu} \mathbb{F}^{\mu\nu}) \quad (1.41)$$

or,

$$\mathcal{L} = \mathcal{L}_0 - \frac{1}{2} \text{Tr} (\mathbb{F}_{\mu\nu} \mathbb{F}^{\mu\nu}) + gJ_a^\mu A_{\mu a} \quad (1.42)$$

where the gauge interactions are given by the last term.

It is noteworthy that, as in the Abelian case, the gauge fields have to be massless since a mass term for gauge fields would break gauge invariance. However, in the non-Abelian gauge theory the  $F^{\mu\nu}$  has bilinear terms in  $A_\mu^a A_\nu^b$  which, after expansion, leads to cubic and quartic self-couplings of the gauge fields, which do not appear in QED.

## 1.3 Construction of the Standard Model

The basis of the Standard Model is a non-Abelian local gauge theory as described above. The Standard Model Lagrangian is symmetric under the gauge group  $SU(3)_c \otimes SU(2)_L \otimes U(1)_Y$  where  $SU(3)_c$  is the gauge group of colour,  $SU(2)_L$  is the gauge group of weak interactions and  $U(1)_Y$  is the gauge symmetry corresponding to hypercharge.

### 1.3.1 Strong interactions

The gauge theory corresponding to the  $SU(3)_c$  group gives us a theory of the strong interaction and is known as Quantum Chromodynamics (QCD). The model assumes three generations of elementary fermions, called quarks  $q$ , which carry the corresponding gauge charges — called colour — and the gauge fields corresponding to this group are called gluons  $G$ . The gauge-invariant Lagrangian for QCD, then, can be written as

$$\mathcal{L}_{\text{QCD}} = \bar{q}_f (i\gamma^\mu \mathbb{D}_\mu - m_f) q_f - \frac{1}{4} G^{\mu\nu, a} G_{\mu\nu}^a \quad (1.43)$$

where the covariant derivative is

$$\mathbb{D}_\mu = \mathbb{I}\partial_\mu - ig_s \mathbb{K}^a G_\mu^a \quad (1.44)$$

with the  $\mathbb{K}^a = \frac{1}{2}\lambda_a$  being the 8 generators of the  $SU(3)_c$  group, in terms of the Gell-Mann matrices  $\lambda_a$ , and

$$G_{\mu\nu}^a = \partial_\mu G_\nu^a - \partial_\nu G_\mu^a + g_s f^{abc} G_\mu^b G_\nu^c \quad (1.45)$$

with  $g_s$  being the coupling constant of the strong interaction and  $f^{abc}$  being the appropriate structure constants. The subscript  $f$  represents a sum over six quark flavours, i.e.  $f = u, d, s, c, b, t$  in order of mass.

### 1.3.2 Electroweak interactions

The group  $SU(2)_L \otimes U(1)_Y$  corresponds to the Glashow-Salam-Weinberg model for electroweak unification. The  $SU(2)_L$  symmetry treats left-handed fermions differently from the right-handed

ones. The left-handed  $u$ -quark and  $d$ -quark forms an  $SU(2)_L$  doublet whereas the corresponding right-handed ones are singlet under the  $SU(2)_L$  group. The hypercharges for left-handed fields also differ from the right-handed fields, so that the electric charges, given by  $Q_f = T_3 + \frac{1}{2}Y$  remain the same for the left- and right-handed components. The electroweak interaction is also felt by the lepton sector which more-or-less follows the same pattern – with an important difference being the absence of right-handed neutrinos. The different gauge charge assignments of the Standard Model fields are shown in Table 1.1.

	$Q_L \equiv \begin{pmatrix} u_L \\ d_L \end{pmatrix}$	$u_R$	$d_R$	$E_L \equiv \begin{pmatrix} \nu_L \\ e_L \end{pmatrix}$	$e_R$
$SU(3)_C$	3	3	3	1	1
$SU(2)_L$	2	1	1	2	1
$U(1)_Y$	1/3	4/3	-2/3	-1	-2

Table 1.1: Charges of lepton and quark fields.

The Lagrangian for the electroweak part of the gauge theory is given by

$$\mathcal{L}_{\text{EW}} = \sum_f i\bar{\psi}_{fL}\gamma^\mu\mathbb{D}_\mu\psi_{fL} + \sum_f i\bar{\psi}_{fR}\gamma^\mu D_\mu\psi_{fR} - \frac{1}{4}W^{\mu\nu a}W_{\mu\nu}^a - \frac{1}{4}B^{\mu\nu}B_{\mu\nu} \quad (1.46)$$

where the sum over  $f$  runs over all quarks (see above) as well as all the leptons  $e, \mu, \tau, \nu_e, \nu_\mu, \nu_\tau$ . The kinetic terms for gauge bosons are given by

$$\begin{aligned} W_{\mu\nu}^a &= \partial_\mu W_\nu^a - \partial_\nu W_\mu^a + g\epsilon_{abc}W_\mu^b W_\nu^c \\ B_{\mu\nu} &= \partial_\mu B_\nu - \partial_\nu B_\mu \end{aligned} \quad (1.47)$$

and the gauge covariant derivatives for left- and right-handed fermions are given, respectively, by

$$\begin{aligned} \mathbb{D}_\mu &= \partial_\mu - ig\mathbb{T}_a W_\mu^a - ig'\frac{Y}{2}\mathbb{B}_\mu \\ D_\mu &= \partial_\mu - ig'\frac{Y}{2}B_\mu \end{aligned} \quad (1.48)$$

where  $\mathbb{T}_a = \frac{1}{2}\sigma_a$  and  $g, g'$  are coupling constants. The gauge bosons cannot have masses if the gauge invariance of the Lagrangian is to be maintained. Likewise, fermion mass terms will break the gauge invariance because the left- and right-handed fermions have different gauge charges — these are not demanded by the gauge theory, but have to be put in by hand to explain maximal parity violation in weak interactions. The above Lagrangian is, thus, a theory of massless particles – in fact, it has no parameter that can set a mass scale.

### 1.3.3 Electroweak symmetry-breaking

A model of massless elementary particles is clearly not realistic, for we have observed both fermions and vector bosons which are massive — in fact, in the case of the  $W$ 's and the  $t$  quark, very massive, i.e.  $\mathcal{O}(100m_p)$ . Such large masses cannot be explained away by introducing small perturbations to break the gauge symmetry, but require a different mechanism altogether. This is provided by a mechanism called *spontaneous symmetry-breaking*.

To achieve spontaneous breaking of the electroweak symmetry we require to augment the field content of the Standard Model with a  $SU(2)_L$  doublet of scalar fields with hypercharge  $Y = 1$ , viz.

$$\Phi(x) = \begin{pmatrix} \phi^+(x) \\ \phi^0(x) \end{pmatrix} = e^{ig\mathbb{T}_a G_a(x)} \begin{pmatrix} 0 \\ \frac{H(x)}{\sqrt{2}} \end{pmatrix} \quad (1.49)$$

where we choose a polar parametrisation of the scalar doublet. An  $SU(2)_L \otimes U(1)_Y$ -symmetric Lagrangian for this scalar doublet

$$\mathcal{L}_\Phi = (\mathbb{D}^\mu \Phi)^\dagger \mathbb{D}_\mu \Phi - V(\Phi) \quad (1.50)$$

where the covariant derivative is

$$\mathbb{D}_\mu = \mathbb{I}\partial_\mu - ig\mathbb{T}_a W_\mu^a - i\frac{g'}{2}\mathbb{I}B_\mu \quad (1.51)$$

and the  $V(\Phi)$  is

$$V(\Phi) = -\mu^2 \Phi^\dagger \Phi + \lambda (\Phi^\dagger \Phi)^2 \quad (1.52)$$

so that we have a doublet of massless scalars with a quadratic and a quartic self-coupling respectively, with positive coupling constants  $\mu^2$  and  $\lambda$ . We note that these self-couplings are not demanded by the gauge symmetry, but do not violate it either. The parameter  $\mu$  has the dimension of mass and introduces a mass scale into the theory. Both parameters are put in by hand.

Treating these interaction terms as a classical potential we find that the value  $\Phi = 0$  about which the perturbation expansion is to be made in a quantum field theory, is an unstable point, whereas the minima lie at

$$\langle \Phi^\dagger \Phi \rangle_0 = \frac{\mu^2}{2\lambda} \equiv \frac{v^2}{2} \quad (1.53)$$

Before quantising the theory, we should expand the scalar doublet about one of the minima, i.e. we should re-define fields

$$\tilde{\Phi} = \Phi - \langle \Phi \rangle_0 \quad (1.54)$$

This will clearly break the  $SU(2)_L$  symmetry by quantity proportional to  $v$ , which is not small, but determined by the choice of parameters  $\mu$  and  $\lambda$ .

With the benefit of hindsight, we can first make an  $SU(2)_L$  gauge transformation with parameters  $\alpha_a(x) = -G_a(x)$ , so that

$$\Phi(x) = \frac{H(x)}{\sqrt{2}} \quad (1.55)$$

In this specific gauge, called the *unitary gauge*, the scalar fields  $G_a(x)$  disappear and only the field  $h$  remains. The former are referred to as *Goldstone bosons* and the latter as a *Higgs boson*. We now have

$$\tilde{\Phi} = \begin{pmatrix} 0 \\ \frac{H(x)}{\sqrt{2}} \end{pmatrix} - \begin{pmatrix} 0 \\ \frac{v}{\sqrt{2}} \end{pmatrix} = \begin{pmatrix} 0 \\ \frac{h(x)}{\sqrt{2}} \end{pmatrix} \quad (1.56)$$

parametrising  $\langle\Phi\rangle_0$  suitably so that  $H = h + v$ . The Lagrangian in Eq. (1.50) now assumes the form

$$\begin{aligned}\mathcal{L}_\Phi &= \frac{1}{2}\partial_\mu h \partial^\mu h - \mu^2 h^2 - \lambda v h^3 - \frac{1}{4}\lambda h^4 \\ &+ \frac{1}{8}g^2(h+v)^2 (W_\mu^1 - iW_\mu^2)(W^{1\mu} + iW^{2\mu}) \\ &+ \frac{1}{8}(h+v)^2 \begin{pmatrix} W_\mu^3 & B_\mu \end{pmatrix} \begin{pmatrix} g^2 & -gg' \\ -gg' & g'^2 \end{pmatrix} \begin{pmatrix} W^{3\mu} \\ B^\mu \end{pmatrix}\end{aligned}\quad (1.57)$$

where now the quadratic interaction term for the scalar Higgs boson has disappeared – to be replaced by a mass term, with mass  $\sqrt{2}\mu$ . Moreover, the second line of Eq. (1.57) tells us that if we define charged gauge bosons fields

$$W_\mu^\pm \equiv \frac{1}{\sqrt{2}}(W_\mu^1 \mp iW_\mu^2)\quad (1.58)$$

we will get a mass term for the particle-antiparticle pair  $W^\pm$  which is

$$M_W = \frac{1}{2}gv\quad (1.59)$$

The last term in Eq. (1.57) is a mass-mixing term between the  $W_\mu^3$  and  $B_\mu$ . One can diagonalise the matrix and obtain the mass eigenstates

$$\begin{pmatrix} Z_\mu \\ A_\mu \end{pmatrix} = \begin{pmatrix} \cos\theta_W & -\sin\theta_W \\ \sin\theta_W & \cos\theta_W \end{pmatrix} \begin{pmatrix} W_\mu^3 \\ B_\mu \end{pmatrix}\quad (1.60)$$

with a mixing angle  $\tan\theta_W = g'/g$ , called the *Weinberg angle*. One of the mixed states, viz.  $A_\mu$  remains massless and the other vector field  $Z_\mu$  receives a mass  $M_Z = M_W \sec\theta_W$ . We note that all these vector boson fields are defined in the unitary gauge mentioned above.

This 1967 model of symmetry-breaking correctly reproduces QED as a low-energy effective theory at energies well below  $v$ , through the massless vector field  $A_\mu$ , which we identify with the photon. The weak interactions are correctly reproduced by the  $W^\pm$  and  $Z$  interactions, though historically, the  $Z$  boson-mediated interactions were discovered later (1973) as predictions of the theory. The  $W^\pm$  and  $Z$  boson themselves were discovered in the 1980s. Another major prediction of the theory was the physical scalar, or the Higgs boson  $h$ , which was discovered only recently in 2012. Its mass  $M_h = \sqrt{2}\mu$  was found to be very close to 125 GeV.

It may be noted before proceeding further that though the  $SU(2)_L$  and  $U(1)_Y$  were standalone symmetries in the massless model, the inclusion of scalars with self-couplings mixes them up and they break down jointly to  $U(1)_{\text{em}}$ , i.e. Maxwellian electrodynamics. This model, then is a genuine model of electroweak unification. The  $SU(3)_c$  symmetry, however, stays apart and unbroken, and the gluons remain massless.

### 1.3.4 The Hierarchy Problem

The mass of the Higgs boson, viz.  $M_h = 125$  GeV, made it accessible to the current generation of experiments and led to its discovery. However, it has been known for a long time that such a value of the Higgs mass leads to a deep theoretical problem when the Standard Model is

considered as a quantum field theory. As we have seen, the Higgs bosons  $h$  have a self-coupling term  $\frac{1}{4}\lambda h^4$  and this leads to one-loop self-energy corrections of the form

$$\delta M_h^2 = \lambda \Lambda^2 \oplus \lambda(\Lambda^2 + M_h^2) \ln \frac{\Lambda^2}{v^2} \oplus M_h^2 \ln \frac{M_h^2}{v^2} \oplus \dots \quad (1.61)$$

where  $\Lambda$  is the (presumably large) momentum cutoff of the Standard Model and the  $\oplus$  symbols denote linear combination with small numerical coefficients. This must be added on to the bare mass  $M_{h0} = \sqrt{2}\mu$  to get the physical Higgs boson mass, i.e.

$$M_h^2 = M_{h0}^2 + \delta M_h^2 \quad (1.62)$$

So far, there is no problem, for one can always choose the bare mass  $M_{h0}^2$  to cancel any large quantities in  $\delta M_h^2$ , as prescribed in textbooks for mass renormalisation of any quantum field theory. This prescription works well for gauge bosons and fermions, for once the divergent terms containing  $\Lambda$  are removed at the one-loop level, they do not appear at higher orders, a fact which can be traced to the existence of gauge and chiral symmetries (in the high energy limit) respectively which forbid the appearance of quadratic divergences. For an elementary scalar like the Higgs boson – the only one known – however, the quadratic divergence  $\lambda\Lambda^2$  is not only explicit, but it reappears at the two-loop level even after cancellation at the one-loop level by the bare mass. This phenomenon can be traced to the fact that no symmetry protects an elementary scalar mass in the high energy limit. If we tune the bare mass to cancel the total divergence at one loop, not only will the one-loop result become divergent and tachyonic, but yet another new divergence will appear at the three-loop level. As one cannot have more than one bare mass parameter, an order-by-order re-definition of the bare mass makes perturbation theory meaningless. It seems, then, that the mass of the Higgs boson will inexorably be drawn to the cutoff of the theory, i.e.  $M_h \approx \Lambda$ , in a quantum version of the Standard Model.

There will still be no problem if the cutoff  $\Lambda$  lies one to three orders of magnitude above  $M_h$ , for there can always be small coefficients involving the coupling constants and the loop factor  $(16\pi^2)^{-1}$ . However, if the cutoff lies much above this, i.e. there is a large hierarchy between  $M_h$  and  $\Lambda$ , it becomes difficult to keep  $M_h \simeq 125$  GeV in the quantum theory. This is known as the *hierarchy problem* in the Standard Model.

The next question is if we have any hint as to where the cutoff for the Standard Model lies. Here, from what is already known, we have four different possibilities.

- (a) If we assume that there are no new interactions among elementary particles, we will still have to include gravitation, which is left out of the Standard Model, as it is too weak at laboratory energies, to have any effect on the experimental results. The strength of gravity grows, however, with energy, and around a value  $M_P = G_N^{-1/2}$  it becomes as strong as the Standard Model interactions. At this energy, the excitations of spacetime itself, considered as a field, will have to be taken into account and hence,  $M_P$  will act as cutoff for the Standard Model. As  $M_P \sim 10^{19}$  GeV, this will make the hierarchy problem extremely acute.
- (b) If we consider the running of the Higgs self-coupling  $\lambda$ , purely within the Standard Model, it turns out that  $\lambda \rightarrow 0$  at an energy scale which varies from  $10^9$  GeV to  $M_P$ , depending on the choice of experimentally measured parameters used in the calculation. This would

destabilise the electroweak vacuum, leading to a catastrophic situation which we know has not occurred as the Universe cooled down from the Big Bang. The only way to avoid this is to have some new phenomena occurring at a fairly high scale, say,  $10^{10}$  GeV, which would then be the cutoff for the Standard Model, and make the hierarchy problem very acute.

- (c) If the strong interactions do unify with the electroweak interactions in some way, we would get a *grand unified theory* (GUT). If the GUT scale is  $\Lambda_{\text{GUT}}$ , we would predict proton decay to non-baryons with a lifetime  $\tau_p \sim \Lambda_{\text{GUT}}^{-1}$ . Current experimental lower bounds on  $\tau_p$  push up  $\Lambda_{\text{GUT}} \sim 10^{17}$  GeV, which is not far from the Planck scale. Once again, such a cutoff would make the hierarchy problem serious.
- (d) The extremely small masses of neutrinos, and the surprising non-observance of lepton number violation in the neutrino sector can be understood if there exist additional very heavy neutrinos which mix with the known ones, driving their mass eigenvalues to very small values. The masses of these heavy neutrinos can be anything from  $10^4$  GeV to  $10^{10}$  GeV. If these are indicative of new physics at the corresponding energy scale, this will serve as a cutoff for the Standard Model. In this case, too, there will be a hierarchy problem. Even though perhaps not as acute as the previous three cases, this cutoff is still too large to be accommodated by any reasonable combination of coupling constants and loop factors.

It is clear, then, that the hierarchy problem in the Standard Model is a serious one, and cannot be removed by any kind of redefinitions within the Standard Model itself. Some new physics is required to prevent the Higgs boson mass from shooting up to the cutoff scale. There are many different ideas for this, including compositeness and supersymmetry, but the one considered in this work will be a revival of the original ideas of Kaluza and Klein in a way which bring the Planck scale itself down to a few TeV or tens of TeV. These are described in the next section.

### 1.3.5 Energy Momentum Tensor and Trace Anomaly

An important aspect of this thesis will be the coupling of gravity with the Standard Model fields, which occurs through the energy-momentum tensor  $T^{\mu\nu}$  corresponding to the Standard Model fields. This is simply the Nöther current corresponding to Poincaré invariance of the Standard Model Lagrangian.

The simplest way to calculate the symmetric gauge-invariant energy-momentum tensor  $T^{\mu\nu}$  is to couple the gauge-invariant Standard Model Lagrangian  $\mathcal{L}_{\text{SM}}$  with an arbitrary metric  $g_{\mu\nu}$  and then calculate

$$T_{\text{SM}}^{\mu\nu} = \left[ -2 \frac{\delta \mathcal{L}_{\text{SM}}}{\delta g_{\mu\nu}} + g^{\mu\nu} \mathcal{L}_{\text{SM}} \right]_{g_{\mu\nu} = \eta_{\mu\nu}} \quad (1.63)$$

One may now calculate the energy-momentum tensor in the unitary gauge as

$$\begin{aligned}
T_{\text{SM}}^{\mu\nu} = & - \sum_f (\bar{\psi}_f (\gamma^\mu D^\nu + \gamma^\nu D^\mu) \psi_f + \eta^{\mu\nu} \bar{\psi}_f (i\mathcal{D} - m_f) \psi_f) \\
& + \sum_A \left( F^{\mu\beta} F_\beta^\nu - \frac{1}{4} \eta^{\mu\nu} F^{\alpha\beta} F_{\alpha\beta} - M_A^2 A^\mu A^\nu + \frac{1}{2} \eta^{\mu\nu} M_A^2 A^\alpha A_\alpha \right) \\
& - D^\mu h D^\nu h + \frac{1}{2} \eta^{\mu\nu} D^\alpha h D_\alpha h - \frac{1}{2} \eta^{\mu\nu} M_h^2 h^2
\end{aligned} \tag{1.64}$$

where the  $\psi_f$  are generic fermion fields, the  $A$  are generic gauge fields and the  $h$  is the Higgs scalar.

A particularly interesting scenario is invariance of a theory under a scale transformation  $x^\mu \rightarrow x'^\mu = e^\sigma x^\mu$  whose infinitesimal form

$$x^\mu \rightarrow x'^\mu = 1 + \sigma x^\mu \tag{1.65}$$

is like a translation of coordinates, i.e. within the set of Poincaré transformations. The conserved current can be calculated as

$$j^\mu = T^{\mu\nu} x_\nu \tag{1.66}$$

and is called the *dilatation current*. It follows that

$$\partial_\mu j^\mu = \partial_\mu (T^{\mu\nu} x_\nu) = T_\mu^\mu \tag{1.67}$$

which is the trace of the energy-momentum tensor. One may now calculate the trace of  $T_{\text{SM}}^{\mu\nu}$  as

$$(T_{\text{SM}})_\mu^\mu = \sum_A M_A^2 A^\mu A_\mu + \sum_f m_f \bar{\psi}_f \psi_f - 2M_h^2 h^2. \tag{1.68}$$

showing that the unbroken gauge theory with massless particles is a scale-invariant theory.

The above results, derived for the SM as a classical theory, does not hold when we consider the corresponding quantum field theory. This can be easily understood from the fact that couplings without any classical mass dimensions run as the scale changes. The running of the coupling constants go as

$$\frac{\partial g(t)}{\partial \ln t} = \beta(g) \tag{1.69}$$

i.e.

$$g(t) = \int^t \beta(g) d \ln t' \tag{1.70}$$

where  $t$  is the scale at which  $g$  is calculated and  $\beta(g)$  is the corresponding beta function. For an infinitesimal scaling  $x^\mu \rightarrow e^\sigma x^\mu$

$$g \rightarrow g + \sigma \beta(g) \tag{1.71}$$

and the corresponding change in the Lagrangian is

$$\mathcal{L} \rightarrow \mathcal{L} + \sigma \beta(g) \frac{\partial}{\partial g} \mathcal{L} \tag{1.72}$$

This immediately implies that this change in the Lagrangian will contribute an extra term – called the *trace anomaly* – to the right side of Eq. (1.67).

If we calculate from the Lagrangian with this prescription, the energy-momentum tensor will be neither symmetric nor gauge invariant. However, one can easily rescale  $A_\mu \rightarrow \frac{1}{g}A_\mu$  to bring all the  $g$  dependence to the gauge kinetic term

$$\mathcal{L} = -\frac{1}{4g^2}F^{\alpha\beta}F_{\alpha\beta} \quad (1.73)$$

This automatically gives a gauge invariant trace anomaly

$$\mathcal{A}_T = \frac{\beta(g)}{2g^3}F^{\alpha\beta}F_{\alpha\beta} \quad (1.74)$$

We need to rescale  $A_\mu \rightarrow gA_\mu$  again, so that, the gauge fields are consistent with the Eq. (1.68). The trace anomaly term finally reads as

$$\mathcal{A}_T = \frac{\beta(g)}{2g}F^{\alpha\beta}F_{\alpha\beta} \quad (1.75)$$

Without loss of generality, we can extend this analysis to all the gauge groups in the Standard Model, obtaining

$$\mathcal{A}_T = \frac{\beta(g')}{2g'}B^{\alpha\beta}B_{\alpha\beta} + \frac{\beta(g)}{2g}W^{\alpha\beta a}W_{\alpha\beta}^a + \frac{\beta(g_s)}{2g_s}G^{\alpha\beta a}G_{\alpha\beta}^a \quad (1.76)$$

As the beta functions in the Standard Model are well-known, calculation of the trace anomaly is a straightforward business.

## 1.4 Solving the Hierarchy Problem with Extra Dimensions

The only new scale achievable in the Kaluza-Klein theory was, as we have seen, the Planck scale, and this arose from the identification of the charge quantum  $\kappa/R_c$  with  $e$ , the coupling constant of electromagnetism. Insofar as the original Kaluza-Klein theory was a unified theory of gravity and electromagnetism, no other choice was possible. However, with the development of gauge field theory, there was no further need to identify the off-diagonal block of the metric tensor with the electromagnetic field, or the charge quantum  $\kappa/R_c$  with electric charge  $e$ . This realisation inspired the development of the so-called *brane-world models*, some aspects of whose experimental realisations form the theme of this thesis. The first of these was the model with *large extra dimensions*, proposed by Arkani-Hamed, Dimopoulos and Dvali (1998) [6, 7], which goes by the name ‘ADD model’. An improved variant was a model with a *warped extra dimension*, proposed (1999) by Randall and Sundrum [8, 9], which goes by the name ‘RS model’. Countless variations of these original models have been proposed in the literature, but the essential features of all these are borrowed from either the one or the other. In this section, both the ideas are explained in brief.

### 1.4.1 Large Extra Dimensions

The idea of ADD was simply the introduction of  $n$  extra compact dimensions similar to the Kaluza-Klein theory. Each of the  $n$  extra dimensions has the topology of a circle and together they form a  $n$ -torus. If each of these circles has radius  $R_c$ , the line element of the free space will be

$$d\hat{s}^2 = \eta_{\mu\nu}dx^\mu dx^\nu - R_c^2(d\phi_1^2 + d\phi_2^2 + \dots + d\phi_n^2) \equiv \hat{g}_{MN}dx^M dx^N \quad (1.77)$$

where  $\eta_{\mu\nu} = \text{diag}(1, -1, -1, -1)$  and  $0 \leq \phi_i < 2\pi$  are angular coordinates of the extra dimensions. Distortions of the off-diagonal components of  $\hat{g}_{MN}$  are not identified with any known interaction field, and hence, there is no theoretical constraint on the value of  $R_c$ . The ADD construction envisages values of  $R_c$  as large as a millimetre, or a tenth of a millimetre. However, there exist stringent experimental constraints from experiments, including the ones at the LHC, which seem to confirm the 4D Standard Model to a high degree of precision to energy scales of a TeV or more, i.e. length scales as small as  $10^{-20}$  m, and seem to rule out the possibility of millimetre-sized extra dimensions. It is, therefore, postulated that the  $(4+n)$ -dimensional space has a 4D topological defect – a vortex, or a domain wall, or a  $D$ -brane of string theory – and that the Standard Model fields are confined to this 4D subspace. The whole  $(4+n)$ -dimensional space is called the *bulk* while the 4D subspace supporting the Standard Model fields is called the *brane*.

We now take up the question of why the ADD construction requires the assumption of large extra dimensions (LED) of the size of a millimetre or so. This is because this would solve the hierarchy problem in the Standard Model. To see this we start, as in the Kaluza-Klein theory, from the 4D Einstein-Hilbert action of general relativity

$$S = \frac{\bar{M}_P^2}{2} \int d^4x \sqrt{|g|} \mathcal{R} \quad (1.78)$$

where  $\bar{M}_P = M_P/\sqrt{8\pi}$  is the reduced Planck mass and  $\mathcal{R}$  is the 4D Ricci scalar. In the  $(4+n)$ -dimensional space, or the bulk, the Einstein-Hilbert action will be

$$\hat{S} = \hat{K} \int d^{4+n}x \sqrt{|\hat{g}|} \hat{\mathcal{R}} \quad (1.79)$$

where  $d^{4+n}x = d^4x d^n\vec{y}$ . We need to determine the constant factor  $\hat{K}$  in Eq. (1.79). Since the action is invariant under general coordinate transformations, we can choose coordinates which have the dimension of length, in which case, the mass dimensions of different quantities involved in the action are given by  $[\hat{g}_{MN}] = [\hat{g}] = 0$  and  $[\hat{\mathcal{R}}] = 2$ . Now, in order for the action to be dimensionless we need

$$[\hat{K}] = 2 + n \quad (1.80)$$

In analogy with the 4D action, we identify

$$\hat{K} = \frac{M_D^{2+n}}{2(2\pi)^n} \quad (1.81)$$

where  $M_D$  is the bulk Planck scale – or sometimes, string scale. For an  $n$ -torus, the volume of the extra dimensional space is given by

$$\int d^n\vec{y} = (2\pi R_c)^n \quad (1.82)$$

and the bulk action can be written as

$$\hat{S} = \frac{M_D^{2+n}}{2(2\pi)^n} \int d^{4+n}x \sqrt{|\hat{g}|} \hat{\mathcal{R}} \quad (1.83)$$

$$= \frac{M_D^{2+n} R_c^n}{2} \int d^4x \sqrt{|g|} \mathcal{R} \quad (1.84)$$

Comparing Eq. (1.78) with the first term in Eq. (1.84) leads to

$$M_D^{2+n} = \frac{M_P^2}{8\pi R_c^n} \quad (1.85)$$

which relates the bulk Planck mass  $M_D$  to the 4D Planck mass  $M_P$ . This bulk Planck scale plays the role of the cutoff  $\Lambda$  for the Standard Model in this scenario, for at these energies gravity becomes strong in the bulk and these effects will manifest in the brane as well. Thus, we can have a solution to hierarchy problem if we can bring the bulk Planck scale  $M_D$  to be in the range of a TeV, or a few tens of TeV. For this we must choose the size of the compact dimensions as

$$R_c \sim 10^{\frac{30}{n}-17} \text{ cm} \left( \frac{1 \text{ TeV}}{M_D} \right)^{1+\frac{2}{n}} \quad (1.86)$$

If we put  $M_D \sim 1 \text{ TeV}$ , then  $R_c \sim 10^{13} \text{ cm}$  for  $n = 1$ , which is not acceptable since this will modify the laws of gravity at the scale of solar system ( $1 \text{ A.U.} \simeq 1.5 \times 10^{13}$ ). For  $n = 2$ , however,  $R_c \sim 0.1 \text{ mm}$ , which is barely acceptable, since modern gravity experiments puts bounds on the length of extra dimensions  $R_c \leq 30 \mu\text{m}$  [10], but it becomes acceptable if we set  $M_D \simeq 1.7 \text{ TeV}$ . If  $n > 2$ , the permissible values of  $R_c$  are perfectly consistent with pure gravity experiments, for  $M_D \sim \text{TeV}$  or more. Thus, with these caveats in mind, it is perfectly possible to have  $M_D$  of a few TeV or more, providing an automatic cutoff for the Standard Model and hence ameliorating the hierarchy problem. This ingenious idea is called the *ADD model*.

### 1.4.2 Warped Extra Dimensions

Though startling in its simplicity and elegance, the ADD model has a basic fault. It works perfectly if gravity is considered as a classical background field, but the moment we allow gravity to become dynamical and assume quantisation, it turns out that large compact dimensions are unstable under radiative corrections and collapse to the Planck length  $R_c \sim M_P^{-1}$ , sending  $M_D$  shooting up to  $M_P$  and reinstating the original hierarchy problem.

A more subtle idea, which improves on the simple ADD Model was proposed by Randall and Sundrum (RS). This solution also relies on bringing down the bulk Planck scale to a scale near to  $M_h$ . The proposed solution is again introduction of one extra spatial dimension with a non-factorizable geometry, being a circle folded about a diameter ( $\mathbb{S}^1/\mathbb{Z}_2$ ). The line element in this space is taken as (see below)

$$d\hat{s}^2 = e^{-2\mathcal{K}R_c\phi} \eta_{\mu\nu} dx^\mu dx^\nu - R_c^2 d\phi^2 \equiv \hat{g}_{MN} dx^M dx^N \quad (1.87)$$

where  $R_c$  is again the radius of the extra dimension and  $\mathcal{K}$  is a constant curvature of the order of Planck scale. We see that the 4D Minkowski metric  $\eta_{\mu\nu}$  is multiplied by a ‘warp’ factor  $e^{-2\mathcal{K}R_c\phi}$ , and hence this is often called a *warped* extra-dimensional model. The  $\mathbb{Z}_2$  orbifolding with  $\mathbb{S}^1$  corresponds to the symmetry associated with the transformation

$$\phi \rightarrow \phi + 2\pi, \quad \phi \rightarrow -\phi \quad (1.88)$$

The points  $\phi = 0$  and  $\phi = \pi$  are the fixed points under these transformations, and, in the 5D bulk, represent topological defects, where it is natural to place two different branes, each with some kind of matter confined on it. The mass parameter on the brane located at  $\phi = 0$  does not

get warped while the mass parameter on the brane located at  $\phi = \pi$  gets warped by a factor  $e^{-\pi\mathcal{K}R_c}$ . Hence these branes are called ultraviolet (UV) and infrared (IR) branes respectively. The Standard Model fields are confined to the IR brane.

If we now take the usual action for a Higgs field  $h$  in the bulk

$$S_h = \int d^5x \sqrt{\hat{g}} \left[ \frac{1}{2} \hat{g}^{\mu\nu} \partial_\mu h \partial_\nu h - \mu^2 h^2 - \frac{\lambda}{4} h^4 \right] \quad (1.89)$$

this appears as a normal Higgs action on the UV brane, but on the IR brane, it becomes

$$S_h = \int d^4x \left[ e^{-2\pi\mathcal{K}R_c} \frac{1}{2} \eta^{\mu\nu} \partial_\mu h \partial_\nu h - e^{-4\pi\mathcal{K}R_c} \mu^2 h^2 - e^{-4\pi\mathcal{K}R_c} \frac{\lambda}{4} h^4 \right] \quad (1.90)$$

In order to get the kinetic term in canonical form we need to renormalise the scalar field by a transformation  $h \rightarrow e^{\pi\mathcal{K}R_c} h$ , which gives

$$S_h = \int d^4x \left[ \frac{1}{2} \partial^\mu h \partial_\mu h - e^{-2\pi\mathcal{K}R_c} \mu^2 h^2 - \frac{\lambda}{4} h^4 \right] \quad (1.91)$$

It follows that the vev of the the Higgs field and its mass, which appear in the bulk as  $v_0 = \sqrt{\mu^2/\lambda}$  and  $M_{h0} = \sqrt{2\mu}$  will appear on the IR brane as

$$v = e^{-\pi\mathcal{K}R_c} \sqrt{\frac{\mu^2}{\lambda}}, \quad \text{and} \quad M_h = e^{-\pi\mathcal{K}R_c} \sqrt{2\mu} \quad (1.92)$$

If we can now tune  $\mathcal{K}R_c \simeq 11.6$ , we can bring down the Higgs mass scale  $\mu$  which is  $\sim M_P$  in this model, to  $\sim \text{TeV}$ . We have already seen that quantum corrections on a bare mass around  $M_P$  will keep it in the same ballpark. The physical mass, after inclusion of all corrections, will then get ‘warped down’ on the IR brane to the observed value. In fact, any mass scale, including a Planck-scale cutoff for the theory will get similarly ‘warped down’, so that a high-scale cutoff of the theory will appear on the IR brane as a TeV-scale cutoff. This gives a nice solution to the hierarchy problem in the SM without having any parameter which is unnaturally large or small.

The RS solution obtained above depends crucially on having a metric of the form exhibited in Eq. (1.87). The metric can be obtained from the solution of Einstein’s equations in the bulk with a negative cosmological constant  $\hat{\Lambda}$ . It also needs the existence on the two branes of brane-localized 4D cosmological constants  $V_0$  and  $V_\pi$  at  $\phi = 0$ , and  $\phi = \pi$  respectively. The 5D bulk action becomes

$$\hat{S} = \int d^5x \left[ \sqrt{\hat{g}} \left( -\hat{\Lambda} + 2\hat{M}^3 \hat{\mathcal{R}} \right) + \sqrt{-\hat{g}_0} V_0 \delta(\phi) + \sqrt{-\hat{g}_\pi} V_\pi \delta(\phi - \pi) \right] \quad (1.93)$$

where  $\hat{g}_0, \hat{g}_\pi$  are the induced metric on the two UV and IR branes respectively,  $\hat{M}$  is the 5D bulk Planck mass and  $\hat{\mathcal{R}}$  is 5-dimensional Ricci scalar. Einstein’s equations for the above action are

$$\sqrt{\hat{g}} \left( \hat{\mathcal{R}}_{MN} - \frac{1}{2} \hat{g}_{MN} \hat{\mathcal{R}} \right) = -\frac{1}{4\hat{M}^3} \left[ \hat{\Lambda} \sqrt{\hat{g}} \hat{g}_{MN} + V_0 \hat{g}_{0,\mu\nu} \delta_M^\mu \delta_N^\nu \delta(\phi) + V_\pi \hat{g}_{\pi,\mu\nu} \delta_M^\mu \delta_N^\nu \delta(\phi - \pi) \right] \quad (1.94)$$

If we take an ansatz for the metric which obeys Poincaré invariance

$$ds^2 = e^{-2A(\phi)} \eta_{\mu\nu} dx^\mu dx^\nu + R_c^2 d\phi^2 \quad (1.95)$$

then the equations for  $A(\phi)$  are

$$\frac{6A'}{R_c^2} = -\frac{\hat{\Lambda}}{4\hat{M}^3} \quad (1.96)$$

$$\frac{3A''}{R_c^2} = \frac{V_0}{4\hat{M}^3 R_c} \delta(\phi) + \frac{V_\pi}{4\hat{M}^3 R_c} \delta(\phi - \pi) \quad (1.97)$$

The solution to Eq. (1.96), consistent with the orbifold symmetry, is

$$A(\phi) = \mathcal{K} R_c |\phi| \quad (1.98)$$

where  $\mathcal{K} = \sqrt{-\frac{\hat{\Lambda}}{24\hat{M}^3}}$ . and, from Eq. (1.97) we get

$$V_0 = -V_\pi = \sqrt{-24\hat{\Lambda}\hat{M}^3} \quad (1.99)$$

These relations between the boundary and bulk cosmological constant are required to obtain the solution for the metric. We note that  $\Lambda < 0$  in order to get a real curvature  $\mathcal{K}$ , and this makes the bulk an anti-de Sitter space, usually denoted  $\text{AdS}_5$ .

The RS model, therefore, also requires a fine tuning – at the classical level – of the cosmological constants in the bulk and on the two branes. The minimal model does not seek to find a dynamical explanation of this. The viability of the model also depends crucially on the exact tuning  $\mathcal{K}R_c \simeq 11.6$ , any deviation from which would cause large changes in the Higgs boson mass. A dynamical explanation of this will be discussed in the next chapter.

## CHAPTER 2

---

# Phenomenology of Extra Dimensions

---

We now consider the models of extra dimensions introduced in the previous chapter and investigate their phenomenological consequences. We first discuss some generic features of 4D Einstein gravity, which are reflected in higher-dimensional theories. We then take up the model of large extra dimensions, where  $n$  compact spatial extra dimensions were introduced. Finally we go on to the RS model, with a warped extra dimension, which has similar features, but also important differences.

### 2.1 Einstein gravity in the weak-field limit

Though most of the material in this section is to be found in any textbook on General Relativity, the discussions in this section closely follow the discussions of Refs. [5, 11].

The 4D invariant action of General Relativity, in the presence of matter fields, is given by

$$S = \frac{1}{\kappa^2} \int d^4x \sqrt{-g} \mathcal{R} + \int d^4x \sqrt{-g} \mathcal{L}_m \quad (2.1)$$

where  $\kappa^2 = 16\pi G_N$  and  $\mathcal{R}$  is the Ricci Scalar. By varying the action, we get Euler-Lagrange equations of motion which are the Einstein equations

$$\mathcal{R}_{\mu\nu} - \frac{1}{2}g_{\mu\nu}\mathcal{R} = \frac{\kappa^2}{\sqrt{-g}} \left[ \frac{\partial(\sqrt{-g}\mathcal{L}_m)}{\partial g_{\alpha\beta}} - \partial_\lambda \frac{\partial(\sqrt{-g}\mathcal{L}_m)}{\partial(\partial_\lambda g_{\alpha\beta})} \right] g_{\alpha\mu} g_{\beta\nu} \equiv -\frac{\kappa^2}{2} T_{\mu\nu} \quad (2.2)$$

where  $T_{\mu\nu}$  is the energy-momentum tensor and is given by Eq. (1.63). Multiplying by  $g^{\mu\nu}$  both the sides of Eq. (2.2) and summing over  $\mu$  and  $\nu$  indices, we get a relation between  $\mathcal{R}$  and the trace of the energy-momentum tensor

$$\mathcal{R} = \frac{\kappa^2}{2} T^\alpha{}_\alpha \quad (2.3)$$

and then substituting the value of  $\mathcal{R}$  in Eq. (2.2), we get

$$\mathcal{R}_{\mu\nu} = -\frac{\kappa^2}{2} \left( T_{\mu\nu} - \frac{1}{2}g_{\mu\nu}T^\alpha{}_\alpha \right) \equiv -\frac{\kappa^2}{2} S_{\mu\nu} \quad (2.4)$$

If the matter density  $S_{\mu\nu}$  is not very large, the right side can be treated perturbatively, and the metric will be nearly flat and constant and can be expanded around a constant background

metric. Since, in practice, the physical world can be described very well by Minkowski metric, the background metric can be taken to be  $\eta_{\mu\nu}$ . So,

$$g_{\mu\nu} = \eta_{\mu\nu} + \kappa h_{\mu\nu} + \mathcal{O}(\kappa^2) \quad (2.5)$$

where  $\kappa$  is the parameter for expansion. This is known as the *weak field approximation*. One can easily see that the value of  $\kappa = \sqrt{16\pi G_N} \sim 10^{-19} \text{ GeV}^{-1}$  is indeed small compared to the energy scale currently available in present day experiments, and therefore, the weak-field approximation is justified.

Now, using this, the Ricci tensor and Ricci scalar can be computed as

$$\mathcal{R}_{\mu\nu} = \frac{1}{2}\kappa \left[ \partial_\mu \partial_\nu h + \square h_{\mu\nu} - \partial_\mu \partial_\lambda h_\nu^\lambda - \partial_\lambda \partial_\nu h_\mu^\lambda \right] + \mathcal{O}(\kappa^2) \quad (2.6)$$

$$\mathcal{R} = \kappa \left[ \square h - \partial_\mu \partial_\nu h^{\mu\nu} \right] + \mathcal{O}(\kappa^2) \quad (2.7)$$

where  $h = h^\mu{}_\mu = \eta^{\mu\nu} h_{\mu\nu}$ , and, therefore, Einstein's equation can be written as

$$\square h_{\mu\nu} + \partial_\mu \partial_\nu h - \partial_\mu \partial_\lambda h_\nu^\lambda - \partial_\lambda \partial_\nu h_\mu^\lambda = -\kappa S_{\mu\nu} \quad (2.8)$$

This is a linear inhomogeneous differential equation of second order in  $h_{\mu\nu}$ , but obviously, finding a Green's function for it is extremely difficult. Fortunately, the equations can be simplified using a standard trick.

We note that under an infinitesimal coordinate transformation

$$x^\mu \rightarrow x'^\mu = x^\mu + \xi^\mu(x) \quad (2.9)$$

the metric transforms as

$$g_{\mu\nu} \rightarrow g'_{\mu\nu} = \frac{\partial x^\alpha}{\partial x'^\mu} \frac{\partial x^\beta}{\partial x'^\nu} g_{\alpha\beta} \quad (2.10)$$

which gives

$$h_{\mu\nu} \rightarrow h'_{\mu\nu}(x') = h_{\mu\nu}(x) - \partial_\mu \xi_\nu(x) - \partial_\nu \xi_\mu(x) \quad (2.11)$$

This looks exactly like a gauge transformation and it is straightforward to show that the action is indeed invariant under this transformation (as it should be). Now, we simply choose a gauge which will simplify the equation of motion for the field  $h_{\mu\nu}$ , just as we choose the Lorenz gauge in electromagnetism. Thus, we choose the harmonic or *de Donder gauge*

$$\partial_\lambda h^\lambda{}_\nu - \frac{1}{2} \partial_\nu h = 0 \quad (2.12)$$

which will simplify the Eq. (2.8) as

$$\square h_{\mu\nu} = -\kappa S_{\mu\nu} \quad (2.13)$$

which is the familiar inhomogeneous wave equation. In absence of matter fields, the equation reduces to free field equation for  $h_{\mu\nu}$

$$\square h_{\mu\nu} = 0 \quad (2.14)$$

The solution to the equation can be obtained as the plane wave solution

$$h_{\mu\nu}(x) = N_k \left[ \epsilon_{\mu\nu}(k) e^{ik \cdot x} + \epsilon_{\mu\nu}^*(k) e^{-ik \cdot x} \right] \quad (2.15)$$

One can show that out of 10 independent component of  $\epsilon_{\mu\nu}$  only two components are independent. Such gravity waves have been recently observed by the LIGO Collaboration and are, therefore, experimentally established.

In this work, however, our interest lies in a quantum description of gravity. So, we start with the Lagrangian of General Relativity which can be written, in the weak-field limit, as

$$\frac{1}{\kappa^2} \sqrt{-g} \mathcal{R} = \frac{1}{4} \left( \partial^\mu h_{\alpha\beta} \partial_\mu h^{\alpha\beta} - \partial^\mu h \partial_\mu h - 2\partial^\mu h_{\mu\alpha} \partial_\nu h^{\nu\alpha} + 2\partial^\mu h_{\mu\alpha} \partial^\alpha h \right) \quad (2.16)$$

which is known as the Fierz-Pauli approximation. The Euler-Lagrange equation for the above action is then

$$\square \left( h_{\mu\nu} - \frac{1}{2} h \eta_{\mu\nu} \right) = 0 \quad (2.17)$$

The equation reduces to previously obtained equation,  $\square h_{\mu\nu} = 0$ , for the fluctuation of metric  $h_{\mu\nu}$  if we can set  $h = 0$ . This can be obtained by redefining  $h_{\mu\nu} \rightarrow h_{\mu\nu} - \frac{1}{4} h \eta_{\mu\nu}$ . Now, we can quantise the fluctuation of the metric as we do in a gauge theory with addition of gauge fixing term and ghost terms. The quanta of the fluctuation of spin-2 metric,  $h_{\mu\nu}$  is called graviton. Also, we assume that the Feynman rules can be derived from the interaction Lagrangian like the other theories.

It is known that the quantisation of  $h_{\mu\nu}$  involves many subtle issues like non-renormalisability etc. These will not be discussed in this work and we only assume that we can quantise the theory. For our purpose, we do not go beyond the tree-level and hence issues arising due to loop corrections will be, as it were, swept under the carpet.

## 2.2 Phenomenology of the ADD Model

### 2.2.1 ADD Feynman rules

We now extend our discussion to the ADD model with  $n$  extra dimensions. Before starting the discussion on the ADD model per se, we write the metric for linearised gravity in higher dimensions as follows

$$\hat{g}_{MN} = \hat{\eta}_{MN} + \hat{\kappa} \hat{h}_{MN} \quad (2.18)$$

where  $\hat{\eta}_{MN} = \text{diag.}(1, -1, -1, \dots, -1)$  and the fluctuation of the metric can be written as

$$\hat{h}_{MN} = V_n^{-1/2} \left( \begin{array}{c|c} h_{\mu\nu} + \phi \eta_{\mu\nu} & A_{\mu i} \\ \hline A_{i\nu} & \phi_{ij} \end{array} \right) \quad (2.19)$$

where  $V_n$  is the volume of the extra dimensional space,  $\phi = \phi_{ii}$  and  $A_{\mu i}$  are off-diagonal elements of the metric, which are like vector fields in the 4D world – as was considered in the original Kaluza-Klein theory. Now, the Ricci tensor and Ricci scalar can be calculated and once again, we can write Fierz-Pauli Lagrangian in the bulk as

$$\frac{1}{\hat{\kappa}^2} \sqrt{|\hat{g}|} \hat{\mathcal{R}} = \frac{1}{4} \left( \partial^M \hat{h}_{AB} \partial_M \hat{h}^{AB} - \partial^M \hat{h} \partial_M \hat{h} - 2\partial^M \hat{h}_{MA} \partial_N \hat{h}^{NA} + 2\partial^M \hat{h}_{MA} \partial^A \hat{h} \right) \quad (2.20)$$

The equation of motion for  $\hat{h}_{MN}$  is

$$\hat{\square} \left( \hat{h}_{MN} - \frac{1}{2} \hat{h} \eta_{MN} \right) = 0 \quad (2.21)$$

where  $\hat{h} = \hat{\eta}^{MN} \hat{h}_{MN} = \eta^{\mu\nu} h_{\mu\nu} + 4\phi - 2\phi_{ii} = h + 2\phi$ . The above equation with a gauge condition  $\hat{h} = 0$  can be reduced to

$$\begin{aligned}\hat{\square} \left( h_{\mu\nu} - \frac{1}{2} h \eta_{\mu\nu} \right) &= 0 \\ \hat{\square} A_{\mu i} &= 0 \\ \hat{\square} \phi_{ij} &= 0\end{aligned}\tag{2.22}$$

for different components in the  $\hat{h}_{MN}$ . These fields can be expanded as Fourier series on a  $n$ -torus as

$$h_{\mu\nu}(x, y) = \sum_{\vec{n}} h_{\mu\nu}^{(\vec{n})}(x) e^{i\vec{n}\cdot\vec{\phi}/R_c}\tag{2.23}$$

$$A_{\mu i}(x, y) = \sum_{\vec{n}} A_{\mu i}^{(\vec{n})}(x) e^{i\vec{n}\cdot\vec{\phi}/R_c}\tag{2.24}$$

$$\phi_{ij}(x, y) = \sum_{\vec{n}} \phi_{ij}^{(\vec{n})}(x) e^{i\vec{n}\cdot\vec{\phi}/R_c}\tag{2.25}$$

where  $h_{\mu\nu}^{(\vec{n})}$ ,  $A_{\mu i}^{(\vec{n})}$ , and  $\phi_{ij}^{(\vec{n})}$  are called KK modes on the 4D brane. These KK modes satisfy

$$\begin{aligned}(\square + M_{\vec{n}}^2) \left( h_{\mu\nu}^{(\vec{n})} - \frac{1}{2} h^{(\vec{n})} \eta_{\mu\nu} \right) &= 0 \\ (\square + M_{\vec{n}}^2) A_{\mu i}^{(\vec{n})} &= 0 \\ (\square + M_{\vec{n}}^2) \phi_{ij}^{(\vec{n})} &= 0\end{aligned}\tag{2.26}$$

with the common mass of these KK states  $h_{\mu\nu}^{(\vec{n})}$ ,  $A_{\mu i}^{(\vec{n})}$ ,  $\phi_{ij}^{(\vec{n})}$  being

$$M_{\vec{n}}^2 = \frac{\vec{n}^2}{R_c^2}\tag{2.27}$$

After KK decomposition, the bulk de Donder gauge condition

$$\hat{\partial}^M \left( \hat{h}_{MN} - \frac{1}{2} \hat{h} \hat{\eta}_{MN} \right) = 0\tag{2.28}$$

will now reduce to

$$\partial^\mu h_{\mu\nu}^{(\vec{n})} - \frac{1}{2} \partial^\mu h^{(\vec{n})} \eta_{\mu\nu} + \frac{i}{R_c} n_i A_{\nu i}^{(\vec{n})} = 0\tag{2.29}$$

$$\partial^\mu A_{\mu i} + \frac{i}{R_c} n_j \phi_{ij}^{(\vec{n})} + \frac{i}{2R_c} n_i h^{(\vec{n})} + \frac{i}{R_c} n_i \phi^{(\vec{n})} = 0\tag{2.30}$$

If we take a bulk gauge transformation

$$\hat{\xi}_M(x, y) = \sum_{\{\vec{n}\}} \xi_M^{(\vec{n})}(x) e^{i\vec{n}\cdot\vec{\phi}/R_c}\tag{2.31}$$

then the fields transforms according to Eq. (2.11) as

$$\hat{h}_{MN}(x, y) \rightarrow \hat{h}_{MN}(x, y) - \partial_M \hat{\xi}_N - \partial_N \hat{\xi}_M\tag{2.32}$$

which will give

$$h_{\mu\nu} \rightarrow h_{\mu\nu} - \partial_\mu \hat{\xi}_\nu - \partial_\nu \hat{\xi}_\mu + \partial_i \hat{\xi}_i \eta_{\mu\nu}\tag{2.33}$$

$$A_{\mu i} \rightarrow A_{\mu i} - \partial_\mu \hat{\xi}_i - \partial_i \hat{\xi}_\mu\tag{2.34}$$

$$\phi_{ij} \rightarrow \phi_{ij} - \frac{1}{2} \left( \partial_i \hat{\xi}_j + \partial_j \hat{\xi}_i \right)\tag{2.35}$$

In the Fourier modes the relation will become

$$h_{\mu\nu}^{(\vec{n})} \rightarrow h_{\mu\nu}^{(\vec{n})} - \partial_\mu \xi_\nu^{(\vec{n})} - \partial_\nu \xi_\mu^{(\vec{n})} + \frac{i}{R_c} n_i \xi_i^{(\vec{n})} \eta_{\mu\nu} \quad (2.36)$$

$$A_{\mu i}^{(\vec{n})} \rightarrow A_{\mu i}^{(\vec{n})} - \partial_\mu \xi_i^{(\vec{n})} - \frac{i}{R_c} n_i \xi_\mu^{(\vec{n})} \quad (2.37)$$

$$\phi_{ij}^{(\vec{n})} \rightarrow \phi_{ij}^{(\vec{n})} - \frac{i}{2R_c} n_i \xi_j^{(\vec{n})} - \frac{i}{2R_c} n_j \xi_i^{(\vec{n})} \quad (2.38)$$

This clearly shows that these fields do not remain invariant under bulk gauge transformations. Han, Lykken and Zhang showed that it is possible to get bulk gauge invariant fields [11]. For that, two projection operators are defined, viz.,

$$P_{ij}^{(\vec{n})} = \delta_{ij} - \frac{n_i n_j}{\vec{n}^2}, \quad \text{and} \quad \tilde{P}_{ij}^{(\vec{n})} = \frac{n_i n_j}{\vec{n}^2} \quad (2.39)$$

and they satisfy

$$P_{ij}^{(\vec{n})} P_{jk}^{(\vec{n})} = P_{ik}^{(\vec{n})}, \quad P_{ij}^{(\vec{n})} \tilde{P}_{jk}^{(\vec{n})} = 0, \quad \tilde{P}_{ij}^{(\vec{n})} \tilde{P}_{jk}^{(\vec{n})} = \tilde{P}_{ik}^{(\vec{n})} \quad (2.40)$$

$$P_{ii}^{(\vec{n})} = n - 1, \quad \tilde{P}_{ii}^{(\vec{n})} = 1, \quad n_i P_{ij}^{(\vec{n})} = 0, \quad n_i \tilde{P}_{ij}^{(\vec{n})} = n_j \quad (2.41)$$

Then, the fields are redefined as

$$\begin{aligned} \tilde{h}_{\mu\nu}^{(\vec{n})} &= h_{\mu\nu}^{(\vec{n})} - iR_c \frac{n_i}{\vec{n}^2} \left( \partial_\mu A_{\nu i}^{(\vec{n})} + \partial_\nu A_{\mu i}^{(\vec{n})} \right) \\ &\quad - \frac{1}{3} \left( P_{ij}^{(\vec{n})} + 3\tilde{P}_{ij}^{(\vec{n})} \right) \left( \frac{2}{M_{\vec{n}}} \partial_\mu \partial_\nu - \eta_{\mu\nu} \right) \phi_{ij}^{(\vec{n})} \end{aligned} \quad (2.42)$$

$$\tilde{A}_{\mu i}^{(\vec{n})} = P_{ij}^{(\vec{n})} \left( A_{\mu j}^{(\vec{n})} - 2i \frac{n_j}{\vec{n}^2} \partial_\mu \phi_{ij}^{(\vec{n})} \right) \quad (2.43)$$

$$\tilde{\phi}_{ij}^{(\vec{n})} = \sqrt{2} \left( P_{ik}^{(\vec{n})} P_{jl}^{(\vec{n})} + a P_{ij}^{(\vec{n})} P_{kl}^{(\vec{n})} \right) \phi_{kl}^{(\vec{n})} \quad (2.44)$$

with  $a$  satisfying  $3(n-1)a^2 + 6a - 1 = 0$ . It can be shown that these redefined physical fields are bulk gauge-invariant. The masses of these physical KK states  $\tilde{h}_{\mu\nu}^{(\vec{n})}, \tilde{A}_{\mu i}^{(\vec{n})}, \tilde{\phi}_{ij}^{(\vec{n})}$  are also the same as those of the original fields. Furthermore, the new fields also satisfy

$$\begin{aligned} \partial^\mu \tilde{h}_{\mu\nu}^{(\vec{n})} &= 0, & \tilde{h}^{(\vec{n})} &= 0, \\ \partial^\mu \tilde{A}_{\mu i}^{(\vec{n})} &= 0, & n_i \tilde{A}_{\mu i}^{(\vec{n})} &= 0, \\ n_i \tilde{\phi}_{ij}^{(\vec{n})} &= 0 \end{aligned} \quad (2.45)$$

The physical states can be identified as

- $\tilde{h}_{\mu\nu}^{(\vec{n})}$  : massive spin-2 states including  $\vec{n} = \vec{0}$ , which is massless
- $\tilde{A}_{\mu i}^{(\vec{n})}$  :  $n - 1$  massive spin-1 states; no zero mode
- $\tilde{\phi}_{ij}^{(\vec{n})}$  :  $n(n-1)/2$  massive spin-0 states; no zero mode

$\tilde{\phi}^{(\vec{n})} = \tilde{\phi}_{ii}^{(\vec{n})}$ , known as graviscalar, is the physical dilaton mode. In terms of these physical fields we can now write the Fierz-Pauli Lagrangian given in Eq. (2.20) as

$$\begin{aligned} \mathcal{L} = & \sum_{\{\vec{n}\}} \frac{1}{2} \left[ \partial^\mu \tilde{h}^{(\vec{n})\alpha\beta} \partial_\mu \tilde{h}_{\alpha\beta}^{(-\vec{n})} - \partial^\mu \tilde{h}^{(\vec{n})} \partial_\mu \tilde{h}^{(-\vec{n})} - 2 \partial_\mu \tilde{h}^{(\vec{n})\mu\alpha} \partial_\nu \tilde{h}_{\nu\alpha}^{(-\vec{n})} \right. \\ & \left. + \partial^\mu \tilde{h}_{\mu\alpha}^{(\vec{n})} \partial^\alpha \tilde{h}^{(-\vec{n})} + \partial^\mu \tilde{h}_{\mu\alpha}^{(-\vec{n})} \partial^\alpha \tilde{h}^{(\vec{n})} - M_{\vec{n}}^2 \left( \tilde{h}^{(\vec{n})\alpha\beta} \tilde{h}_{\alpha\beta}^{(-\vec{n})} - \tilde{h}^{(\vec{n})} \tilde{h}^{(-\vec{n})} \right) \right] \\ & + \sum_{\{\vec{n}\}} \sum_{i=1}^n \left[ -\frac{1}{2} \tilde{F}_i^{(\vec{n})\mu\nu} \tilde{F}_{i\mu\nu}^{(-\vec{n})} + M_{\vec{n}}^2 \tilde{A}_i^{(\vec{n})\mu} \tilde{A}_{i\mu}^{(-\vec{n})} \right] \\ & + \sum_{\{\vec{n}\}} \sum_{i,j=1}^n \left[ \frac{1}{2} \partial^\mu \tilde{\phi}_{ij}^{(\vec{n})} \partial_\mu \tilde{\phi}_{ij}^{(-\vec{n})} - \frac{1}{2} M_{\vec{n}}^2 \tilde{\phi}_{ij}^{(\vec{n})} \tilde{\phi}_{ij}^{(-\vec{n})} \right] \end{aligned} \quad (2.46)$$

with  $\tilde{F}_{i\mu\nu}^{(\vec{n})} = \partial_\mu \tilde{A}_{\nu i}^{(\vec{n})} - \partial_\nu \tilde{A}_{\mu i}^{(\vec{n})}$ . We can now find the free field equation for  $\tilde{h}_{\mu\nu}^{(\vec{n})}$ ,  $\tilde{A}_{\mu i}^{(\vec{n})}$ , and  $\tilde{\phi}_{ij}^{(\vec{n})}$  fields as

$$\begin{aligned} \square \left( \tilde{h}_{\mu\nu}^{(\vec{n})} - \frac{1}{2} \tilde{h}^{(\vec{n})} \eta_{\mu\nu} \right) - \partial_\mu \partial^\rho \left( \tilde{h}_{\rho\nu}^{(\vec{n})} - \frac{1}{2} \tilde{h}^{(\vec{n})} \eta_{\rho\nu} \right) - \partial_\nu \partial^\rho \left( \tilde{h}_{\mu\rho}^{(\vec{n})} - \frac{1}{2} \tilde{h}^{(\vec{n})} \eta_{\mu\rho} \right) \\ - \partial^\lambda \partial^\rho \left( \tilde{h}_{\lambda\rho}^{(\vec{n})} - \frac{1}{2} \tilde{h}^{(\vec{n})} \eta_{\lambda\rho} \right) \eta_{\mu\nu} + M_{\vec{n}}^2 \left( \tilde{h}_{\mu\nu}^{(\vec{n})} - \tilde{h}^{(\vec{n})} \eta_{\mu\nu} \right) = 0 \end{aligned} \quad (2.47)$$

$$\partial^\mu \tilde{F}_{i\mu\nu}^{(\vec{n})} + M_{\vec{n}}^2 \tilde{A}_{\nu i}^{(\vec{n})} = 0 \quad (2.48)$$

$$\left( \square + M_{\vec{n}}^2 \right) \tilde{\phi}_{ij}^{(\vec{n})} = 0 \quad (2.49)$$

and the propagators for these fields are given by

$$i\Delta_{\{\alpha\beta, \vec{n}\}, \{\mu\nu, \vec{m}\}}^{\tilde{h}}(k) = \frac{i\delta_{\vec{n}, -\vec{m}} P_{\alpha\beta, \mu\nu}}{k^2 - M_{\vec{n}}^2 + i\varepsilon} \quad (2.50)$$

$$i\Delta_{\{i\mu, \vec{n}\}, \{j\nu, \vec{m}\}}^{\tilde{A}}(k) = -\frac{i\delta_{\vec{n}, -\vec{m}} P_{ij}^{(\vec{n})} \left( \eta_{\mu\nu} - \frac{k_\mu k_\nu}{M_{\vec{n}}^2} \right)}{k^2 - M_{\vec{n}}^2 + i\varepsilon} \quad (2.51)$$

$$i\Delta_{\{ij, \vec{n}\}, \{kl, \vec{m}\}}^{\tilde{\phi}}(k) = \frac{i\delta_{\vec{n}, -\vec{m}} \left( P_{ik}^{(\vec{n})} P_{jl}^{(\vec{n})} + P_{il}^{(\vec{n})} P_{jk}^{(\vec{n})} \right)}{2(k^2 - M_{\vec{n}}^2 + i\varepsilon)} \quad (2.52)$$

where

$$\begin{aligned} P_{\alpha\beta, \mu\nu}(k) = & \left( \eta_{\alpha\mu} - \frac{k_\alpha k_\mu}{M_{\vec{n}}^2} \right) \left( \eta_{\beta\nu} - \frac{k_\beta k_\nu}{M_{\vec{n}}^2} \right) + \left( \eta_{\alpha\nu} - \frac{k_\alpha k_\nu}{M_{\vec{n}}^2} \right) \left( \eta_{\beta\mu} - \frac{k_\beta k_\mu}{M_{\vec{n}}^2} \right) \\ & - \frac{2}{3} \left( \eta_{\alpha\beta} - \frac{k_\alpha k_\beta}{M_{\vec{n}}^2} \right) \left( \eta_{\mu\nu} - \frac{k_\mu k_\nu}{M_{\vec{n}}^2} \right) \end{aligned} \quad (2.53)$$

In the ADD model, SM fields are confined to the brane situated at  $\vec{y} = \vec{0}$ . The action for minimal interactions of SM fields with gravity would be

$$S = \int d^{4+n}x \sqrt{|\hat{g}_{\text{ind}}|} \mathcal{L}_m(\Phi, V_\mu, \Psi) \quad (2.54)$$

where  $\hat{g}_{\text{ind}}$  is the induced metric on the 4D brane and  $\mathcal{L}_m$  represents matter Lagrangian containing scalar, vector, or fermionic fields which are represented by  $\Phi$ ,  $V_\mu$ , and  $\Psi$  respectively. The fluctuation of metric field, graviton, interacts with matter fields via the following action

$$S = \int d^{4+n}x \frac{\delta \left( \sqrt{|\hat{g}_{\text{ind}}|} \mathcal{L}_m \right)}{\delta \hat{g}_{MN}} \Big|_{\hat{\eta}_{MN}} \delta \hat{g}_{MN} \quad (2.55)$$

Now, recalling that  $\delta\hat{g}_{MN} = \hat{\kappa}\hat{h}_{MN}$  and SM fields are confined to 4D brane, we can write the above equation as

$$S = \frac{\hat{\kappa}}{\sqrt{V_n}} \int d^4x \left. \frac{\delta(\sqrt{-g}\mathcal{L}_m)}{\delta g_{\mu\nu}} \right|_{\eta_{\mu\nu}} (h_{\mu\nu} + \phi\eta_{\mu\nu}) \quad (2.56)$$

$$= -\frac{\kappa}{2} \int d^4x T^{\mu\nu} (h_{\mu\nu} + \phi\eta_{\mu\nu}) \quad (2.57)$$

where  $\kappa \equiv \frac{\hat{\kappa}}{\sqrt{V_n}} = 16\pi G_N$  and  $T^{\mu\nu}$  is the energy-momentum tensor defined in Eq. (1.63). We have used the approximation  $g = 1 + \mathcal{O}(\kappa)$  in the expression of the energy-momentum tensor,  $T^{\mu\nu}$ , in the Eq. (2.57). In terms of physical KK modes, the interaction Lagrangian becomes

$$\mathcal{L}_{\text{int}} = -\frac{\kappa}{2} \sum_{\{\vec{n}\}} \left( T^{\mu\nu} \tilde{h}_{\mu\nu}^{(\vec{n})} + \omega \tilde{\phi}^{(\vec{n})} T^\mu{}_\mu \right) \quad (2.58)$$

with  $\omega = \sqrt{\frac{2}{3(n+2)}}$ . We can now substitute the energy-momentum tensor for SM matter fields as given in Eq. (1.64) to get interaction terms for gravity-matter interaction. The Lagrangian for gravity-matter interaction becomes

- for a scalar field  $\Phi$ ,

$$\begin{aligned} \mathcal{L}_\Phi^{(\vec{n})} = & -\kappa \left[ \left( \tilde{h}_{\mu\nu}^{(\vec{n})} - \frac{1}{2}\eta_{\mu\nu}\tilde{h}^{(\vec{n})} \right) D^\mu\Phi^\dagger D^\nu\Phi + \frac{1}{2}\tilde{h}^{(\vec{n})}m_\Phi^2\Phi^\dagger\Phi \right. \\ & \left. - \omega\tilde{\phi}^{(\vec{n})} \left( D^\mu\Phi^\dagger D_\mu\Phi - 2m_\Phi^2\Phi^\dagger\Phi \right) \right] \end{aligned} \quad (2.59)$$

- for gauge bosons  $V_\mu$ ,

$$\begin{aligned} \mathcal{L}_V^{(\vec{n})} = & -\kappa \left[ \frac{1}{8} \left( \tilde{h}^{(\vec{n})}\eta_{\mu\nu} - 4\tilde{h}_{\mu\nu}^{(\vec{n})} \right) F^\mu{}_\beta F^{\nu\beta} - \frac{1}{4} \left( \tilde{h}^{(\vec{n})}\eta_{\mu\nu} - 2\tilde{h}_{\mu\nu}^{(\vec{n})} \right) m_V^2 V^\mu V^\nu \right. \\ & - \frac{\tilde{h}^{(\vec{n})}}{2\xi} \left( \partial_\mu\partial_\nu V^\mu V^\nu + \frac{1}{2}\partial_\mu V^\mu\partial_\nu V^\nu \right) + \frac{\tilde{h}_{\mu\nu}^{(\vec{n})}}{\xi} \partial^\mu\partial_\beta V^\beta V^\nu \\ & \left. - \frac{\omega}{2}m_V^2\tilde{\phi}^{(\vec{n})}V^\mu V_\mu + \frac{\omega}{\xi}\partial_\mu\tilde{\phi}^{(\vec{n})}\partial_\nu V^\nu V^\mu \right] \end{aligned} \quad (2.60)$$

- for fermion fields  $\Psi$

$$\begin{aligned} \mathcal{L}_\Psi^{(\vec{n})} = & -\frac{\kappa}{2} \left[ \left( \tilde{h}_{\mu\nu}^{(\vec{n})} - \eta_{\mu\nu}\tilde{h}^{(\vec{n})} \right) \bar{\Psi}i\gamma^\mu D^\nu\Psi + m_\Psi\tilde{h}^{(\vec{n})}\bar{\Psi}\Psi + \frac{1}{2}\bar{\Psi}i\gamma^\mu \left( \partial^\nu\tilde{h}_{\mu\nu}^{(\vec{n})} - \partial_\mu\tilde{h}^{(\vec{n})} \right) \Psi \right. \\ & \left. - 3\omega\tilde{\phi}^{(\vec{n})}\bar{\Psi}i\not{D}\Psi + 4\omega m_\Psi\tilde{\phi}^{(\vec{n})}\bar{\Psi}\Psi - \frac{3\omega}{2}\partial_\mu\tilde{\phi}^{(\vec{n})}\bar{\Psi}i\gamma^\mu\Psi \right] \end{aligned} \quad (2.61)$$

One can now get the Feynman rules at tree-level for the gravity-matter interaction and study phenomenology of the model. However, we need to be cautious about studying higher order correction in the loop level since quantum theory of gravity is nonrenormalizable.

From the above we can deduce some important features of ADD phenomenology.

- There is one 4D spin-2 state  $\tilde{h}_{\mu\nu}^{(\vec{n})}$  and one scalar state  $\tilde{\phi}^{(\vec{n})} = \tilde{\phi}_{ii}^{(\vec{n})}$  for each KK mode which will interact with SM fields, which are confined to the brane. The graviton couples to the SM particles via energy-momentum tensor while the graviscalar interacts via the trace of energy-momentum tensor. Since the graviscalar couples to the trace of the energy-momentum tensor, it does not couple to the massless gauge bosons and fermions.
- The other states,  $\tilde{A}_{\mu i}^{(\vec{n})}$  and  $\tilde{\phi}_{ij}^{(\vec{n})}$ , though they are there in bulk, do not interact with the SM fields on the brane at the tree-level.
- The coupling of  $\tilde{h}_{\mu\nu}^{(\vec{n})}$  and  $\tilde{\phi}^{(\vec{n})}$  to the SM particles are independent of flavour and colour, but depends on the spin of the particles.
- The coupling does not depend on the KK mode of the KK graviton or KK graviscalar. Hence, in a process, all the KK modes contribute with equal strength as long as their masses are below the cutoff relevant to the process.
- The coupling of each KK graviton and KK graviscalar to matter particles, which goes as  $\kappa$ , is so feeble that there is almost no possibility of detecting them in an experimental detector and hence it will be missing in the detector. Like supersymmetric particles, they will give signatures of missing energy at collider experiments.

### 2.2.2 ADD Mass Spectra of KK Modes

As we have seen in the previous subsection, the masses of  $\vec{n}^{\text{th}}$  KK state goes as

$$M_{\vec{n}}^2 = \frac{\vec{n}^2}{R_c^2} \quad (2.62)$$

and hence the mass difference between nearest KK states is

$$\Delta M_{\vec{n}} = \frac{1}{R_c} \quad (2.63)$$

If we take large extra dimensions — e.g.  $R_c \sim 10^{-10}$  m, which is many orders larger than the Planck length  $10^{-35}$  m — then

$$\Delta M_{\vec{n}} = \frac{1}{R_c} \sim 2 \text{ keV} \quad (2.64)$$

If the typical energy of collider experiment is  $\sim \text{TeV}$ , there would be  $10^9$  states of KK gravitons accessible in a typical scattering process. Hence, this mass spectrum, as far as today's collider experiments are concerned may be considered to form a quasi-continuum. On this nearly continuum mass spectrum sum on the modes can be replaced by an integral with density-of-states of KK gravitons

$$\sum_{\{\vec{n}\}} \longrightarrow \int dM \rho(M) \quad (2.65)$$

where  $\rho(M)$  is the number density of KK graviton having mass between  $M$  and  $M + dM$ . As the KK gravitons satisfy a mass relation

$$\frac{n_1^2}{R_c^2} + \frac{n_2^2}{R_c^2} + \dots + \frac{n_n^2}{R_c^2} = M_{\vec{n}}^2 \quad (2.66)$$

the density-of-state function will be

$$\rho(M) dM = \frac{2\pi^{\frac{n}{2}} R_c^n}{\Gamma\left(\frac{n}{2}\right)} M^{n-1} dM \quad (2.67)$$

Since  $M_D$  is a more convenient parameter to work with, we replace  $R_c$  using Eq. (1.85) to get

$$\rho(M) dM = \frac{1}{\kappa^2} \frac{4\pi^{\frac{n}{2}}}{\Gamma\left(\frac{n}{2}\right)} \frac{M^{n-1}}{M_D^{n+2}} dM \quad (2.68)$$

where  $\kappa = \frac{M_P}{\sqrt{16\pi}}$ . This  $\kappa^{-2}$  factor in front of the density-of-state expression will be cancelled by the coupling  $\kappa^2$  of the graviton in the squared amplitude. Thus, in a process where a real graviton is emitted, if the centre-of-momentum energy of the experiment is  $E$ , the number of KK modes, collectively, gives a contribution

$$\sim \left(\frac{E}{M_D}\right)^{n+2} \quad (2.69)$$

This is suppressed by the bulk Planck scale,  $M_D$ , rather than the 4D Planck scale,  $M_P$ , and makes the effective interaction of electroweak strength rather than the much weaker gravitational strength.

### 2.2.3 Graviton Processes

At the tree-level, there are two types of processes where ADD graviton KK modes can contribute [5, 11]. We discuss these separately in the following.

#### Emission of Real KK States

Like other particles in the Standard Model, KK states – both graviton and graviscalar – can be produced in scattering processes. An example of such a process is

$$A + B \longrightarrow X + \tilde{h}_{\mu\nu}^{(\vec{n})} \quad (2.70)$$

This type of process will be relevant in different types of experiments as well as in astrophysical considerations.

In astrophysical processes, emission of KK gravitons will accelerate cooling of supernova by carrying away a substantial part of the energy. As explained in the previous subsection, there will be a huge number of KK modes contributing to the cooling dynamics of astrophysical bodies. These types of processes in the ADD model has been studied in the literature in the context of neutron stars [12] and supernovae [13] cooling. These give lower bounds on  $M_D$  at  $\sim 10$  TeV for  $n = 3$ ; the bound is less for higher numbers of extra dimensions.

At a collider, as mentioned earlier, KK gravitons cannot be detected in a detector and will give rise to missing energy signals. All the KK modes with masses upto the kinematical limit, which is close to the machine energy in most of the processes, will contribute to the same signal. The processes with each KK mode labelled by  $\vec{n}$  correspond to different processes and will be added incoherently. If the centre-of-mass energy of a collider is  $E_{cm}$ , the total cross-section will go as

$$\sigma = \sum_{\{\vec{n}\}} \sigma_{\vec{n}} \sim \frac{1}{E_{cm}^2} \left(\frac{E_{cm}}{M_D}\right)^{n+2} \quad (2.71)$$

This, again, is suppressed only by powers of the bulk Planck scale and may be observable. This will be discussed more elaborately in Chapters 5 and 6.

### Exchange of Virtual KK States

KK gravitons and graviscalars can also appear as virtual states in a scattering process. Since KK modes couple to SM particles irrespective of their flavour or colour, every neutral current interaction, mediated by photon,  $Z$  boson or Higgs boson, will also have a graviton/graviscalar-mediated counterpart. One such example is shown in Figure 2.1 where a KK graviton and a

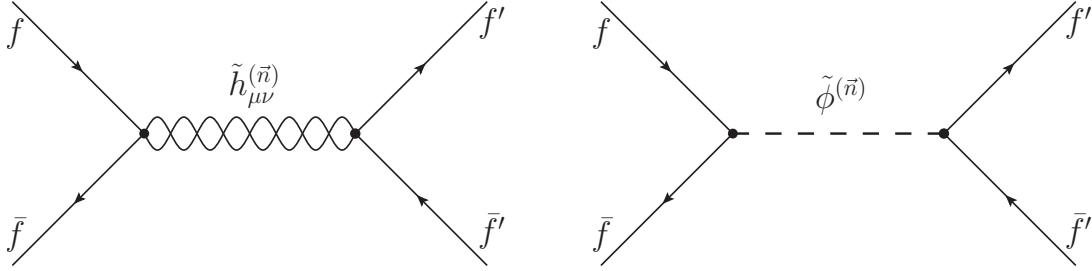


Figure 2.1: Feynman diagram of a process involving exchange of virtual KK states.

graviscalar is getting exchanged in the process  $f\bar{f} \rightarrow f'\bar{f}'$ , and there are, of course, SM diagrams in addition to the diagrams shown in Figure 2.1. The amplitude for the process can be written as

$$i\mathcal{M} = i\mathcal{M}_{\text{SM}} + \sum_{\{\vec{n}\}} i\mathcal{M}_{(\vec{n})} \quad (2.72)$$

where the subscript ‘SM’ stands for the Standard Model contribution and the sum is over KK modes. Here, unlike the real graviton emission process, the final states are the same for all values of  $\vec{n}$  and hence the summation over KK modes are done in a coherent fashion, i.e. at the amplitude level. The summation can then be approximated as an integration with the appropriate density-of-states function described in the previous subsection. Since the mass of the KK mode appears only in the propagators, we can factor out the summation part and the part which is not dependent on the KK mode [5]

$$\sum_{\{\vec{n}\}} \mathcal{M}_{\vec{n}} = \left( \sum_{\{\vec{n}\}} \frac{\kappa^2}{q^2 - M_{\vec{n}}^2 + i\epsilon} \right) \overline{\mathcal{M}} \rightarrow \left( \int dM \frac{\kappa^2 \rho(M)}{q^2 - M^2 + i\epsilon} \right) \overline{\mathcal{M}} \quad (2.73)$$

where  $\overline{\mathcal{M}}$  is the part independent on KK mode numbers and is like a contact interaction.

The upper limit for the integration in Eq. (2.73) is not pre-defined. A natural choice is the bulk Planck scale,  $M_D$ , where the quantum effects for gravity becomes important and the decomposition into KK modes should break down. The term in parentheses in Eq. (2.73) can now be treated as an effective coupling for the contact interaction [5]

$$G_{\text{eff}} \simeq \frac{\lambda_n}{M_D^4} \quad (2.74)$$

where  $\lambda_n$  is a constant dependent on the number  $n$  of extra dimensions. Thus, we get an effective contact interaction, with the scale being the bulk Planck mass. The dependence on the exact

choice of the cut off for the mass of accessible KK mode is very small, but the dependence is slightly more sensitive to the number of extra dimensions [5].

## 2.3 RS Model and Phenomenology

When we consider the RS model with a warped extra dimension, we again have a spacelike extra dimension of length very close to the Planck length. The Standard Model fields are confined to the IR brane and hence, we need to develop Feynman rules on the IR brane, in a manner similar to that done for the ADD model. However, in this case, the geometry is not flat, as it was in the ADD model, and hence we must take into account the metric

$$d\hat{s}^2 = e^{-2\mathcal{K}R_c\phi} \eta_{\mu\nu} dx^\mu dx^\nu - R_c^2 d\phi^2 \equiv \hat{g}_{MN} dx^M dx^N \quad (2.75)$$

with

$$\phi \rightarrow \phi + 2\pi, \quad \phi \rightarrow -\phi \quad (2.76)$$

We require to find the KK modes of the graviton in this geometry and then determine their interactions with the fields confined to the IR brane.

### 2.3.1 RS Graviton

If we start from the general coordinate invariant Lagrangian in RS model given in Eq. (1.93), we can get 4D effective action after integrating over the extra dimension

$$S_{\text{eff}} = 2\hat{M}^3 \int d^4x \int_{-\pi}^{\pi} d\phi R_c e^{-2\mathcal{K}R_c|\phi|} \sqrt{g} \mathcal{R} \quad (2.77)$$

where  $g$ , and  $\mathcal{R}$  are the determinant of the 4D metric and the 4D Ricci scalar respectively. On the IR brane, the action becomes

$$S_{\text{eff}}^{(\text{IR})} = \frac{2\hat{M}^3}{\mathcal{K}} [1 - e^{-2\pi\mathcal{K}R_c}] \int d^4x \sqrt{g} \mathcal{R} \quad (2.78)$$

This should correctly reproduce the 4D effective action given in Eq. (1.78) on IR brane since all the experimental results are consistent with the 4D universe. Hence, matching this with the 4D action gives a relation between the 4D Planck mass and the 5D Planck mass

$$M_P^2 = \frac{32\pi\hat{M}^3}{\mathcal{K}} [1 - e^{-2\pi\mathcal{K}R_c}] \quad (2.79)$$

This tells us that the Planck mass is not very sensitive to the radius of the extra dimension. However, as we noticed in Chapter 1, the stability of the size of the extra dimension plays an important role in warping down the mass scale at the TeV brane.

If we now consider the fluctuation of the 4D metric with respect to the background metric  $\eta_{\mu\nu}$ , just as we did in the previous section, the line element in the bulk with the fluctuation is given by

$$d\hat{s}^2 = e^{-2\mathcal{K}R_c|\phi|} (\eta_{\mu\nu} + h_{\mu\nu}) dx^\mu dx^\nu - R_c^2 d\phi^2 \quad (2.80)$$

The equation of motion of the graviton,  $h_{\mu\nu}$ , can be obtained by varying the action. In the warped geometry, the harmonics are Bessel functions of order unity and it is in terms of these

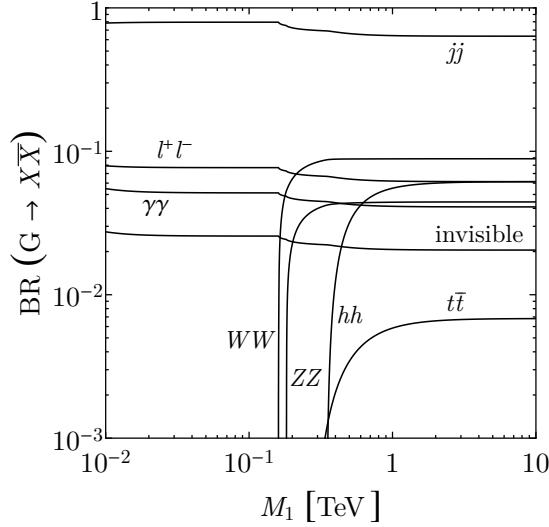


Figure 2.2: Branching fraction of lightest RS graviton in different decay channels.

that the Fourier expansion should be made. The Fourier coefficients, as in the ADD case, will be the KK modes of the 5D graviton on the 4D IR brane. The mass spectrum of the KK graviton is given by [14, 15]

$$M_n = \pi j_n \mathcal{K} e^{-\pi \mathcal{K} R_c} \quad (2.81)$$

where  $j_n$  are the zeros of Bessel function i.e.  $J_1(j_n) = 0$ . The values of  $j_n$  roughly go as  $(n + 0.25)$ , which means that the masses of KK gravitons are well separated and separation is around the scale of a TeV. This is quite different from the gravitons in the ADD model where the KK modes form a quasi-continuum of masses. In the RS model, the graviton KK modes, having masses  $\sim$ TeV, can be observed as resonances at a TeV collider such as the LHC. As we can see from Figure 2.2 the dominant decay mode for such a graviton is into dijets. However, the cleanest channels in a hadron collider are diphoton and dilepton, hence, even if the corresponding branching ratios are small, they give stronger bounds on the graviton masses. At the 13 TeV LHC, these have been studied by ATLAS (CMS) in diphoton (dilepton) channel with 36.7 (2.7)  $\text{fb}^{-1}$  of data yielding a bound of 4.1 (3.1) TeV bound on the mass of lightest KK graviton.

### 2.3.2 Goldberger-Wise Stabilisation and the Radion

In the RS model, there is a single graviscalar, but its phenomenology is somewhat different from the ADD case. We have already mentioned that in the case of a warped extra dimension the solution to the hierarchy problem relies on bringing down the mass scale at TeV brane by a factor of  $e^{-\pi \mathcal{K} R_c}$  with respect to the mass scale at the UV brane i.e.  $M_{\text{Pl}} \sim 10^{19}$  GeV to a TeV, for which we need  $\mathcal{K} R_c \simeq 11.6$ . Since the factor is in the exponent, a small fluctuation in the radius of the extra dimension, which may be generated from the fluctuation of the background geometry, leads to large fluctuations in the mass scale at the TeV brane. Thus, a dynamical means of stabilisation requires to be added to the minimal RS model. To see this, with the

fluctuation the distance function can be written as

$$d\hat{s}^2 = e^{-2T(x)|\phi|} g_{\mu\nu}(x) dx^\mu dx^\nu - \left[ \frac{T(x)}{\mathcal{K}} \right]^2 d\phi^2 \quad (2.82)$$

where  $g_{\mu\nu}$  is the 4D metric and  $T(x)$  is called the *modulus field*. With this geometry, the Einstein-Hilbert action in 5D

$$\hat{S} = 2\hat{M}^3 \int d^4x d\phi \sqrt{\hat{g}} \hat{\mathcal{R}} \quad (2.83)$$

can be reduced to an effective action in terms of 4D massless modes  $T(x)$  and  $g_{\mu\nu}(x)$  as

$$\hat{S} = \frac{2\hat{M}^3}{\mathcal{K}} \int d^4x d\phi \sqrt{-g} e^{-2|\phi|T} \left[ 6|\phi| \partial_\mu T \partial^\mu T - 6\phi^2 T \partial_\mu T \partial^\mu T + T \mathcal{R} \right] \quad (2.84)$$

where  $g$ , and  $\mathcal{R}$  are the determinant of the metric and the Ricci scalar in 4D respectively. After integrating over  $\phi$  we get

$$\hat{S} = \frac{2\hat{M}^3}{\mathcal{K}} \int d^4x \sqrt{-g} (1 - e^{-2\pi T}) \mathcal{R} + \frac{12M^3}{\mathcal{K}} \int d^4x \sqrt{-g} \partial_\mu (e^{-2T}) \partial^\mu (e^{-2T}). \quad (2.85)$$

If we reparametrise the modulus field  $T(x)$  as a graviscalar

$$\chi(x) = f e^{-\pi T(x)} \quad (2.86)$$

with  $f = \sqrt{\frac{24\hat{M}^3}{\mathcal{K}}}$  then the action becomes

$$\hat{S} = \frac{2\hat{M}^3}{\mathcal{K}} \int d^4x \sqrt{-g} \left[ 1 - \left( \frac{\chi(x)}{f} \right)^2 \right] \mathcal{R} + \frac{1}{2} \int d^4x \sqrt{-g} \partial_\mu \chi(x) \partial^\mu \chi(x). \quad (2.87)$$

The last term in the action is, clearly, the kinetic term of the graviscalar  $\chi(x)$ . We observe that this is a massless free field and it can have any vacuum expectation value  $\langle \chi(x) \rangle$  whatsoever. Since  $R_c = \langle T(x) \rangle = -\frac{1}{\pi} \ln \left( \frac{1}{f} \langle \chi(x) \rangle \right)$  it follows that  $R_c$  can be completely arbitrary.

A mechanism for stabilization of  $R_c$  was proposed by Goldberger and Wise [16]. For this, a real scalar bulk field  $\hat{B}(\hat{x})$  is added with potential terms on the Planck (UV) and TeV (IR) brane at  $\phi = 0$  and  $\phi = \pi$  respectively. The action is, then, given by

$$S = S_{\text{bulk}} + S_{UV} + S_{IR} \quad (2.88)$$

where  $S_{\text{bulk}}$ ,  $S_{UV}$  and  $S_{IR}$  are the action in the bulk, the UV brane and the IR brane respectively. They are given by

$$S_{\text{bulk}} = \int d^4x d\phi \sqrt{\hat{g}} \left( \frac{1}{2} \partial_A \hat{B} \partial^A \hat{B} - \frac{1}{2} M_B^2 \hat{B}^2 \right), \quad (2.89)$$

$$S_{UV} = - \int d^4x d\phi \sqrt{-\hat{g}_0} \lambda_h \left( \hat{B}^2 - V_0^2 \right)^2 \delta(\phi), \quad (2.90)$$

$$S_{IR} = - \int d^4x d\phi \sqrt{-\hat{g}_\pi} \lambda_h \left( \hat{B}^2 - V_\pi^2 \right)^2 \delta(\phi - \pi) \quad (2.91)$$

where the subscripts 0 and  $\pi$  represent the labels for UV and IR branes respectively. Due to the presence of these brane potential terms,  $\hat{B}$  develops a  $\phi$ -dependent vev. The vev for  $\hat{B}$  can

be determined by solving the equations of motion. Then, inserting the solution into the bulk scalar action, and integrating over  $\phi$ , we get a potential term for the field  $\chi(x)$

$$V(\chi) = \frac{\mathcal{K}^3}{144\hat{M}^6} \chi^4 \left[ V_\pi - V_0 \left( \frac{\chi}{f} \right)^\alpha \right] \quad (2.92)$$

with  $\alpha = M_B^2/4\mathcal{K}^2 \ll 1$ . It is clear from Eq. (2.92) that the potential has a minimum at

$$\frac{\langle \chi \rangle}{f} = \left( \frac{V_\pi}{V_0} \right)^{1/\alpha} \quad (2.93)$$

or

$$\mathcal{K}R_c = \langle T(x) \rangle = \frac{4\mathcal{K}^2}{\pi M_B^2} \ln \frac{V_\pi}{V_0} \quad (2.94)$$

The value of  $\mathcal{K}R_c$  can be set to  $\simeq 11.6$  without any extreme fine tuning of the parameters of the theory. If, however, one calculates  $V''(\chi)$  at  $\chi = \langle \chi \rangle$ , we will get

$$V''(\langle \chi \rangle) \propto e^{2\pi\mathcal{K}R_c} \quad (2.95)$$

which is very large since  $e^{2\pi\mathcal{K}R_c} \sim 10^{32}$ . This shows that the minimum is a very sharp one and hence we get a good mechanism for stabilisation of the modulus field  $T(x)$ .

Now, if we expand the graviscalar field  $\chi$  around  $\langle \chi \rangle = \Lambda_\varphi$

$$\chi = \Lambda_\varphi + \varphi. \quad (2.96)$$

the value at the minimum of the potential gives the mass and coupling of the  $\varphi$  field to other fields. This  $\varphi$  field is usually called the *radion*. The mass of radion is obtained as

$$M_\varphi^2 = \left. \frac{\partial^2 V(\chi)}{\partial \chi^2} \right|_{\Lambda_\varphi} = \frac{a^2 V_{IR}^2 \mathcal{K}^3}{72M^6} \Lambda_\varphi^2 = \frac{V_{IR}^2 \mathcal{K}^2 a^2}{3M^3} e^{-2\pi\mathcal{K}R_c} \quad (2.97)$$

where we replace  $\Lambda_\varphi$  with  $f e^{-\pi\mathcal{K}R_c}$  which is the expectation value for the radius. Clearly, the mass is suppressed by the same exponential factor  $e^{-\pi\mathcal{K}R_c}$  as the KK gravitons and hence the mass of the radion also comes in the TeV range. In fact, it is suppressed by another factor of  $a$  and hence it is logical to think that the radion is lighter than the KK states of the bulk graviton. Hence, it might well be the first signal for RS model to be discovered at colliders.

In the minimal RS model, as mentioned previously, all the matter fields are confined to the IR brane situated at  $\phi = \pi$ . Hence, the interaction between SM fields and radion – a part of the 5D gravitational field – arises from 4D general coordinate invariant matter field action

$$S = \int d^4x d\phi \sqrt{|\hat{g}_\pi|} \hat{\mathcal{L}}_m(\hat{g}_\pi^{\mu\nu}) \delta(\phi - \pi) \quad (2.98)$$

where  $\hat{\mathcal{L}}_m$  is the Lagrangian containing matter fields and  $\hat{g}_{\pi,\mu\nu}$  is the induced metric on the 4D IR brane. For RS geometry with Goldberger-Wise stabilization mechanism, the latter is

$$\hat{g}_{\pi,\mu\nu} = e^{-2\pi T(x)} g_{\mu\nu} \quad (2.99)$$

where  $g_{\mu\nu}$  is the usual 4D metric. After integration over  $\phi$ , the 4D action will be

$$S = \int d^4x \sqrt{-g} e^{-4\pi T(x)} \hat{\mathcal{L}}_m(\hat{g}_\pi^{\mu\nu}) \quad (2.100)$$

If we expand the the matter Lagrangian as a series in the metric,

$$\hat{\mathcal{L}}_m = \hat{\mathcal{L}}_m^{(0)} + \hat{\mathcal{L}}_m^{(1)} + \hat{\mathcal{L}}_m^{(2)} + \dots \quad (2.101)$$

where  $\hat{\mathcal{L}}_m^{(n)}$  contains  $n$ th powers of  $\hat{g}_\pi^{\mu\nu}$ , then on the TeV brane the Lagrangian will be expanded as

$$\hat{\mathcal{L}}_m = \mathcal{L}_m^{(0)} + e^{2\pi T} \mathcal{L}_m^{(1)} + e^{4\pi T} \mathcal{L}_m^{(2)} + \dots \quad (2.102)$$

where the  $\mathcal{L}_m^{(n)}$  are terms containing  $n$ th powers of 4D  $g^{\mu\nu}$ . Eq. (2.100), then, can be written as

$$S = \int d^4x \sqrt{-g} \left[ e^{-4\pi T(x)} \mathcal{L}_m^{(0)} + e^{-2\pi T(x)} \mathcal{L}_m^{(1)} + \mathcal{L}_m^{(2)} + \dots \right] \quad (2.103)$$

$$= \int d^4x \sqrt{-g} \left[ \left( \frac{\chi(x)}{f} \right)^4 \mathcal{L}_m^{(0)} + \left( \frac{\chi(x)}{f} \right)^2 \mathcal{L}_m^{(1)} + \mathcal{L}_m^{(2)} + \dots \right] \quad (2.104)$$

$$= \int d^4x \sqrt{-g} \left[ \left( 1 + \frac{\varphi}{\Lambda_\varphi} \right)^4 e^{-4\pi \mathcal{K} R_c} \mathcal{L}_m^{(0)} \right. \\ \left. + \left( 1 + \frac{\varphi}{\Lambda_\varphi} \right)^2 e^{-2\pi \mathcal{K} R_c} \mathcal{L}_m^{(1)} + \mathcal{L}_m^{(2)} + \dots \right] \quad (2.105)$$

where we now write  $g$  for  $g_\pi$  in view of the fact that the IR brane is the observed Universe. After absorbing powers of  $e^{-\pi \mathcal{K} R_c}$  into the terms  $\mathcal{L}_m^{(n)}$  to redefine fields and mass parameters as was also done in Eqs. (1.89–1.91), we get the four dimensional Lagrangian. After the expansion, we get the action for radion field interacting with the matter field as

$$S = \int d^4x \sqrt{-g} \mathcal{L}_m + \int d^4x \sqrt{-g} \frac{\varphi}{\Lambda_\varphi} \left( 4\mathcal{L}_m^0 + 2\mathcal{L}_m^1 + \dots \right) \quad (2.106)$$

Clearly, the first integral is the general coordinate invariant Lagrangian on the IR brane and the second term represents the coupling of radion field with the matter fields. The terms with matter couplings with more than one radion which can be derived from Eq. (2.105) are not included in the Eq. (2.106). On the other hand,  $T_{\mu\nu}$  as defined in Eq. (1.63) with the Lagrangian given in Eq. (2.101), but in 4D, can be calculated as

$$T_{\mu\nu} = -2 \frac{\partial}{\partial g^{\mu\nu}} \left( \mathcal{L}_m^{(0)} + \mathcal{L}_m^{(1)} + \mathcal{L}_m^{(2)} + \dots \right) + g_{\mu\nu} \left( \mathcal{L}_m^{(0)} + \mathcal{L}_m^{(1)} + \mathcal{L}_m^{(2)} + \dots \right) \quad (2.107)$$

The trace of the energy-momentum tensor is given by

$$T^\mu{}_\mu = g^{\mu\nu} T_{\mu\nu} \quad (2.108)$$

$$= -2g^{\mu\nu} \frac{\partial}{\partial g^{\mu\nu}} \left( \mathcal{L}_m^{(0)} + \mathcal{L}_m^{(1)} + \mathcal{L}_m^{(2)} + \dots \right) \\ + g^{\mu\nu} g_{\mu\nu} \left( \mathcal{L}_m^{(0)} + \mathcal{L}_m^{(1)} + \mathcal{L}_m^{(2)} + \dots \right) \quad (2.109)$$

$$= -2 \left( 0 + \mathcal{L}_m^{(1)} + 2\mathcal{L}_m^{(2)} + \dots \right) + 4 \left( \mathcal{L}_m^{(0)} + \mathcal{L}_m^{(1)} + \mathcal{L}_m^{(2)} + \dots \right) \quad (2.110)$$

$$= 4 \mathcal{L}_m^{(0)} + 2 \mathcal{L}_m^{(1)} + \dots \quad (2.111)$$

where we use Euler's theorem for homogeneous function to get the result after summing over  $\mu$  and  $\nu$ . The term within parentheses in the last integral of Eq. (2.106) is the same as  $T^\mu{}_\mu$  as given in Eq. (2.111). We can therefore conclude that the radion couples to the trace of the

four-dimensional energy-momentum tensor. Hence, the coupling of  $\varphi$  to the matter field on 4D, is given by

$$\mathcal{L}_{\text{int}}(\varphi) = \frac{\varphi}{\Lambda_\varphi} T^\mu{}_\mu \quad (2.112)$$

The form of  $T^\mu{}_\mu$  for the SM Lagrangian as given in Eq. (1.68) suggests that the coupling of the radion field is very similar to that of the SM Higgs. However, The Eq. (1.68) is not complete since there is also a trace anomaly term. This makes the phenomenology of radion slightly different for the massless gauge bosons. So, the complete Lagrangian for radion coupling to SM fields is given by

$$\mathcal{L}_{\text{int}}(\varphi) = \frac{\varphi}{\Lambda_\varphi} (T^\mu{}_\mu + \mathcal{A}_T) \quad (2.113)$$

where, for SM Lagrangian,  $T^\mu{}_\mu$  and  $\mathcal{A}_T$  are given in Eq. (1.68) and Eq. (1.76) respectively. This will play an important role in Chapter 3 and especially Chapter 4.

## CHAPTER 3

---

# Mixed Higgs-Radion States at the LHC

---

### 3.1 Introduction

In the previous chapter, we have discussed the model of Goldberger and Wise (1999) [16] who rewrite the metric in Eq. (2.75) as

$$d\hat{s}^2 = e^{-2T(x)\phi} \eta_{\mu\nu} dx^\mu dx^\nu - \left[ \frac{T(x)}{\mathcal{K}} \right]^2 d\phi^2 \quad (3.1)$$

where the modulus field  $T(x)$  can be parametrised as a *radion*

$$\varphi(x) = \Lambda_\varphi \left( e^{-\pi\{T(x)-\mathcal{K}R_c\}} - 1 \right) \quad (3.2)$$

which has a vacuum expectation value

$$\Lambda_\varphi = \sqrt{\frac{24\hat{M}^3}{\mathcal{K}}} e^{-\pi\mathcal{K}R_c} \quad (3.3)$$

and a mass

$$M_\varphi^2 = \frac{2\mathcal{K}^2}{\hat{M}^3} (V_0 - V_\pi)^2 e^{-2\pi\mathcal{K}R_c} \quad (3.4)$$

Because of the warp factor  $e^{-\pi\mathcal{K}R_c}$ , both the radion mass  $M_\varphi$  and the radion vacuum expectation value  $\Lambda_\varphi$  lie at or around the electroweak scale. Hence, it is easier, for phenomenological purposes, to treat them as the free parameters in the theory, rather than the set  $\{\mathcal{K}, \hat{M}, V_0, V_\pi\}$ . It is also worth noting that if we let  $V_0 = V_\pi$ , in which case Eq. (3.4) tells us that the radion is massless, we would also have  $R_c = 0$  from Eq. (2.94), i.e. the two branes would coalesce and  $M_H$  immediately shoot up to  $\hat{M}$  — which takes us back to the Standard Model and the hierarchy problem. We conclude, therefore, that  $V_0 > V_\pi$  and hence the radion must be massive. We have also seen that its interactions with matter on the IR brane can be written as

$$\mathcal{L}_{\text{int}}(\varphi) = \frac{1}{\Lambda_\varphi} \varphi (T^\mu{}_\mu + \mathcal{A}_T) \quad (3.5)$$

where  $T_{\mu\nu}$  is the tree-level energy-momentum tensor and  $\mathcal{A}_T$  is the trace anomaly. For on-shell particles, the tree-level  $T^\mu{}_\mu$  has the explicit form

$$T^\mu{}_\mu = \sum_f m_f \bar{f} f + M_H^2 H^2 - 2M_W^2 W^{+\mu} W_\mu^- - M_Z^2 Z^\mu Z_\mu \quad (3.6)$$

where the sum runs over all fermions  $f$  and the anomaly term is

$$\mathcal{A}_T = \sum_i \frac{\beta(g_i)}{2g_i} F^{\mu\nu i} F_{\mu\nu}^i \quad (3.7)$$

where  $\beta(g_i)$  is the beta function corresponding to the coupling  $g_i$  of the gauge field  $A_i$  which has the field strength tensor  $F_{\mu\nu}^i$ . The sum over  $i$  runs over all the gauge fields in the SM, including photons, gluons and  $W^\pm$  and  $Z$  bosons. The  $\mathcal{A}_T$  term induces substantial couplings of the radion to  $\gamma\gamma$  and  $gg$  pairs, which are completely absent in Eq. (3.6). On the other hand, similar anomaly-induced contributions to radion couplings with  $W^+W^-$  and  $ZZ$  pairs are usually negligible compared to the corresponding terms in Eq. (3.6), because of the large masses of these particles, and only become significant when their tree-level couplings to one of the scalars vanishes.

The tree-level radion couplings in Eq. (3.5) would be subject, in addition to the trace anomaly contributions, to radiative corrections, especially from loops involving the top quark. Moreover, it is worth mentioning that there could be large brane corrections to the above couplings if the mass of the radion is comparable to the Kaluza-Klein scale [17–20], determined by the mass of the lightest graviton mode in the minimal RS construction. To avoid this, we require a radion which is comparatively light, and this requires a modest level of fine tuning [17–20]. The discussions in this thesis are, therefore, subject to this assumption.

As remarked above, the phenomenological behaviour of such a light radion is rather similar to that of the Higgs boson. This naturally leads one to ask whether these two low-lying elementary scalar states can *mix*, since they carry the same set of conserved quantum numbers, once the electroweak symmetry has been broken. In fact, this is possible, as was first pointed out in Ref. [21] and has been discussed by many others [21–23]. Before proceeding further, it may be noted that there are several phenomenological models with fermions and gauge bosons accessing the bulk [24–28], which have better control over the flavour problem. In these models, the top quark remains close to the TeV brane along with the Higgs field while the other fermions are close to the UV brane. This suppresses the higher-dimensional operators contributing to flavour-changing neutral currents, since the effective interaction of fermions with the Higgs field is governed by the overlap of their profiles and hence this scenario naturally generates the pattern of fermion masses and mixings. These models predict heavy Kaluza-Klein particles on the TeV brane having masses in the range of a TeV. However, the radion and Higgs fields, being still close to the TeV brane, mix more-or-less without bulk effects [29]. Hence, the mixing can be understood fairly accurately using a minimal model where all the relevant particles are confined to the TeV brane<sup>1</sup>, for this is, after all, no more than approximating a sharply-peaked function by a delta function.

In the following section, therefore, we briefly discuss, following Refs. [22,23] how the radion-Higgs field mixing may be described in terms of a single mixing parameter  $\xi$ . The next section then describes constraints on the mixed Higgs-Radion scenario, as obtained using all experimental

---

<sup>1</sup>The only caveat to this is the fact that heavy Kaluza-Klein excitations of the top quark may contribute to Higgs production at a hadron collider through loop diagrams. However, if these excitations are at the level of a TeV, the corresponding loop contributions are not more than a few percent and may be safely neglected — as we have done in this work.

inputs currently available, especially those from the LHC. For easy comparison, we include projections of the discovery reach of the LHC alongside the current constraints. While some of the observations in this work echo previous ones [30–47], the data used are current, leading to new bounds, and, for ease of reading, we have presented our findings in a manner such that this chapter can be read, as far as possible, independently of the preceding literature.

## 3.2 Radion-Higgs mixing

Mixing of the radion field  $\varphi(x)$  with the Higgs scalar  $h(x)$  of the SM has been discussed by several authors [21–23], with the same broad features, but we choose to closely follow the formalism of Ref. [22, 23].

The mixing occurs through the kinetic terms

$$\mathcal{L} = \frac{1}{2}\partial^\mu h \partial_\mu h - \frac{1}{2}M_h^2 h^2 + \frac{\beta}{2}\partial^\mu \varphi \partial_\mu \varphi - \frac{1}{2}M_\varphi^2 \varphi^2 + 6\gamma\xi \partial^\mu \varphi \partial_\mu h \quad (3.8)$$

where  $\gamma \equiv v/\Lambda_\varphi$ ,  $v$  being the SM Higgs vacuum expectation value. In this formalism, the mixing parameter appears twice – once in the mixing term  $6\gamma\xi \partial^\mu \varphi \partial_\mu h$ , and once in the non-canonical normalisation  $\beta \equiv 1+6\gamma^2\xi$  of the radion kinetic term. As is usual, the Higgs boson mass is given by  $M_h^2 = 2\lambda v^2$ , where  $\lambda$  is the Higgs quartic coupling and  $v$  is the Higgs vacuum expectation value.

We note that the presence of the non-canonical normalisation  $\beta$  means that the identification of physical states  $H$  and  $\Phi$  will involve a scaling as well as a rotation of states, i.e. a non-unitary transformation. Hence, we write the unphysical states  $\varphi, h$  as linear combinations of the physical ones  $\Phi, H$ , with real coefficients  $A, B, C$  and  $D$ , thus

$$\begin{aligned} \varphi &= A\Phi + BH \\ h &= C\Phi + DH, \end{aligned} \quad (3.9)$$

where the coefficients  $A, B, C$  and  $D$  are given by

$$\begin{aligned} A &= -\frac{1}{Z}\cos\theta & B &= \frac{1}{Z}\sin\theta \\ C &= \sin\theta + \frac{6\gamma\xi}{Z}\cos\theta & D &= \cos\theta - \frac{6\gamma\xi}{Z}\sin\theta \end{aligned} \quad (3.10)$$

in terms of

$$Z^2 = \beta - (6\gamma\xi)^2 \quad (3.11)$$

and a mixing angle  $\theta$ , defined by

$$\tan 2\theta = \frac{12\gamma\xi Z M_h^2}{M_\varphi^2 - M_h^2 (Z^2 - 36\gamma^2\xi^2)} \quad (3.12)$$

The mixing parameter  $\xi$  is immediately constrained by the requirement that  $Z^2 > 0$  to get a real mixing angle. The mass eigenvalues of the physical eigenstates  $\Phi$  and  $H$  are now given by

$$M_{\Phi,H}^2 = \frac{1}{2Z^2} \left( M_\varphi^2 + \beta M_h^2 \pm \sqrt{(M_\varphi^2 + \beta M_h^2)^2 - 4Z^2 M_\varphi^2 M_h^2} \right) \quad (3.13)$$

where the sign is chosen to ensure that  $M_H < M_\Phi$ . We identify the lighter state  $H$  as the scalar state of mass around 125 GeV which was discovered at the CERN LHC in 2012, while the other state  $\Phi$  is a heavier scalar state predicted in the model. From these formulae, it is clear that the free parameters in question are  $M_h$ ,  $M_\varphi$ ,  $\Lambda_\varphi$  and  $\xi$ , everything else being computable in terms of them. We also note in passing that since  $M_h^2 = 2\lambda v^2$ , this makes the Higgs quartic coupling  $\lambda$  an unknown quantity in this model, just as it used to be in the Standard Model before the identification of the 125 GeV scalar with the Higgs boson<sup>2</sup>.

Instead of the Lagrangian parameters  $M_h$  and  $M_\varphi$ , however, we find it more convenient to use the physical masses  $M_H$  and  $M_\Phi$ , which can be traded for the previous two by some simple algebra, leading to

$$\begin{aligned} M_\varphi^2 &= \frac{Z^2}{2} \left[ M_\Phi^2 + M_H^2 + \sqrt{(M_\Phi^2 + M_H^2)^2 - \frac{4\beta M_\Phi^2 M_H^2}{Z^2}} \right] \\ M_h^2 &= \frac{Z^2}{2\beta} \left[ M_\Phi^2 + M_H^2 - \sqrt{(M_\Phi^2 + M_H^2)^2 - \frac{4\beta M_\Phi^2 M_H^2}{Z^2}} \right] \end{aligned} \quad (3.14)$$

Since we identify  $M_H = 125$  GeV, we are left with a set of only three independent parameters, viz.  $M_\Phi$ ,  $\Lambda_\varphi$  and  $\xi$ . The rest of our analysis will be presented in terms of these variables.

We now have another theoretical constraint, apart from  $Z^2 > 0$ . This is the requirement that the parameters  $M_\varphi$  and  $M_h$  be real (to keep the Lagrangian Hermitian), which automatically means that

$$(M_\Phi^2 + M_H^2)^2 > \frac{4\beta M_\Phi^2 M_H^2}{Z^2} \quad (3.15)$$

Imposing both these constraints reduces the possible range of  $\xi$ , for a given  $M_\Phi$  and  $\Lambda_\varphi$ , quite significantly (see below).

Since the mixing of the  $h$  and the  $\varphi$  to produce the physical  $H$  and the  $\Phi$  is non-unitary, we define two mixing indicators as follows. We first invert Eq. (3.9) to write

$$\begin{aligned} \Phi &= a\varphi + bh \\ H &= c\varphi + dh, \end{aligned} \quad (3.16)$$

where

$$\begin{pmatrix} a & b \\ c & d \end{pmatrix} = \begin{pmatrix} A & B \\ C & D \end{pmatrix}^{-1}. \quad (3.17)$$

In terms of this, we now define indicators

$$f_{\varphi/H} = \frac{|c|}{|c| + |d|} \quad f_{h/\Phi} = \frac{|b|}{|a| + |b|} \quad (3.18)$$

which, in a sense, indicate the fraction of radion  $\varphi$  in the light state  $H$ , and the fraction of Higgs boson  $h$  in the heavy state  $\Phi$ . These, together with the mixing angle  $\theta$  defined in Eq. (3.12), are plotted in Figure 3.1, as a function of the mixing parameter  $\xi$ .

---

<sup>2</sup>This is a reflection of the fact that we still do not have a direct measurement of  $\lambda$ . All that we have is the estimate  $\lambda = (125 \text{ GeV})^2/2v^2 \simeq 0.129$  — which is true only if the 125 GeV state is purely a SM Higgs boson without any admixture of new states.

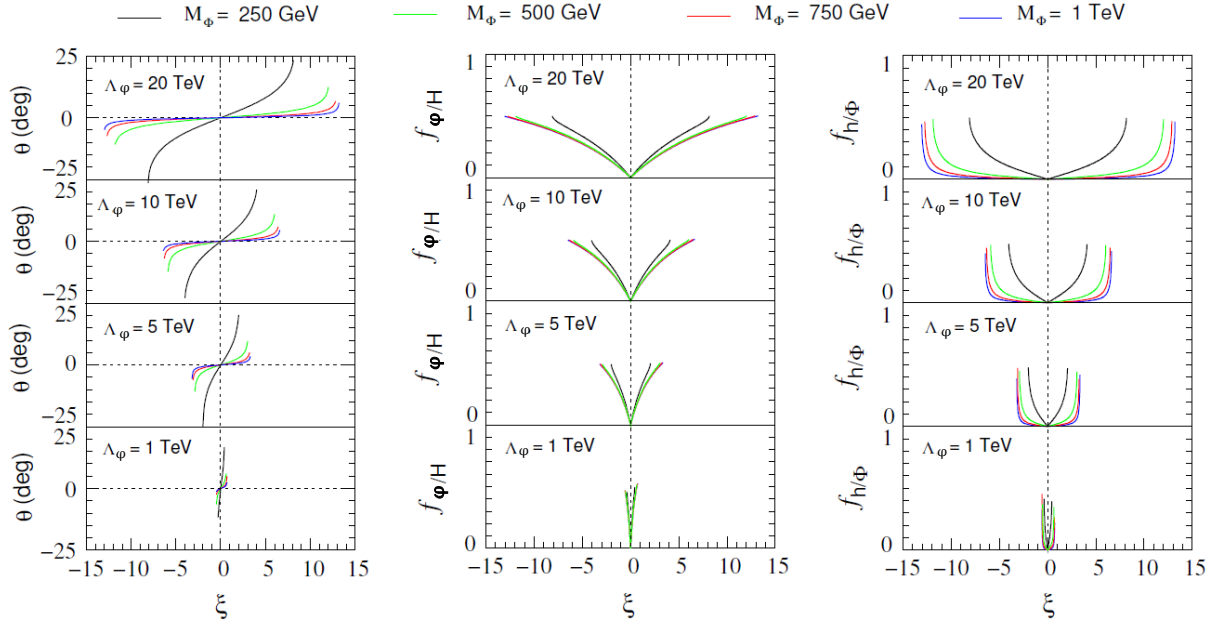


**Figure 3.1:** The variation with  $\xi$  of the mixing parameters (a)  $\theta$ , (b)  $f_{\phi/H}$  and (c)  $f_{h/\phi}$ . In each panel, the four boxes, from bottom to top, show the behaviour when  $\Lambda_\phi = 1, 5, 10$  and  $20$  TeV respectively, as marked. Inside the boxes, the curves are coloured black, green, red and blue for  $M_\Phi = 250$  GeV,  $500$  GeV,  $750$  GeV and  $1$  TeV respectively. Observe that all these parameters vanish when  $\xi = 0$ , as expected. The lines break off abruptly for larger values of  $|\xi|$  because of the theoretical constraints discussed in the text.

In each of the three panels in Figure 3.1, we have four boxes placed one above the other, corresponding to choices of four different values of the radion vacuum expectation value, viz.  $\Lambda_\phi = 1, 5, 10$  and  $20$  TeV respectively (marked in the respective boxes). Within each box, the curves are colour-coded, with black, green, red and blue indicating benchmark choices of the heavy scalar mass as  $M_\Phi = 250$  GeV,  $500$  GeV,  $750$  GeV and  $1$  TeV respectively (indicated at the top of the figure). Each curve ends abruptly at some maximum and minimum values of the mixing parameter  $\xi$  – this is a reflection of the theoretical limitations (see above). As may be seen from the different plots, this restriction is extremely stringent when  $\Lambda_\phi$  is small, and even when we push  $\Lambda_\phi$  as high as  $20$ , does not permit the value of  $|\xi|$  to exceed  $15$ . If we consider the panel on the left, it is clear that we get significant values of the mixing angle  $\theta$  only when the heavy  $\Phi$  state is as light as around  $250$  GeV. For values of  $M_\Phi$  of  $500$  GeV or greater,  $\theta$  does not exceed  $10^\circ$ . However, since the mixing is not unitary, the smallness of  $\theta$  is not necessarily an indicator of small mixing. This becomes clear if we look at the central and right panels of Figure 3.1, which tell us the proportion of the radion in the  $125$  GeV state, and the proportion of the Higgs boson in the heavier state respectively. In each case, as  $|\xi|$  increases, the mixing becomes more, starting from zero when  $|\xi| = 0$  to about equal mixtures when  $|\xi|$  reaches its maximum theoretically-permitted value. The purpose of this chapter is, as explained above, to see how far such large mixings are allowed in the light of current experimental data.

We next consider the effect of mixing on the couplings of the two scalar states to the SM fields. As shown in Ref. [23], the tree-level couplings of the heavy  $\Phi$  state to pairs of SM fields  $X\bar{X}$  (except  $X = H$ ) have the form

$$g_{\Phi X\bar{X}} = g_{\phi X\bar{X}} (C + \gamma A) \equiv c_\Phi g_{\phi X\bar{X}} \quad (3.19)$$

where  $g_{\phi X\bar{X}}$  can be read off from Eqs. (3.5–3.6), and  $c_\Phi = C + \gamma A$  is a scaling factor. Similarly,

the couplings of the light 125 GeV state have the form

$$g_{HX\bar{X}} = g_{hX\bar{X}} (D + \gamma B) \equiv c_H g_{hX\bar{X}} \quad (3.20)$$

where  $g_{hX\bar{X}}$  are the SM couplings and  $c_H = D + \gamma B$  is a scaling factor. Very different from these is the coupling of the heavy scalar to a pair of light scalars, since all three fields are mixed states, and this can be written [23] for a  $\Phi(p) - H(k_1) - H(k_2)$  vertex, as

$$g_{HH} = \frac{1}{\Lambda_\phi} [(k_1^2 + k_2^2) \{AD^2 + 6\xi B(CD + \gamma AD + \gamma BC)\} + D \{12\gamma\xi AB + 2BC + (6\xi - 1)AD\} p^2 - 4M_h^2 D(AD + 2BC) - 3M_h^2 CD^2/\gamma] \quad (3.21)$$

The couplings of the scalars  $H$  and  $\Phi$  with other particles are conveniently listed in the Appendix of Ref. [23].

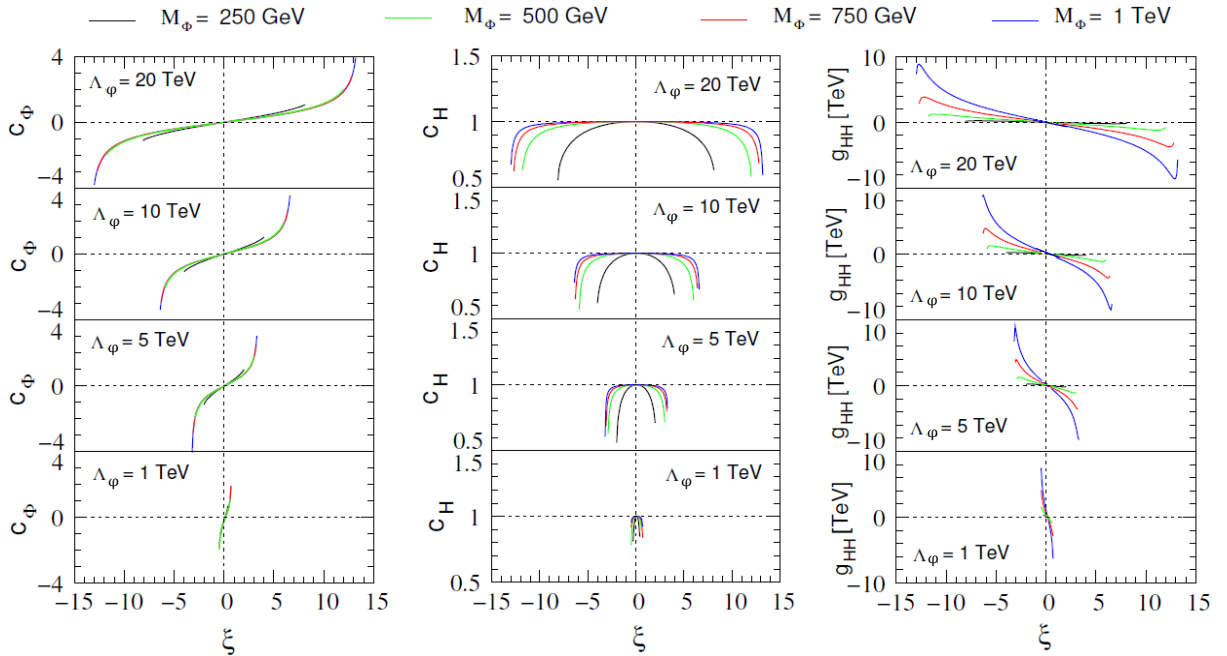


**Figure 3.2:** The variation with  $\xi$  of the (dimensionless) scaling factors (a)  $c_\Phi$  and (b)  $c_H$  is shown in the left and central panels, while the right panel shows the  $\Phi HH$  coupling  $g_{HH}$ , in units of TeV. The layout and colour conventions of this figure closely follow those of Figure 3.1.

To get a feeling of how these couplings are affected by the variation in the basic parameters  $\xi$ ,  $\Lambda_\phi$  and  $M_\Phi$ , we plot them in Figure 3.2 on a scheme similar to that in Figure 3.1. The three panels show, from left to right, the scaling factors  $c_\Phi$  and  $c_H$ , and the coupling  $g_{HH}$  respectively. As in Figure 3.1 it is immediately clear that for  $\xi = 0$ ,  $c_\Phi$  is very small (small enough to appear as zero on this scale), as befits a radion with a small coupling to matter, whereas  $c_H = 1$  indicating that the lighter scalar is the SM Higgs boson. Similarly, for  $\xi = 0$ , the  $g_{HH}$  coupling is very small (small enough to appear as zero on this scale), indicating that the heavy scalar couples only weakly to a pair of light scalars. There are also genuine zeroes in the couplings, which are discussed in more detail in the next chapter.

An interesting feature of both Figure 3.1 and Figure 3.2 is the fact that the variation in parameters is rather slow for smaller values of  $\xi$ , but is very sharp for larger values just before

the unphysical region. These larger values of the scaling factor and  $\Phi HH$  coupling are likely to have phenomenological consequences at observable levels, and hence are more likely to be constrained by experimental data. In the next section, we shall see that this is indeed the case.

### 3.3 Experimental Constraints

We are now in a position to apply the experimental constraints to this model. Since the two scalars  $H$  and  $\Phi$  are the crucial elements, the main constraints will come from

- (a) the measured signal strengths  $\mu_{XX}$  of the 125 GeV scalar in its decay channels to  $X\bar{X}$  pairs – these are known to match reasonably closely to the SM predictions, leaving only limited room for a mixed state;
- (b) the lack of signals for a heavy scalar in the range of a few hundred GeV to about a TeV – by implication, any new scalar would be very heavy and mix only marginally with the SM Higgs boson.

In principle, the scalars could also contribute as virtual states to any neutral current processes. However, as most of these are suppressed by the small masses of the initial states (either  $e^\pm$  or  $u$  and  $d$  quarks), we do not really get any useful constraints from these processes. Constraints from electroweak precision tests are not very strong [22, 48]. In the rest of this sections, therefore, we concentrate on the two issues listed above.

Signal Strength	8 TeV limits	13 TeV limits
$\mu_{\gamma\gamma}$	0.68 – 1.70 [49]	$\left\{ \begin{array}{l} 0.31 – 1.27 [50] \text{ (CMS)} \\ 0.03 – 1.17 [51] \text{ (ATLAS)} \end{array} \right.$
$\mu_{WW}$	0.58 – 1.42 [49]	—
$\mu_{ZZ}$	0.76 – 2.16 [49]	0.78 – 1.62 [52] (CMS)
$\mu_{\tau\tau}$	0 – 2.26 [49]	—
$\mu_{bb}$	0 – 3.13 [49]	0 – 1.23 [53] (ATLAS)

**Table 3.1:** LHC results on the Higgs signals strengths at 95% confidence level. The 8 TeV limits are from ATLAS and CMS combined. Production is through gluon fusion, except for the last entry, which is through vector boson fusion.

We first take up the signal strengths of the 125 GeV scalar  $H$ . This decays into several channels

$$H \longrightarrow X + \bar{X} \quad (3.22)$$

where  $X = \ell^-, u, d, s, c, b, W, Z, \gamma, g$  with one of  $X$  or  $\bar{X}$  being off-shell in the case of  $W$  and  $Z$ . At the LHC, the  $H$  is produced dominantly through gluon-gluon fusion<sup>3</sup>. Hence, we can define signal strengths  $\mu_{XX}$  as

$$\mu_{XX} = \frac{\sigma(pp \rightarrow gg \rightarrow H)_{\text{exp}} \mathcal{B}(H \rightarrow X\bar{X})_{\text{exp}}}{\sigma(pp \rightarrow gg \rightarrow H)_{\text{SM}} \mathcal{B}(H \rightarrow X\bar{X})_{\text{SM}}} \quad (3.23)$$

where  $\sigma$  and  $\mathcal{B}$  stand for cross-section and branching ratio respectively, and the subscripts ‘SM’ and ‘exp’ mean the SM prediction and the experimental value respectively. If we are making

<sup>3</sup>In our numerical analysis, we have also included the vector boson fusion mode.

a theoretical prediction, then ‘exp’ will stand for the expected value in the theoretical model in question — in the present case, the model with radion-Higgs mixing. Of course, in an experiment only the entire numerator on the right side of Eq. (3.23) can be measured and not the individual factors. By this definition, then, all the SM signal strengths are normalised to unity, and experimental deviations from it constitute the leeway for new physics. These allowed experimental deviations are given in Table 3.1.

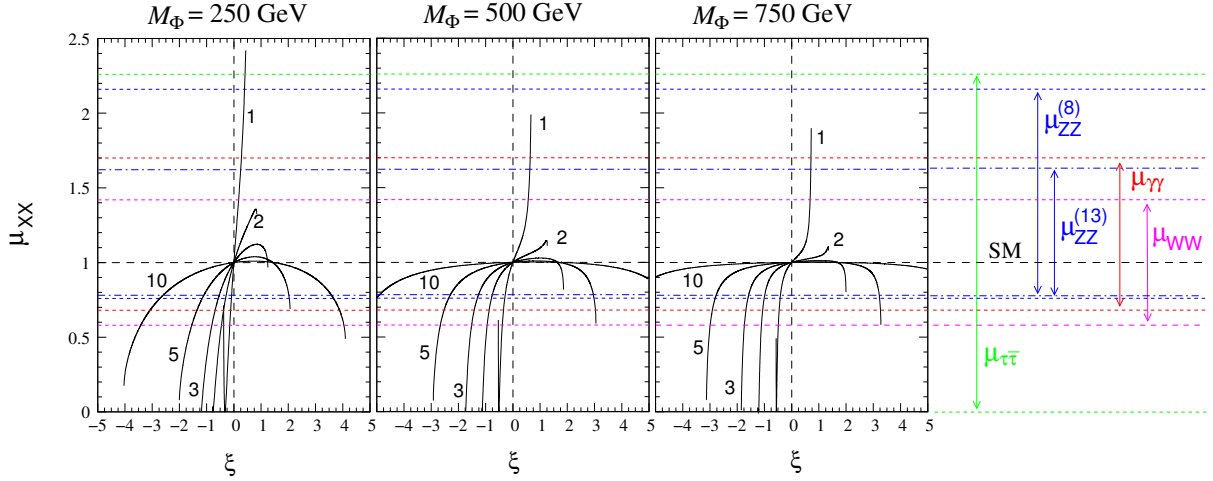


**Figure 3.3:** The variation of the predicted signal strengths with the mixing parameter  $\xi$ , for different choices of  $\Lambda_\varphi$  (in TeV), marked alongside each curve. Each panel corresponds to a different mass  $M_\Phi$  as marked. The experimental constraints at 95% C.L. are shown on the right. Superscripts (8) and (13) indicate results from Run-1 and Run-2 respectively of the LHC.

Obviously, for zero mixing, the signal strengths predicted for the  $H$  scalar will be the same as the SM values, i.e. unity. As  $\xi$  increases, we should expect deviations from unity, and indeed that is what happens, as illustrated, in Figure 3.3. The three panels, from left to right, correspond to choices of  $M_\Phi = 250, 500$  and  $750$  GeV respectively. The graph for  $M_\Phi = 1$  TeV is very similar to that for  $M_\Phi = 750$  GeV, and hence we do not show it explicitly. Likewise, the actual graphs for  $\mu_{\gamma\gamma}$  are slightly different, but not enough to show up on a plot at this scale. Each curve in the panels corresponds to the value of  $\Lambda_\varphi$ , in TeV, written alongside, i.e. 1, 2, 3, 5 and 10 TeV respectively. The steepness of the curves decreases with increasing  $\Lambda_\varphi$ , for which we also have larger permitted ranges in  $\xi$ , as we have earlier shown in Figure 3.2. Horizontal broken lines in Figure 3.3 represent the useful 95% C.L. constraints from the signal strengths in Table 3.1, and are marked on the right side of the figure.

The behaviour of the predicted signal strengths with increasing  $\xi$  is quite as expected, remaining close to the SM value for small  $\xi$  and showing large deviations near the edge of the theoretically-allowed range. This, as we have seen earlier, is due to the large deviations of the coupling of the  $H$  from the SM coupling at such values of  $\xi$ . It is thus obvious that the present constraints from signal strengths will only affect narrow strips of the parameter space adjacent to the theoretically-disallowed region, and this, in fact, is what we find (see below). It may be noted in passing that a region of the parameter space where  $D + \gamma B \simeq 0$  would be very strongly constrained from the signal strengths, but this does not happen anywhere inside the region allowed by theoretical considerations.

When we turn to the heavy  $\Phi$  state, once again the main production mode is through gluon-

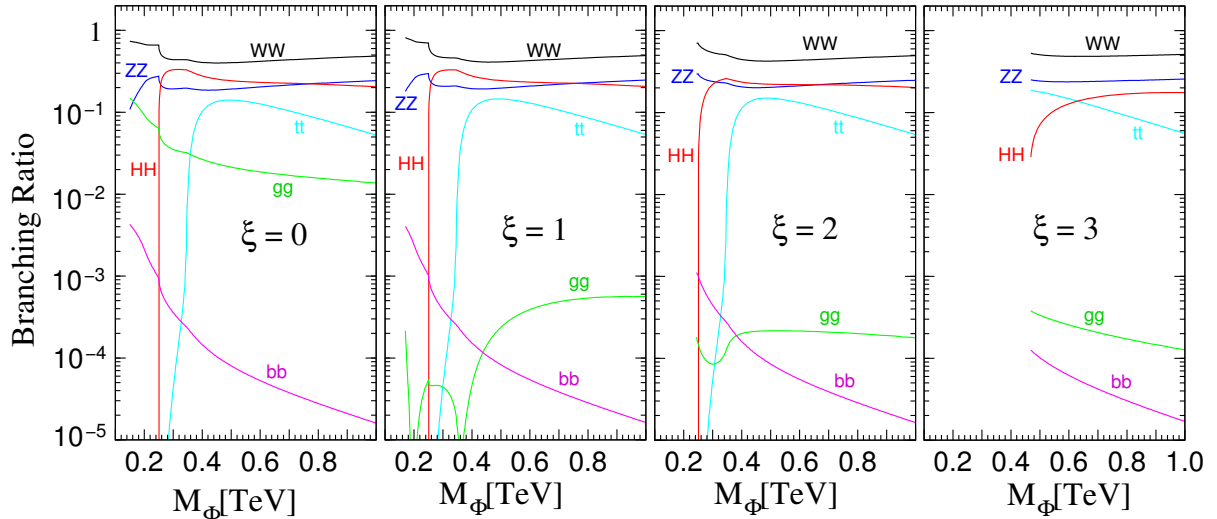


**Figure 3.4:** Two-body branching ratios of the heavy scalar  $\Phi$  as a function of its mass  $M_\Phi$ , for different choices of the mixing parameter  $\xi = 0, 1, 2$  and  $3$ . The extreme left panel, viz.  $\xi = 0$ , corresponds to a pure radion state. Branching ratios for the diphoton channel are not shown as they are too small to appear on the chosen scale. For these plots, we have set  $\Lambda_\phi = 5$  TeV. Variation with  $\Lambda_\phi$  exists, but is slight.

gluon fusion, but now there is no analogous SM prediction and hence one looks for the direct signals in the various decay channels of the  $\Phi$ . As in the case of the light scalar, the potentially observable ones are  $\Phi \rightarrow \gamma\gamma$  [54–56],  $WW$  [57–60],  $ZZ$  [58, 61–63] and  $\tau^+\tau^-$  [64–67] to which we can now add  $\Phi \rightarrow t\bar{t}$  and  $\Phi \rightarrow HH$  [68–78]. The  $b\bar{b}$  [79] signal would be difficult to distinguish from the QCD background, unless the mass of the  $\Phi$  scalar is very well known, as in the case of the  $H$  scalar. The behaviour of all these branching ratios, as functions of the scalar mass  $M_\Phi$  is shown in Figure 3.4, where  $\Lambda_\phi$  is fixed to 5 TeV and the panels, from left to right, correspond to  $\xi = 0$  (no mixing), and  $\xi = 1, 2$  and  $3$  respectively. The relevant decay channel is marked alongside each curve. These curves terminate at the left end where they correspond to theoretically-disallowed regions in the parameter space.

One feature which is immediately obvious from these curves is the fact that the scalar  $\Phi$  decays dominantly through the  $WW$  and  $ZZ$  channels. When the mixing is low, the  $HH$  channel is also competitive, but as  $\xi$  rises, it gets suppressed. In any case, the signals from the  $WW$  and  $ZZ$  channels are leptonic and clean, whereas the signals arising from  $HH$ , dominantly leading to  $4b$  final states, are hadronic, as are those arising from the direct decays of the  $\Phi$  into quark pairs. These hadronic channels are generally suppressed compared to  $WW$  and  $ZZ$ , and, in any case, would be plagued by large QCD backgrounds. It may be still possible to investigate the  $t\bar{t}$  and  $HH$  channels, using jet substructure-based tagging methods for boosted particles, but such experimental searches are still not competitive [80]. Thus, in principle, we get constraints from every decay channel of the  $\Phi$ , but the most useful ones will arise from the ATLAS and CMS search results for a heavy scalar resonance decaying to  $WW$  and  $ZZ$  pairs, which are equally applicable to the  $\Phi$  scalar in the model under consideration. As is well-known, the experimental results are all negative, and hence the 95% C.L. upper limits on the cross-section are given in Table 3.2.

We are now in a position to compare these data with the predictions of our theory. As in the

$pp \rightarrow S \rightarrow WW$	$M_S = 250$ GeV	$M_S = 500$ GeV	$M_S = 750$ GeV	$M_S = 1$ TeV
ATLAS (Run I) [57]	—	0.191	0.039	0.020
CMS (Run I) [58]	1.590	0.287	0.221	0.064
ATLAS (Run II) [59]	—	0.884	0.253	0.066
CMS (Run II) [60]	51.395	4.866	2.882	1.708
$pp \rightarrow S \rightarrow ZZ$	$M_S = 250$ GeV	$M_S = 500$ GeV	$M_S = 750$ GeV	$M_S = 1$ TeV
ATLAS (Run I) [61]	0.298	0.044	0.012	0.011
CMS (Run I) [58]	0.110	0.089	0.040	0.025
ATLAS (Run II) [62]	0.758	0.111	0.068	0.050
CMS (Run II) [63]	0.416	0.136	0.070	0.060

**Table 3.2:** LHC 95% upper limits on the cross-section, in pb, for a heavy scalar  $S$  decaying to a  $WW$  or a  $ZZ$  pair, for the benchmark values  $M_S = 250, 500, 750$  and  $1000$  GeV respectively. In our work, we have used only the Run-2 data for the constraints.

case of the  $H$  state, the cross-section for  $pp \rightarrow \Phi \rightarrow VV$ , where  $V = W, Z$ , can be written

$$\sigma(pp \rightarrow \Phi \rightarrow VV) = \sigma(pp \rightarrow gg \rightarrow \Phi) \mathcal{B}(\Phi \rightarrow VV) \quad (3.24)$$

where  $\mathcal{B}(\Phi \rightarrow VV)$  is the branching ratio of the  $\Phi$  to a  $VV$  pair. These can be calculated in terms of the free parameters  $\xi$ ,  $M_\Phi$  and  $\Lambda_\varphi$  respectively. Our results are shown in Figure 3.5.

The four upper panels of Figure 3.5 represent the cross-section, in pb, for the process  $pp \rightarrow \Phi \rightarrow WW$  and the lower four panels represent the process  $pp \rightarrow \Phi \rightarrow ZZ$ . In each row the panels correspond, from left to right, to  $M_\Phi = 250$  GeV, 500 GeV, 750 GeV and 1 TeV, respectively. Within each panel, the curves show the variation of the cross-section with the mixing parameter  $\xi$ , for different values of the radion vacuum expectation value, corresponding to different colours, as marked in the legend above the panels. The horizontal solid lines correspond to the CMS bounds from the 13 TeV data, as shown in Table. 3.2, while the broken lines correspond to the ATLAS 13 TeV data.

All the curves have a distinct minimum at a small value of  $\xi$  varying from 0.2 to 2 — this corresponds to a minimum in the cross-section  $\sigma(pp \rightarrow gg \rightarrow \Phi)$  where there is maximal cancellation in the amplitude for  $gg \rightarrow \Phi$  due to the top quark loop and the trace anomaly term. In this region, the heavy scalar can be produced in association with a  $W^\pm/Z$  and it further decays to  $WW$  or  $ZZ$  pairs, leading to a final state with three gauge bosons or their decay products. In view of the low production cross-sections for higher values of  $\Lambda_\varphi$ , one has to consider hadronic decays of one or more of these gauge bosons, and this immediately invites a large QCD background at the LHC. However, the region can be successfully probed at a high energy  $e^+e^-$  collider (such as the proposed ILC) with  $\sqrt{s} = 1$  TeV [81].

In addition to the dip described above, there is a very sharp minimum, very close to the vertical axis, which corresponds to the so-called ‘conformal’ point, where  $c_\Phi \rightarrow 0$ . We defer the

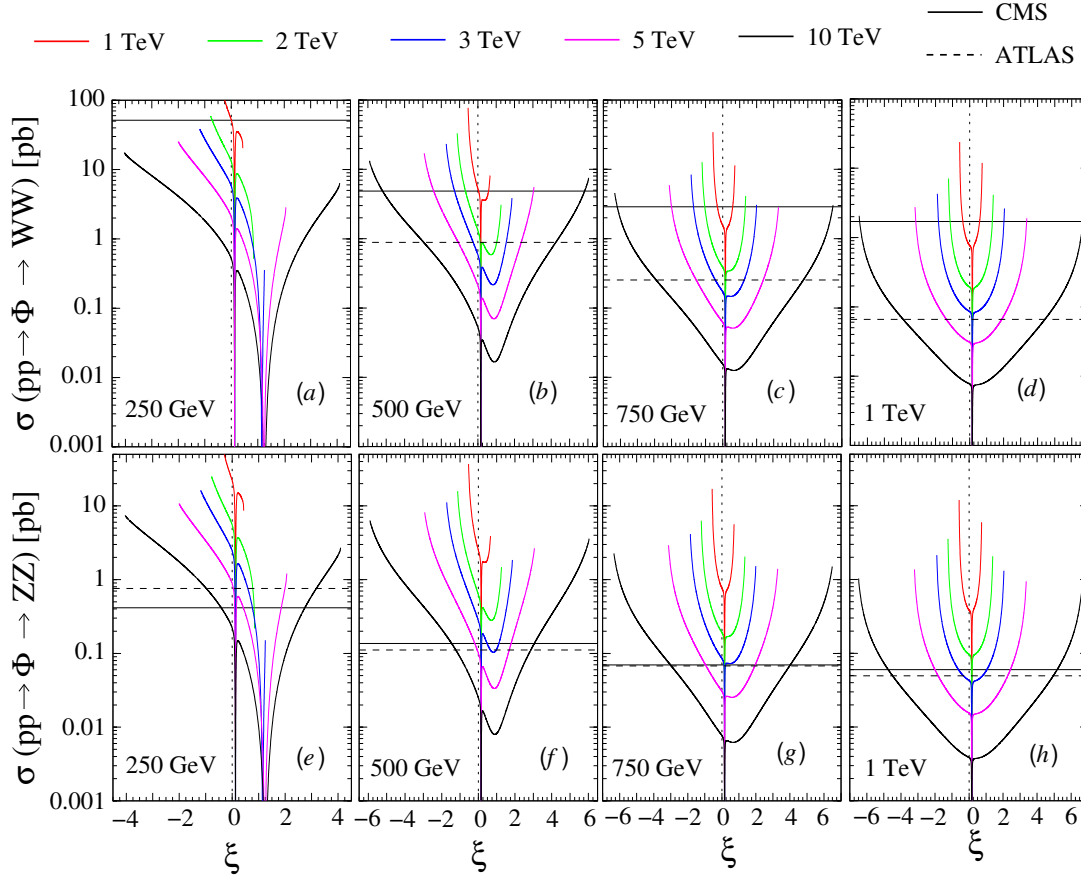


**Figure 3.5:** Predictions of this model vis-à-vis LHC searches for a heavy ‘SM-like’ scalar. The upper set of panels are for a  $WW$  final state and the lower set of panels are for a  $ZZ$  final state. Each panel shows the variation with  $\xi$  for a definite  $M_\Phi$  as marked, and the different curves correspond to different values of  $\Lambda_\varphi$ , as indicated in the legend above the panels. Horizontal solid (dashed) lines indicate the 95% C.L. CMS (ATLAS) 13 TeV constraints as in Table 3.2.

discussion of this point to the next chapter and focus here on the constraints obtainable from the rest of the parameter space. Here, as in the case of signal strengths the constraints rule out larger values of  $\xi$ , with the exact bound depending on the other two parameters of the theory.

From Figs. 3.3 and 3.5 we can draw some general conclusions. The first is that the effect of increasing the mixing parameter  $\xi$  becomes weaker and weaker as the vacuum expectation value  $\Lambda_\varphi$  keeps increasing. This is true both for the signal strengths in Figure 3.3 as well the cross-section in Figure 3.5 and is easy to track down as due to the limiting case  $\gamma \rightarrow 0$ . A similar argument may be made for the parameter  $M_\Phi$  – at least numerically – though the parameter dependence here is much more complicated. We may argue, therefore, that for a fixed  $\xi$ , the region with small  $M_\Phi$  and small  $\Lambda_\varphi$  is more constrained — which also corresponds to the commonsense argument that if these parameters are small, radion-mediated processes are large and vice versa. These expectations are corroborated by our results shown in Figure 3.6. Here we show the  $\Lambda_\varphi$ – $M_\Phi$  plane for four different values of  $\xi$ , viz.  $\xi = -0.5, 0, 1$  and  $1.5$ , as marked on each panel. As indicated in the key at the top, the region shaded grey corresponds to the theoretically disallowed region, and includes all values of  $\Lambda_\varphi < 1$  TeV, except in the panel on the top left, marked  $\xi = 0$ , which corresponds to the case of an un-mixed radion of mass  $M_\Phi$ . Here, though values of  $\Lambda_\varphi < 1$  TeV are theoretically permitted, the experimental constraints do not allow them, as is apparent from the figure. In all the panels, the dark grey shaded region is

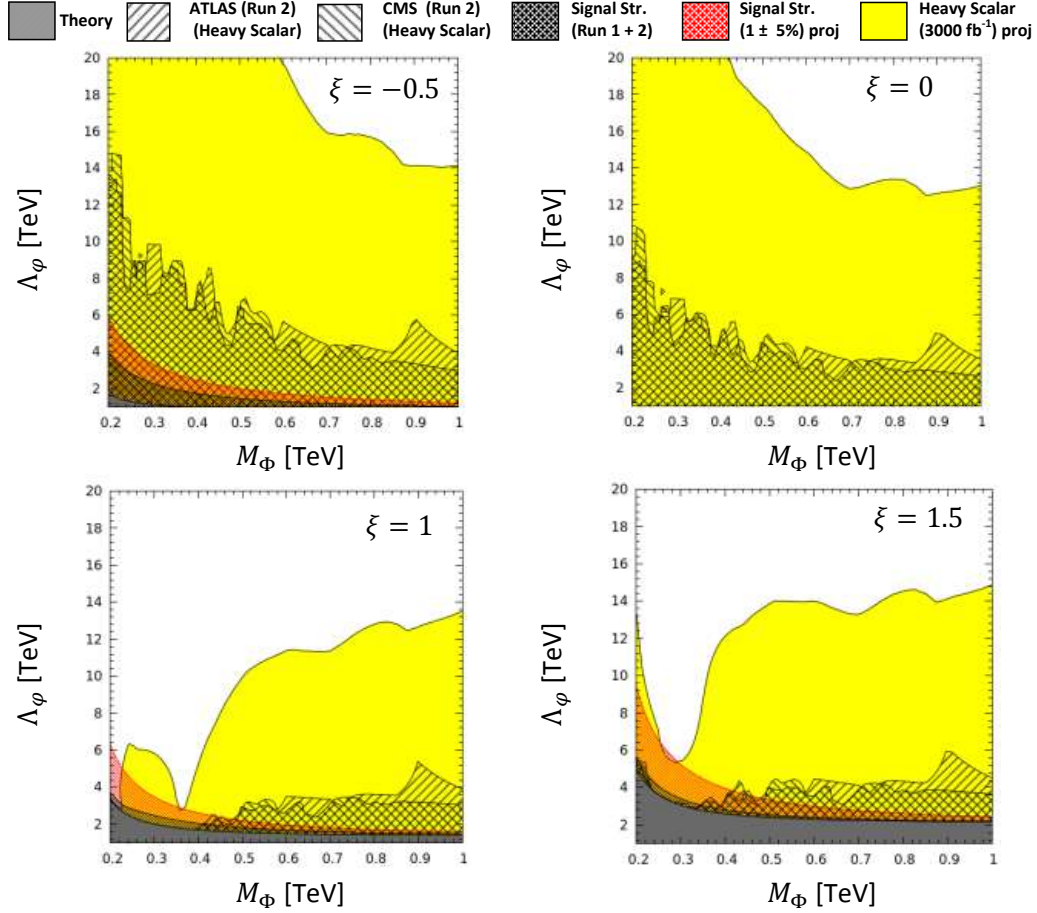


**Figure 3.6:** Constraints from LHC data on the  $\Lambda_\phi$ - $M_\Phi$  plane for different values of the mixing parameter  $\xi$ . The region shaded grey is theoretically disallowed and the region shaded dark grey is ruled out by the Higgs boson signal strengths. Hatching with opposite slants correspond to the ATLAS and CMS constraints from the heavy scalar search. The red-shaded region represents a projection of constraints from the signal strengths, assuming  $\mu_{XX} = 1 \pm 0.05$  for all channels. Finally, the yellow-shaded region represents a combination of the ATLAS and CMS projected discovery limits from the  $ZZ$  channel, assuming a data collection of  $3000 \text{ fb}^{-1}$  at 14 TeV.

ruled out by the signal strengths at Runs 1 and 2 and the hatched regions by the ATLAS and CMS searches for a heavy scalar at Run-2 of the LHC. These are the strongest constraints and represent the state of the art as far as current experimental data are concerned<sup>4</sup>. The jagged shape of the curves reflects the fact that the LHC has, till now, collected quite a small amount of data for rare processes like the decay of a heavy scalar. However, the LHC has the potential to search much further, and this is shown by the red and yellow-shaded regions, which represent, respectively, the expectations from the signal strength measurements if  $\mu_{XX} = 1 \pm 0.05$  for all  $X$ , and the ATLAS and CMS discovery limits at 95% C.L. for the heavy  $\Phi$  if the LHC were to run at 14 TeV and collect  $3000 \text{ fb}^{-1}$  of data [82, 83] — which may not be too far from the reality. For the panel with  $\xi = 0$ , there are no constraints from the signal strengths, since the  $H$  is completely SM-like; but the constraints from the heavy scalar searches are quite strong because that scalar is a pure radion. A comparative study of the four plots indicates that the value

<sup>4</sup>We have, in fact, considered constraints from all the channels separately, but the others are subsumed in the ones shown in the figure, and hence are not shown in order to have uncluttered figures.

$\xi \approx 1$  would permit the largest part of the parameter space to survive consistently negative results from LHC, while negative values of  $\xi$  are better suited to a discovery of the heavy scalar predicted in this theory.

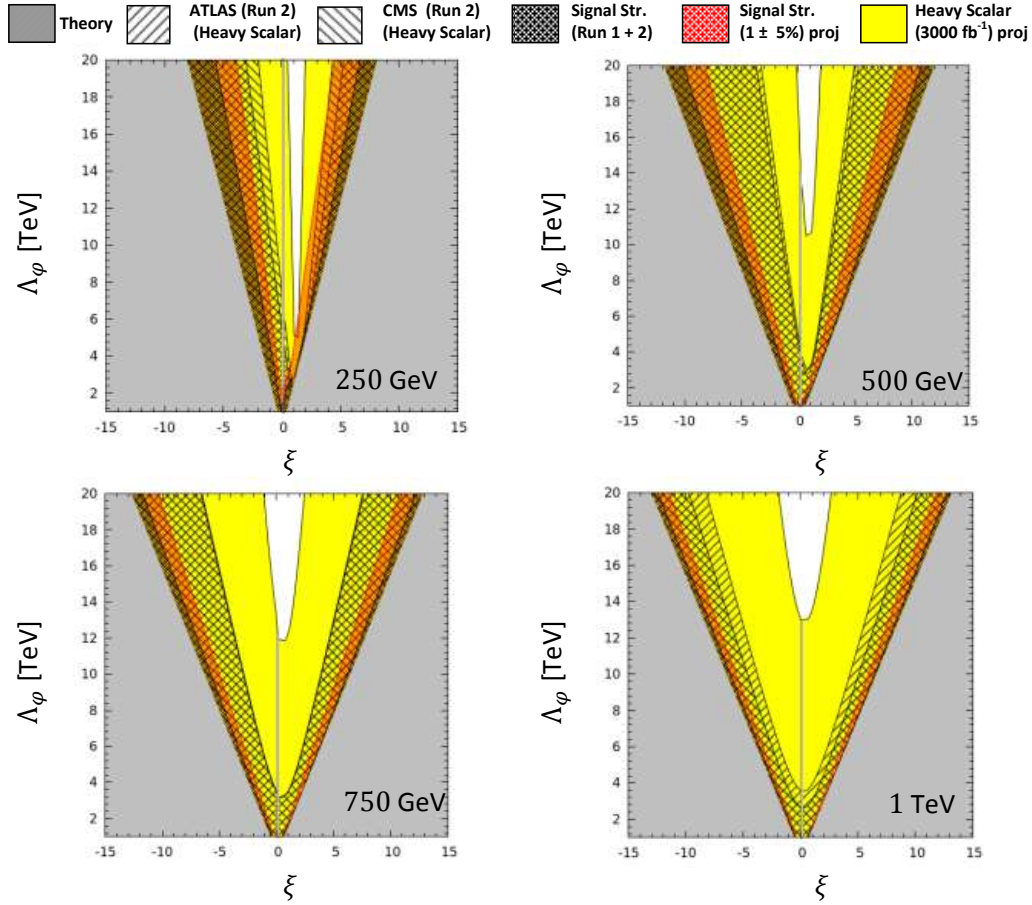


**Figure 3.7:** Constraints from LHC data on the  $\Lambda_\varphi$ - $\xi$  plane for different values of the heavy scalar mass  $M_\Phi$ . The region shaded grey is theoretically disallowed and the region shaded dark grey is ruled out by the Higgs boson signal strengths. Hatching with opposite slants correspond to the ATLAS and CMS constraints from the heavy scalar search. As in Figure 3.6, the red-shaded region represents a projection of constraints from the signal strengths, assuming  $\mu_{XX} = 1 \pm 0.05$  for all channels and the yellow-shaded region represents a combination of the ATLAS and CMS projected discovery limits, assuming a data collection of  $3000 \text{ fb}^{-1}$  at 14 TeV.

Coming to constraints on  $\xi$ , it is clear from Figs. 3.3 and 3.5 that  $\xi = 0$ , which corresponds to the 125 GeV scalar being the Standard Model Higgs boson — not surprisingly — is always allowed by the signal strength data. For given values of  $M_\Phi$  and  $\Lambda_\varphi$ ,  $\xi$  can range on the positive and negative side, but when its magnitude grows larger, all new physics effects grow and, at some point, higher magnitudes of  $\xi$  get disallowed — first by the experimental constraints and then by the requirement of theoretical consistency. For low values of  $\Lambda_\varphi$  and  $M_\Phi$ , we arrive at this point for fairly low values of  $\xi$ . As both these parameters increase, however, the allowed range grows, creating a funnel-like shape, which grows wider as  $\Lambda_\varphi$  and  $M_\Phi$  increase. This is illustrated in Figure 3.7, where we show the  $\Lambda_\varphi$ - $\xi$  plane for the same choices of  $M_\Phi$  as in the earlier figures. The shading and hatching conventions of this figure are exactly the same as those of Figure 3.6. It is immediately obvious that for low values of  $\Lambda_\varphi$  close to 1 TeV, the range of  $\xi$  is severely constrained by theoretical consistency alone. A heavy scalar of mass 250 GeV is also rather severely constrained, except for a narrow cone, which will shrink further when the

LHC finishes its run. Constraints ease up for a heavier scalar, since that is much more difficult to find. It is interesting that even if LHC completes its run without finding any evidence for a heavy scalar up to 1 TeV, there will be a range of parameter space where this model is still allowed. However, for these parameters, the 125 GeV will be so similar to the SM Higgs boson, and the interactions of the heavy scalar will be so heavily suppressed that the model may no longer be interesting, at least from a phenomenological point of view.

An interesting feature of all the plots in Figure 3.7 is the needle-thin sliver of allowed parameter space which appears in every graph close to the vertical axis. This corresponds, in every case, to the ‘conformal point’ mentioned above, where all constraints from a heavy scalar search weaken considerably.

### 3.4 Summary and Outlook

The minimal Randall-Sundrum model continues to be one of the most elegant ways of solving the hierarchy problem, and it works best if there is a Goldberger-Wise stabilisation, which works best if there is a light radion state. Though there are strong constraints on such a light radion per se, there remains room for a light radion mixed with the SM Higgs boson to survive. In this thesis, we have explored this possibility, using an existing formalism, in the light of current data from the LHC Runs 1 and 2. Our findings are summarised below.

The possibility of a radion-Higgs mixing arises essentially because we have no independent measurement of the Higgs boson self coupling  $\lambda$ , so that the SM formula  $M_h^2 = 2\lambda v^2$  is open to other interpretations. One of these is the mixed radion-Higgs scenario, where the lighter eigenstate is identified with the 125 GeV scalar discovered at the LHC. In this model, there are three free parameters, viz. the mixing parameter  $\xi$ , the mass  $M_\Phi$  of the heavy scalar  $\Phi$ , and the radion vacuum expectation value  $\Lambda_\varphi$ . However, self-consistency of the theory imposes fairly stringent constraints on the choices of the mixing parameter  $\xi$ . These, as we show, are further constrained by (a) the signal strengths measured for the decays of the 125 GeV scalar at the LHC, and (b) the search for a heavy scalar decaying into a pair of electroweak vector bosons, be they  $W$ ’s,  $Z$ ’s or photons. These lead to further bounds on the parameter space, essentially pushing  $\Lambda_\varphi$  above a TeV (and hence reducing all radion-mediated effects) and  $M_\Phi$  to values closer to a TeV, though here some avenues for a lighter  $M_\Phi$  remain.

In addition to the current data, we have tried to predict discovery limits at the LHC in two ways. One way is to use the signal strengths, and assume that they will eventually converge within 5% of the SM prediction. This leads to modestly enhanced bounds on the radion-Higgs mixing scenario. The other way is to use the projected discovery limits from the ATLAS and CMS Collaborations for a heavy scalar in Run-2, where we identify that heavy scalar with our heavier eigenstate  $\Phi$ . This, in fact, is very effective for most choices of the mixing parameter  $\xi$  and is sensitive to rather high values of  $M_\Phi$  and  $\Lambda_\varphi$ . The only exception is at the so-called conformal point, which is a peculiar feature of this model, involving a value of the mixing parameter where the heavy scalar essentially decouples from SM fields.

It is interesting to ask how our results would be modified if we replace the simplistic model used above with a more phenomenologically-relevant model where the fields can access the bulk. As

explained in the Introduction, the radion and Higgs fields, being still close to the TeV brane, mix in the same manner [29]. The decay of the radion to the light quarks is severely suppressed because of the small overlap [84] of their wavefunctions in the bulk. Decays of the radion to massive gauge bosons are governed by an additional coupling that can be safely neglected for  $\Lambda_\varphi \gtrsim 1$  TeV. Radions decaying to massless gauge boson pairs (especially to diphotons) is significantly enhanced, however, due to the tree-level coupling in the case of bulk scenario. However, this doesn't really effect our region of interest [81]. We feel, therefore, that the results of this work are robust against more realistic variations of the minimal model and may be safely adopted in such cases.

To conclude, then, we have shown that a mixed radion-Higgs scenario is quite consistent with the current experimental data at the LHC, and there is every possibility that the heavy scalar predicted in this model could be discovered as the LHC continues to run at its present energy of 13 TeV. Discovery of this would certainly be one of the most exciting things to happen in the near future, and, if, the branching ratios turn out to be consistent with this model, could provide a powerful insight into the nature of spacetime itself. Such a happy consummation is to be devoutly hoped for, but, for the present, we must reconcile ourself to a fairly long wait as the Run-2 of the LHC continues.



## CHAPTER 4

---

# Radion Signals at the Conformal Point

---

### 4.1 The Conformal Point

In the last chapter, we have repeatedly commented on a specific feature of the radion-Higgs mixing. For every choice of  $M_\Phi$  and  $\Lambda_\varphi$ , there is a fixed value  $\xi = \xi_0$  which satisfies the equation  $c_\Phi = 0$ , and hence

$$C(\xi) + \gamma A(\xi) = 0 \tag{4.1}$$

and this is known as the ‘conformal’ point<sup>1</sup>. It corresponds to the case when the tree-level couplings  $g_{\Phi X\bar{X}}$  of both the fermions and gauge bosons – generically denoted  $X$  – with the heavy scalar  $\Phi$  vanish. This is a curious situation and corresponds to the case when the mixing is fine-tuned to be such that the parts of the coupling arising from the SM  $h$  and the radion  $\varphi$  cancel each other. Like all fine-tuned situations, if this is the reality, it can hardly be a random effect, and must represent some deeper structure in the theory, which is not addressed in our present formulation. Nevertheless, it is interesting to explore the phenomenological implications of this scenario. In this section, therefore, we investigate the conformal point and see how it can be constrained using current and projected data, just as the other points can. It is important to note that though most of the tree-level couplings of the  $\Phi$  to pairs of SM particles vanish at the conformal point (except for the coupling to  $HH$  pairs), there exist one-loop couplings to pairs of gauge bosons through the trace anomaly. This makes the pattern of branching ratios at the conformal point very different from that in other regions of parameter space. The most important feature of this is the fact that the decays  $\Phi \rightarrow gg$  and  $\Phi \rightarrow \gamma\gamma$  are considerably enhanced with respect to the others – in fact the former is the dominant decay mode. This behaviour is nicely exhibited in Figure 4.1, where we exhibit the behaviour of the relevant branching ratios in the immediate vicinity of the conformal point.

In Figure 4.1, it is immediately apparent that for the particular value  $\xi = \xi_0$ , the tree-level decay modes of  $\Phi \rightarrow X\bar{X}$ , where  $X$  is a massive gauge boson or a fermion, drop sharply by many orders of magnitude. This is particularly true for the cases  $X = t, b$  and  $H$ , with the minimum for the last case occurring at a slightly displaced point from the others (best seen in the zoomed panel on the right). On the other hand, the branching ratios for the purely

---

<sup>1</sup>From this stage we drop the quotes on ‘conformal’.

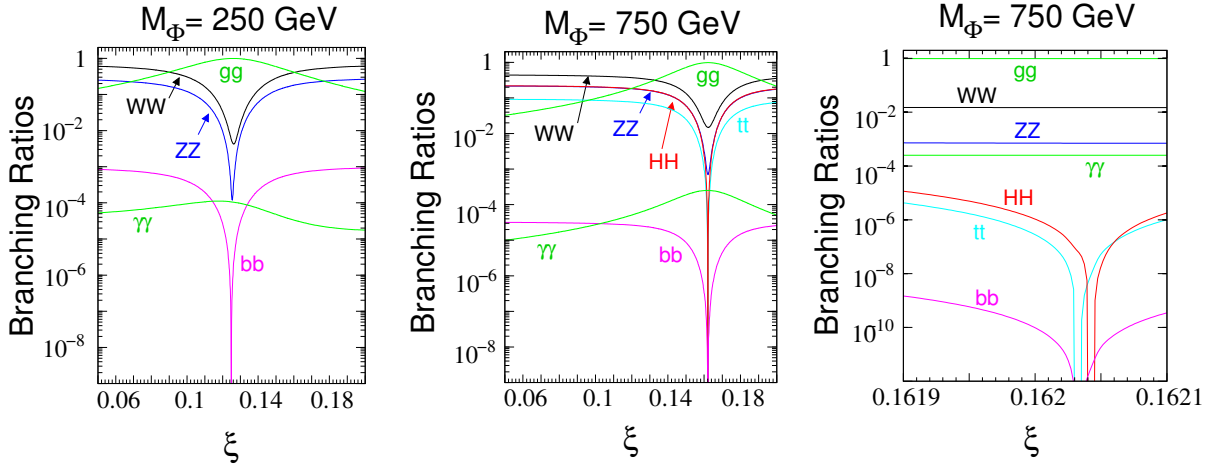


**Figure 4.1:** Branching ratios of the heavy scalar  $\Phi$  in the neighbourhood of the conformal point. Note that the conformal point is quite sensitive to the value of  $M_\Phi$ . There is some minor dependence on the radion vacuum expectation value  $\Lambda_\varphi$ , but for purposes of comparison it has been set at 2 TeV for every plot in this figure. The sharp drop in the tree-level decays at the conformal point may be noted. The conformal point for the decay  $\Phi \rightarrow HH$  is close to, but different from that for other decays, as is clear in the panel on the right, which is a zoomed version of the central panel.

one-loop decays, viz.  $\Phi \rightarrow gg$  and  $\Phi \rightarrow \gamma\gamma$  exhibit a growth at the same point, attributable to their partial decay widths being finite, whereas the others drop almost to zero. However, the decays to  $WW$  and  $ZZ$  states do not disappear altogether because they too have anomaly contributions. Naturally the decay  $\Phi \rightarrow gg$  dominates the others because of the appearance of the strong coupling as well as the colour factor. The decay  $\Phi \rightarrow \gamma\gamma$  also shows a gentle increase, but is intrinsically much more rare than the digluon mode. At the conformal point, therefore, constraints on the model will have to be sought in a different fashion. One obvious way is to consider Higgs boson signal strengths, for if the couplings of the  $\Phi$  vanish that does not mean that the couplings of the  $H$  will also vanish. Accordingly, there will be contributions to the signal strengths and these can be used to constrain the model. In fact, even the heavy scalar searches, i.e.  $pp \rightarrow S \rightarrow VV$ , where  $V = W, Z$  can be used to a limited extent, since the branching ratios  $\Phi \rightarrow VV$ , though small at  $\xi = \xi_0$ , are not absolutely negligible. However – and this is a distinct feature of the conformal point – the strongest bounds come from diphoton searches, which is not entirely surprising, given that this mode is considerably enhanced at the conformal point.

In trying to understand how the conformal point is constrained by the data, we need to recognise that the conformal point  $\xi_0$  is not unique, but a function of  $M_\Phi$  and  $\Lambda_\varphi$ , with the dependence on the former being much stronger than that on the latter. Its variation with  $M_\Phi$  is shown in the left panel of Figure 4.2, where the thickness of the line corresponds to variation of  $\Lambda_\varphi$  from 1 TeV to 20 TeV. This plot shows that the variation flattens out as  $M_\Phi$  grows above 500 GeV, and has a very weak dependence on  $\Lambda_\varphi$ . Nevertheless, we have scanned a sizeable portion of the  $M_\Phi$ – $\Lambda_\varphi$  plane and calculated the values of  $\xi_0$  at every point by solving Eq. (4.1).

With these parameters, we now evaluate the measurables, viz. the signal strengths and the cross-sections for  $pp \rightarrow S \rightarrow VV$ , where  $V = W, Z$ . These are then compared with existing data to yield the constraints on the plane, as shown in the right panel of Figure 4.2. The conventions of this panel are exactly the same as those of Figs. 3.6 and 3.7, but the constraints follow a different pattern. As usual, low values of  $M_\Phi$  and  $\Lambda_\varphi$  are excluded. However, there are

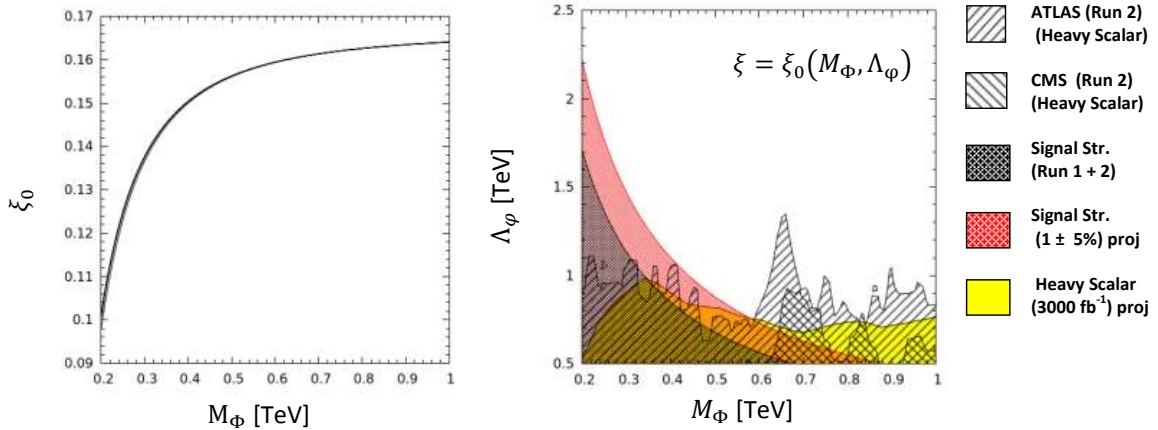


**Figure 4.2:** Constraints on the conformal point  $\xi_0$ . The variation of  $\xi_0$  with  $M_\Phi$  is shown in the left panel. The thickness of the line corresponds to variation of  $\Lambda_\phi$  from 1 to 20 TeV. The right panel shows the  $M_\Phi$ - $\Lambda_\phi$  plane, assuming that at every point the mixing parameter  $\xi = \xi_0$ .

no theoretical constraints, showing that there will always be a conformal point for any choice of model parameters. For small values of  $M_\Phi$ , the strongest constraints come from the signal strengths (dark grey shaded area), while for higher values, it is the ATLAS and CMS data on diphotons – not  $WW$  and  $ZZ$  – from a heavy scalar resonance, which yield the best constraints. Projecting signal strength measurements at the level of  $\mu_{XX} = 1 \pm 0.05$  for all  $X$  provides the red-shaded band, showing that moderate improvement can be obtained if these measurements yield results much closer to the SM prediction. The shaded yellow region represents the predictions from  $ZZ$  decay modes of a heavy scalar for the LHC running at 14 TeV with  $3000 \text{ fb}^{-1}$  [82, 83] of data (which is all that is currently available), and it does worse than the Run-2 data. It may be expected that diphoton searches would provide better discovery limits — when the Run-2 projections become available.

All in all, we can conclude that the conformal point is somewhat less constrained than the rest of the parameter space. It was this narrow window which had been used [85, 86] to explain the purported discovery of a heavy 750 GeV scalar during 2015-2016 [87, 88], though that proto-signal did not survive the test of time [55, 56]. In the next section, we include a discussion of this idea.

## 4.2 Explaining the Erstwhile 750 GeV Resonance

The joint announcement in December 2015, by the ATLAS and CMS Collaborations at the CERN LHC [87, 88], of a modest excess in the  $pp \rightarrow \gamma\gamma$  channel, with a clustering of invariant mass around 750 – 760 GeV, sparked a great deal of speculation in the literature about the possible origins of this excess. The fact that both the ATLAS and the CMS Collaborations observed excess events in precisely the same invariant mass bin was an unusual happenstance and could well have been the harbinger of a momentous discovery, such as the Higgs boson proto-signals in 2011 [89, 90] proved in the next year to be [91, 92]. Therefore, this excess attracted interest to study the possible origins of this ‘signal’, which cannot be explained within the framework of the Standard Model (SM) of strong and electroweak interactions.

The principal features of the CERN observations [87, 88] were as follows.

- A. The ATLAS (CMS) Collaboration had seen a modest ‘bump’ in the invariant mass distribution of  $\gamma\gamma$  final states of 14 (10) events clustered around 750 (760) GeV in 3.2 (2.6)  $\text{fb}^{-1}$  of data at the Run-2 of the LHC at a centre-of-mass energy  $\sqrt{s} = 13$  TeV.
- B. The statistical significance of these results at the ATLAS (CMS) was  $3.9\sigma$  ( $2.6\sigma$ ) when considered for the individual invariant mass bin, but reduced to  $2.3\sigma$  ( $2.0\sigma$ ) when one considered the look-elsewhere effect (a width around 45 GeV).
- C. The width of this proto-resonance appeared to be around 6% of its mass, i.e. around 45 GeV.
- D. The tagging efficiency for the diphoton signal, as estimated by the ATLAS (CMS) Collaborations, was 0.4 (0.6).
- E. No excess over the SM predictions had been observed in other channels, such as dileptons, dijets,  $WW$ ,  $ZZ$ , jets + MET, etc. as searched by both Collaborations in Run-2 of the LHC.

These observations were consistent with the resonant production, in 13 TeV  $pp$  collisions, of a new particle of mass in the range 750 – 760 GeV. This new particle must decay to  $\gamma\gamma$  pairs at a rate large enough to yield the observed signal. At the same time, its possible decays to other channels must be suppressed to the extent of going undetected at the LHC (or elsewhere), at least at the present level of statistics. It was also obvious that such a particle could not belong to the SM, whose particle spectrum was completed by the discovery of the Higgs boson in 2012, and which does not contain any particle with a mass as high as 750 GeV.

Theoretical speculations about the nature of this new particle started from the observation that it must decay into two spin-1 photons, and therefore, must be electrically neutral and have spin 0, or 1, or 2. However, the Landau-Yang theorem [93,94] forbids a massive spin-1 particle from decaying into two massless spin-1 particles (photons), and hence, the resonance had to be either spin-0 or spin-2. The spin-2 option was easily dismissed, for the only known spin-2 particles in elementary particle models are the gravitons, or rather their Kaluza-Klein excitations in models with large or warped extra dimensions [6,8]. Such gravitons would have universal couplings, and one cannot reconcile an observed excess in the diphoton channel with the absence of similar excesses in the dilepton, dijet,  $WW$  and  $ZZ$  channels. There remained the possibility that the resonance was a neutral scalar.

Neutral scalars are ubiquitous in models of physics beyond the SM. Ever since the 1964 discovery by Englert and Brout [95,96], and by Higgs [97,98], that such fields can develop a vacuum expectation value (vev) which breaks a local gauge symmetry spontaneously, the same idea has been invoked in diverse models with extra gauge symmetries at high scales which are made to break spontaneously through the vev’s of postulated extra neutral scalars. These have been used, among other things, to explain parity violation [99,100], achieve grand unification [101–103], solve the strong CP problem [104] and induce inflation in the early Universe [105]. Scalars also play an important role in giving mass to sequential fermions of the SM through their Yukawa interactions [106]. Not surprisingly, therefore, the bulk of theoretical speculations were attempts to fit in the proto-resonance at 750 GeV with one or the other of these postulated scalars<sup>2</sup>.

---

<sup>2</sup>An early study can be found in Ref. [107]

Some of these theoretical studies had already thrown up interesting results. It is clear, for example, that the 750 GeV resonance *could* be

1. one of the heavy scalars  $H^0$  and  $A^0$  postulated in the minimal supersymmetric SM, despite the possibility of varying all the 105 new parameters in the model ([108–111]);
2. any minimal version of the two-Higgs doublet model, i.e. without the addition of new fermion states [108, 109]; however, a more optimistic result was claimed in Refs. [110, 112];
3. a sneutrino  $\tilde{\nu}$  in the  $R$ -parity-violating version of the above, for its branching ratio to two photons is mediated by a one-loop diagram which is suppressed by a factor not larger than  $m_b/750 \text{ GeV} \sim 10^{-5}$ , which renders the production of diphoton signals too low to be observed;
4. a massive dilaton arising in a model with an extra dimension [109]; however, [113] claimed a positive result with this scenario.

On the other hand, it was claimed that the signals in question *could* be explained by

1. an axion field arising in a model with a broken Peccei-Quinn symmetry [114, 115];
2. models with additional vector-like fermions [108, 109, 116–121];
3. a radion in a Randall-Sundrum model where the Higgs boson or the entire SM fields live in the five-dimensional bulk [85, 122];
4. a generic singlet scalar or pseudoscalar [123–126], or specifically, one that may arise in the context of SUSY inspired simplified models [127]
5. a composite scalar coming from strong dynamics [128–133];
6. dark matter models having a scalar mediator [134–136]
7. a pseudo-Goldstone boson or a scalar superpartner to the goldstino [137–141] or to a Dirac bino [142] in a supersymmetric model;
8. a scalar which couples only to photons [143];
9. more imaginative ideas like heavy messenger multiplets, cascade decays, hidden valley theories etc. [144–147].

Some of these works discussed model-independent studies of the signal and eventually focussed on specific models [133, 148, 149]. However, we may note that several of the long list of explanations were clearly devised in haste – not surprisingly under the circumstances – and had not studied the backgrounds very seriously. It was possible, however, to isolate the most serious background to the signal in a very simple-minded construction, which also highlights the difficulty of fitting any of the known models of physics beyond the SM to the observed facts.

In order to be produced in  $pp$  collisions at the LHC, a  $CP$ -even scalar resonance  $\varphi$  must have a coupling (fundamental or effective) to a pair of partons, and in order to decay to diphoton states it must have a coupling (fundamental or effective) to a pair of photons. These are the absolutely minimum requirements to see a diphoton resonance at the LHC. These couplings can be parametrised in a gauge-invariant way as

$$\mathcal{L}_{\text{int}} = y_q \varphi \bar{q}q + \frac{c_g}{M_\varphi} \sum_{a=1}^8 \varphi G_{\mu\nu}^a G^{\mu\nu,a} + \frac{c_\gamma}{M_\varphi} \varphi F_{\mu\nu} F^{\mu\nu} \quad (4.2)$$

Here  $q$  stands for any of the light quarks and could even be summed over all quark flavours, while  $G_{\mu\nu}^a$  and  $F_{\mu\nu}$  denote the field strength tensors for gluons and photons respectively. Before proceeding further, it should be noted that this is a really minimal construction, as it respects the symmetries  $SU(3)_c$  and  $U(1)_{em}$ , which are known to be unbroken, but not the  $SU(2)_L$  of the electroweak theory, which should hold at energy scales above the Higgs vev of 246 GeV. This means that this model assumes an explicit breaking of the  $SU(2)_L \times U(1)_Y$  symmetry of the SM by the  $c_\gamma$  term, which would not be observed at lower energies because of the  $1/M_\varphi$  suppression.

Once we have fixed the above couplings, we can easily calculate the partial decay widths to a  $q\bar{q}$ ,  $gg$  and  $\gamma\gamma$  final state. These turn out to be

$$\Gamma(\varphi \rightarrow q\bar{q}) = \frac{3}{8\pi} y_q^2 M_\varphi, \quad \Gamma(\varphi \rightarrow gg) = \frac{2}{\pi} c_g^2 M_\varphi, \quad \Gamma(\varphi \rightarrow \gamma\gamma) = \frac{1}{4\pi} c_\gamma^2 M_\varphi \quad (4.3)$$

from which it follows that the total decay width of the  $\varphi$  is

$$\Gamma_\varphi = \frac{2M_\varphi}{\pi} \left( c_g^2 + \frac{3}{16} y_q^2 + \frac{1}{8} c_\gamma^2 \right) \quad (4.4)$$

and the branching ratios to diphotons and dijets are

$$\mathcal{B}_{\gamma\gamma} = \frac{\frac{1}{8} c_\gamma^2}{c_g^2 + \frac{3}{16} y_q^2 + \frac{1}{8} c_\gamma^2} \quad \mathcal{B}_{JJ} = \frac{c_g^2 + \frac{3}{16} y_q^2}{c_g^2 + \frac{3}{16} y_q^2 + \frac{1}{8} c_\gamma^2} \quad (4.5)$$

where  $J$  denotes a jet arising from a final state quark or a gluon.

We can calculate the production cross-section for the  $\varphi$  as

$$\sigma_\varphi = \frac{y_q^2}{96\pi s} F_q + \frac{c_g^2}{128\pi s} F_g \quad (4.6)$$

where

$$\begin{aligned} F_q &= \int_{r^2}^1 \frac{dx}{x} \left[ f_{q/p}(x) f_{\bar{q}/p} \left( \frac{r^2}{x} \right) + f_{\bar{q}/p}(x) f_{q/p} \left( \frac{r^2}{x} \right) \right] \\ F_g &= \int_{r^2}^1 \frac{dx}{x} \left[ f_{g/p}(x) f_{g/p} \left( \frac{r^2}{x} \right) \right] \end{aligned} \quad (4.7)$$

with  $r = M_\varphi/\sqrt{s} \simeq 5.77 \times 10^{-2}$  if we take  $M_\varphi \simeq 750$  GeV and  $\sqrt{s} = 13$  TeV. Using CTEQ-6L structure functions, we then find the following values

$$F_u = 2.177 \times 10^2 \quad F_g = 2.914 \times 10^3 \quad (4.8)$$

with other quarks giving smaller results. Not surprisingly, since  $r$  is small, the gluon PDFs dominate all the others.

We are now in a position to put together all the factors and compute the production cross-section for the  $\varphi$  as

$$\sigma_\varphi = 33.36 c_g^2 + 1.66 y_u^2 \quad (4.9)$$

in units of picobarn. Thus, we predict that some tens of thousands of these heavy scalars must have been produced at the LHC Run-2 in order to obtain the signal which has been observed.

It is now a straightforward matter to calculate the cross-sections for diphoton and dijet production at the LHC Run-2. We get

$$\sigma(pp \rightarrow \varphi \rightarrow \gamma\gamma) = \sigma_\varphi \mathcal{B}_{\gamma\gamma} \quad \sigma(pp \rightarrow \varphi \rightarrow JJ) = \sigma_\varphi \mathcal{B}_{JJ} \quad (4.10)$$

where the quantities on the right side can be read off from Eq. (4.5) and Eq. (4.9). For this part of the analysis, we use the leading-order results. QCD corrections will change the numerics somewhat, but will not affect the qualitative features of the analysis.

This simple-minded model must now be subjected to three experimental constraints, viz.,

- A. The total decay width  $\Gamma_\varphi$  as given in Eq. (4.4) should not exceed about 50 GeV. Any larger value would be invalidated by the best fit width [87] of about 45 GeV.
- B. The diphoton cross-section, as given in Eq. (4.10), should lie in the range 5 – 15 fb, which would make it consistent with both the ATLAS and CMS observations.
- C. The dijet cross-section, as given in Eq. (4.10), should not exceed a value around 1.2 pb (at the  $1\sigma$  level) or 2.5 pb (at the  $2\sigma$  level). These constraints arise from the fact that the dijet signals observed at the LHC Run-2 are consistent with the SM prediction of around  $12.5 \pm 1.2$  pb (scaled up from the 8 TeV results [150]), leaving no scope for any excess over the experimental errors.

An analysis of the allowed values of  $c_g$  and  $c_\gamma$ , for different choices of  $y_u$ , is extremely instructive. To illustrate this, we have plotted, in Figure 4.3, the allowed region in the  $c_\gamma$ - $c_g$  plane, for two different values (a)  $y_u = 0$ , and (b)  $y_u = 0.3$  of the Yukawa couplings in Eq. (4.2), setting  $q = u$ .

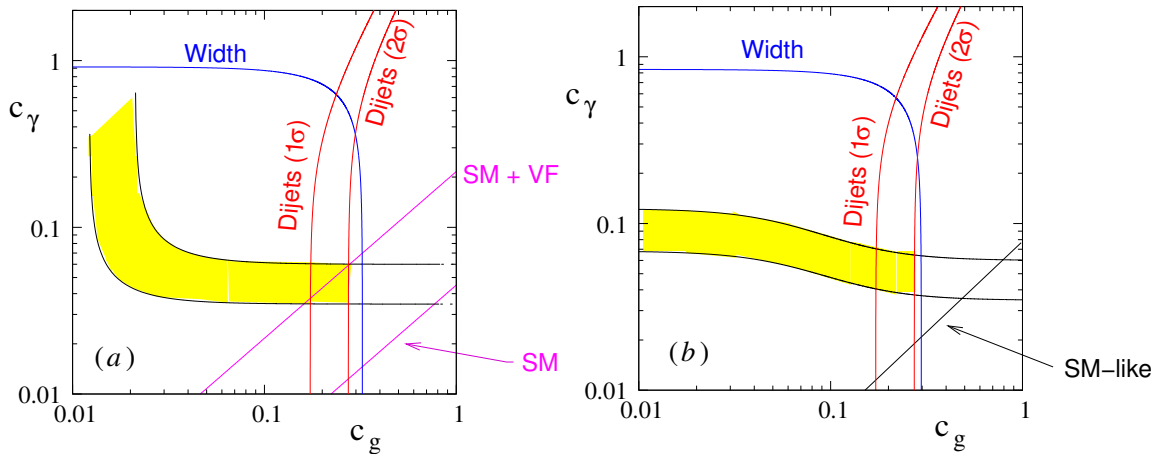


**Figure 4.3:** Illustrating regions in the  $c_\gamma$ - $c_g$  plane which can give rise to the signal in question for (a)  $y_u = 0$ , and (b)  $y_u = 0.3$ . All points above and to the right of the blue line marked ‘Width’ are disallowed by the  $\Gamma_\varphi$  constraint. All points to the right of the red lines marked ‘Dijet’ would lead to unacceptable dijet rates. The yellow shaded region indicates the permitted region which yields the correct diphoton cross-section. The straight (magenta) lines correspond to a radion scenario as described in this work, with a purely SM-like content (marked ‘SM’) and with the SM content augmented by one generation of heavy vectorlike fermions (marked ‘SM + VF’).

A glance at Figure 4.3 shows that only a narrow band of allowed  $c_\gamma$  values can give rise to the observed signal. In the panel marked (a), the graphs curve upward, since  $c_g$  is the only source of production and hence cannot be zero. This is no longer the case in the panel marked (b),

where some production occurs through the nonvanishing Yukawa coupling. The requirement of a scalar width less than about 50 GeV constrains large values of  $c_g$  – as expected – but leaves much of the allowed parameter space unaffected. The dijet constraint is more restrictive at the  $1\sigma$  level, but at 95% confidence level it is no more constraining than the total width.

On the lower right corner of the panel marked (b), we have plotted a straight line in black, which has been marked ‘SM-like’. This corresponds to the case when the scalar has effective couplings to a gluon pair and a photon pair through one loop diagrams with SM particles in the loop. Using the standard computation of the SM partial widths [151] the two parameters will be related by

$$c_\gamma = 0.075 c_g \quad (4.11)$$

which is illustrated by the straight line as shown. The fact that this line is far away from the allowed region only emphasises the difficulty of fitting the observed signal with any of the usual models, as mentioned above. In fact, perhaps the only way in which this line can be shifted towards the allowed region is to include fermions with exotic electromagnetic charges in the loop. In fact, it is not enough to have fermions with charges  $5/3$ , but we also need [108] fermions with charge  $8/3$  and multiple generations of those to boot. Most of the usual models also predict large  $WW$  and  $ZZ$  decay modes of the resonant scalar, which may have avoided detection in the current searches, but are sure to be detected in the next LHC run [152, 153].

It is clear, therefore, that any explanation of the observed diphoton excess requires an extra effort of imagination and perhaps a large degree of fine-tuning as well, inasmuch as the observed scalar does not seem to have the usual decay modes other than the diphoton one. As we have remarked already, it is very difficult to invent a scenario in which we have a scalar which couples only to a pair of partons and a pair of photons, and at the same time, obtain values of  $c_\gamma$  which are large enough compared to  $c_g$  as illustrated in Figure 4.3. However, we wish to point out that there exists one new physics scenario where this is a basic feature of the model, albeit in a fine-tuned situation.

The model which, in our view, provided one of the neatest solutions to the enigma of the 750 GeV resonance, was the variant of the Randall-Sundrum model stabilised by the Goldberger-Wise mechanism, where we have a scalar radion, possibly of electroweak scale mass, which couples to matter through the trace of the energy-momentum tensor. This results in couplings which are very Higgs boson-like, with the SM vev  $v$  replaced by the radion vev  $\Lambda_\varphi$ . However, there exists one major difference, which is that the radion couplings to a  $\gamma\gamma$  or a  $gg$  pair contain contributions from the trace anomaly, which are absent in the case of a Higgs boson.

Of course, if we consider a radion in isolation, its behaviour is so much like a Higgs boson, that it is precluded from being a solution to the 750 GeV resonance problem by the very same arguments that apply to a heavy Higgs boson [108]. However, there exists the very interesting possibility that the radion may *mix* with the Higgs boson of the SM, with the lighter component being the 125 GeV boson observed at CERN in 2012, and the heavier component being the 750 GeV resonance in question, as described in the previous section. We may reiterate that such mixings through kinetic terms [21–23, 38], are controlled by a parameter  $\xi$ . At the conformal point  $\xi = \xi_0 \approx 1/6$ , we have seen that the tree-level couplings of the heavier scalar state to all matter particles vanish, leaving only the one-loop couplings to  $\gamma\gamma$  and  $gg$  pairs, which are

mediated by the trace anomaly. The latter, as shown above, depend on the beta functions of the gauge theory rather than direct couplings of the radion to matter. Apart from the fact that such radions escape all constraints from precision electroweak tests and heavy Higgs boson searches at the LHC, this scenario is highly conducive to an explanation of the diphoton resonance [85]. Thus, we obtain Eq. (4.2) with the specific couplings

$$y_q = 0 \quad \forall q \quad c_g = \frac{\alpha_s}{16\pi} \frac{M_\varphi}{\Lambda_\varphi} g_\varphi(\xi_0) |b_3| \quad c_\gamma = \frac{\alpha}{16\pi} \frac{M_\varphi}{\Lambda_\varphi} g_\varphi(\xi_0) |b_1 + b_2| \quad (4.12)$$

where the  $b_1, b_2, b_3$  correspond to the  $U(1)_Y$ ,  $SU(2)_L$  and  $SU(3)_c$  gauge groups respectively. The function  $g_\varphi(\xi)$  arises from the mixing, but for the choice  $\xi = \xi_0$  is approximately unity.

The beta functions in the above couplings are given, as usual, by

$$b_1 = -\frac{20}{9}N_f - \frac{1}{6}N_s, \quad b_2 = \frac{22}{3} - \frac{4}{3}N_f - \frac{1}{6}N_s, \quad b_3 = 11 - \frac{4}{3}N_f \quad (4.13)$$

where  $N_f$  and  $N_s$  represent the number of fermion and scalar doublets, respectively, in the model. If the particle content on the ‘infrared’ brane matches with that of the SM, we will have  $N_f = 3$  and  $N_s = 1$ , and hence obtain the usual values  $b_1 = -41/6$ ,  $b_2 = 19/6$  and  $b_3 = 7$ . In terms of these, we can write

$$c_\gamma \simeq 0.045c_g \quad (4.14)$$

The corresponding curve is plotted in Figure 4.3, on the panel marked (a), and indicated as ‘SM’. It is clear that this is far away from the allowed region and therefore, this version of the model fails to explain the 750 GeV observation. In fact, this version hardly does better than models where the  $\gamma\gamma$  and  $gg$  couplings are generated from loops containing matter particles (see panel (b) and the discussions following Figure 4.3).

Though the above result is rather disappointing and belies the optimistic claims made just before, a small addition to the model can provide a scenario which works very nicely. This is the addition, on the ‘infrared’ brane, of a single family of vectorlike fermions, which are doublets under  $SU(2)_L$ . The presence of such fermions, so long as their masses lie below that of the resonance, changes  $N_f$  from 3 to 5. As a result, we get  $b_1 = -203/18$ ,  $b_2 = 1/2$  and  $b_3 = 13/3$ , and this leads to

$$c_\gamma \simeq 0.216c_g \quad (4.15)$$

In Figure 4.3(a), this curve is plotted and marked ‘SM + VF’. Obviously, it passes through the allowed region — somewhat marginally if the absence of dijet signals is demanded at  $1\sigma$ , but much more comfortably, if we relax it to  $2\sigma$ . Thus, it seems that we can obtain a solution to the 750 GeV resonance by postulating the following:

- A Randall-Sundrum type scenario, with modulus stabilisation through the Goldberger-Wise mechanism;
- Mixing of the scalar radion with the Higgs boson, with a mixing parameter precisely tuned so that the heavier eigenstate decouples from matter fields on the brane;
- Augmentation of the particle content on the ‘infrared’ brane by one full generation of vectorlike doublet fermions.

An encouraging feature of adding vectorlike fermions is the fact that they are not constrained seriously by electroweak precision tests. However, the story is not completed yet, for we still

have to check that the actual values of  $c_g$  and  $c_\gamma$  are adequate for our purposes, and do not induce new constraints on the model from, for example, the couplings of the light 125 GeV scalar, which does *not* decouple from matter. This is shown in Figure 4.4, where we have plotted the diphoton signal as a function of the radion vev  $\Lambda_\varphi$  – the only free parameter once we set  $\xi = \xi_0$ . For this part of the analysis, QCD corrections to the production cross-section have been included in the form of a factor  $K \approx 2$ . The blue curve marked ‘SM’ shows the cross-section when we consider only SM particles on the brane. Corresponding constraints on the radion vev  $\Lambda_\varphi$  from the signal strengths (in particular,  $\mu_{WW}$  at the CMS [154]) of the 125 GeV scalar are shown as the blue shading. Obviously, this scenario fails to produce enough diphoton events. In any case, it is ruled out by the fact that even with this low level of diphoton production, it would lead to an observable dijet excess (see above).

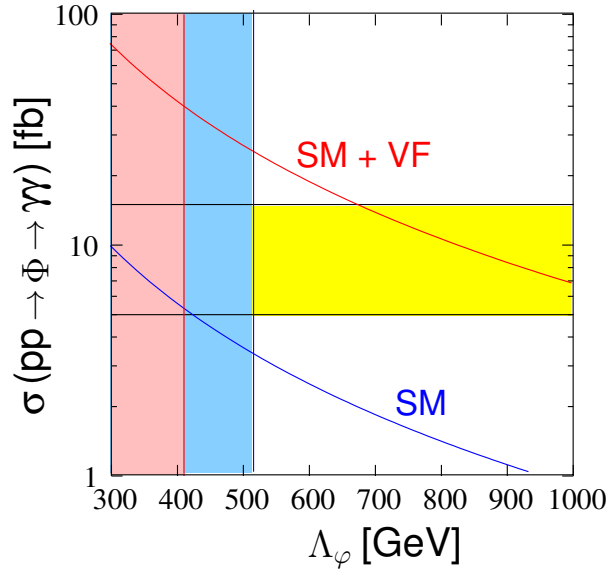


**Figure 4.4:** Cross-sections for diphoton production as a function of the radion vev  $\Lambda_\varphi$ , in the case  $\xi = \xi_0$ , in two different scenarios. The yellow shading indicates the region of interest for the 750 GeV resonance.

The red curve, marked ‘SM + VF’, on the other hand, provides very reasonable cross-sections for values of  $\Lambda_\varphi > 700$  GeV. This corresponds, as explained before, to the SM augmented by a vectorlike family of doublet fermions. Interestingly, this scenario is less constrained by signal strengths than the previous case. The pink shading shows the bounds on  $\Lambda_\varphi$  from the Higgs signal strengths. We have already verified (Figure 4.3) that this model will *not* lead to an observable dijet excess.

To summarise, in this work we considered a simple scenario in which the proto-resonance at 750 GeV was a scalar radion of the Randall-Sundrum model, which has a mixing with the Higgs boson, carefully fine-tuned so that the heavier eigenstate decouples from matter. Identifying this with the possible resonance at 750 GeV, we could explain the observations, including the lack of a dijet signal, provided the SM stands augmented by a single family of vectorlike fermions. As we included just a single family of such fermions, which live purely on the ‘infrared’ brane, and that too, with canonical gauge charges, this appeared to be a more economical solution than many of the ones provided in the literature. Of course, like all the other ingenious explanations for this transient excitement, this work has no relevance to the real world. It has been included mainly as an indicator of the unique features of the conformal point in radion-Higgs mixing.

## CHAPTER 5

---

# Missing $p_T$ Signals for LED at the LHC

---

### 5.1 Introduction

The successful run of the LHC has marked, in many ways, a new era in particle physics. The LHC has now been upgraded from 8 TeV to an increased centre-of-mass energy of 13 TeV and will continue to run for few years to search for new physics. The machine energy is already high enough to potentially search for TeV range physics. With the increased energy, it has already looked for new physics in various channels and found a null result in almost every obvious channel suggested for new physics searches. However, the LHC is expected to run for several more years, and it is entirely possible that new physics may be found when it has collected enough data. It is, therefore, the right time to study newer search channels for the models which predict TeV-range physics.

One such well-known new physics model is the model of Large Extra Dimensions (ADD model) discussed in Chapters 1 and 2 where a number of extra spatial dimensions are introduced. We may recall that in this model the Standard Model fields are confined to a 4D brane, but a massless graviton is free to propagate in the higher-dimensional bulk. On the brane, this appears as a tower of massive KK modes, each a spin-2 field propagating in 4D. Mass of each of these modes is inversely proportional to  $R_c^{(n)}$  where  $n$  is the number of extra dimensions. We also recall that due to the large size of the extra dimensions, the mass spectrum of the KK gravitons becomes a quasi-continuum. The coupling of each KK graviton to matter remains small in this case, but the contribution from a huge number of accessible KK modes make the effect substantial enough to be observed in a TeV range experiment. However, due to the feeble coupling of individual mode, each graviton KK mode does not leave any trace in a detector when it passes through it.

These KK graviton states may appear as (a) emission of real KK gravitons, or (b) as virtual states contributing to the modification of the strength of a process. The behaviour of both types of processes has already been discussed in Chapter 2, and it has been explained how real graviton emission processes can be used as a probe for the model. This forms the theme for the present chapter and the next.

The chapter is organised as follows. First, we consider the simplest process that can be used to

look for this model, viz.  $pp \rightarrow jG_{\vec{n}}$ <sup>1</sup> which has already been studied in the literature [11, 155, 156] and analysed in the experiments to constrain the bulk Planck scale,  $M_D$  [157, 158]. We will then discuss in detail a complementary study to probe the model via the process  $pp \rightarrow t\bar{t}G_{\vec{n}}$ . We will then make a correlated study of these two processes together.

## 5.2 Monojet + MET signals

The simplest process involving real gravitons at a hadron collider is emission of a real KK mode in association with a jet. The contribution for this process comes from the following parton-level subprocesses.

$$gg \longrightarrow gG_{\vec{n}}, \quad qq \longrightarrow gG_{\vec{n}}, \quad \text{and} \quad qg \longrightarrow qG_{\vec{n}}$$

where  $q$  and  $g$  represent quark and gluon partons from the colliding hadrons. The biggest contribution comes from the subprocess  $qg \rightarrow qG_{\vec{n}}$ . The KK graviton, being invisible to the detectors, will contribute to the missing transverse energy (MET). This process will give a signal for **jet + MET** at a hadron collider. The collider signatures for this process has already been studied in Refs. [11, 155, 156]. However, we will discuss this process to some extent for completeness. A representative diagram for this process is shown in Figure 5.1 where a  $G_{\vec{n}}$  is emitted in association with a quark. In addition to the quark final state, final state with a gluon will also contribute to the **jet + MET** final state which will come from the other two subprocesses.

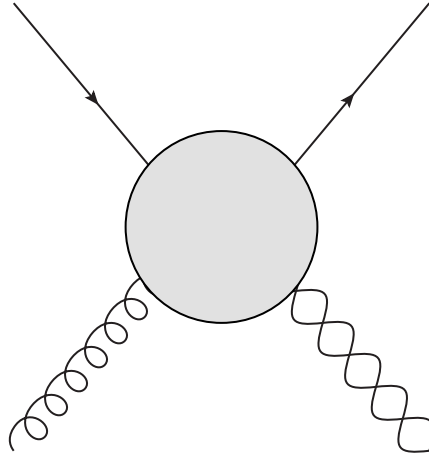


Figure 5.1: A sketch of representative subprocess for the process  $pp \rightarrow jG_{\vec{n}}$ .

As described in Chapter 2, each KK mode  $\vec{n}$  corresponds to different final state. Hence, the calculation of total cross-section involves incoherent sum of all such final states with different KK indices  $\vec{n}$ , i.e.

$$\sigma_{\text{tot}} = \sum_{\{\vec{n}\}} \sigma_{\vec{n}} \quad (5.1)$$

where  $\sigma_{\vec{n}}$  represents the cross-section corresponding to the final state involving KK mode  $G_{\vec{n}}$ . The sum can be approximated by an integral with an appropriate upper cutoff. As argued previously, the cutoff should be the centre-of-mass energy of the collider.

<sup>1</sup>KK gravitons, denoted as  $\tilde{h}_{\mu\nu}^{(\vec{n})}$  in Chapter 2, will be denoted as  $G_{\vec{n}}$  in this chapter.

It may be noted in passing that we are trying to probe a theory with a cutoff scale at  $M_D \sim 5$  TeV which is lower than the centre-of-mass energy  $\simeq 13$  TeV of the currently-running LHC. However, this is not a serious problem since the actual centre-of-mass energy available in an individual partonic event is usually much lower than the machine energy and the number of events where the parton-level collision energy is greater than the cutoff scale is negligibly small. We of course safely probe the cutoff scale of a new theory to a higher value than the machine energy. However, we need to do a systematic study of how low the cutoff scale can be taken for that new theory. A systematic study for the cutoff scale,  $M_D$ , in the case of Large Extra Dimensions from the perturbativity considerations in the **jet** + MET has been done in Ref. [155]. For this process, the conclusion is that  $M_D$  can be taken to be  $\sim 4$  TeV or more for all permissible values of the number of extra dimensions  $n$ .

At the 13 TeV LHC, a search for LED has already been carried out by ATLAS [157] and CMS [158] in the **jet** + MET channel at  $\sim 36$  fb $^{-1}$  luminosity. We list the lower bounds on  $M_D$  obtained by both ATLAS and CMS collaborations in Table 5.1. It may be seen that this gives fairly stringent bounds on the model in question.

$n$	ATLAS [157]	CMS [158]
2	7.7	9.9
3	6.2	7.5
4	5.5	6.3
5	5.1	5.7
6	4.8	5.3

Table 5.1: Lower bound (in TeV) on  $M_D$  for different values of extra dimensions  $n$  from the LHC.

So long as the LHC (and other machines) continue to find no evidence for physics beyond the SM, this process will be enough to constrain the model — that is all that can be done. If, however, deviations from the SM are seen in this channel, then it would be necessary to look for some *confirmatory process* to check if the deviation is, indeed, due to LED. It is with such an optimistic scenario in mind that the following study was undertaken.

### 5.3 MET Signals in Association with $t\bar{t}$

As a confirmatory process for the LED model, we have studied production of KK gravitons in association with  $t\bar{t}$  at the LHC, i.e. the process

$$p p \longrightarrow t \bar{t} G_{\vec{n}}$$

The top quark, whose lifetime is much shorter than the hadronisation timescale, decays promptly to a  $b$  quark and a  $W$  boson with almost 100% branching ratio. The  $W$  boson then decays, also promptly, either to a lepton-neutrino pair or to a quark-antiquark pair, while  $b$  quarks will hadronise to jets with a large probability of displaced vertices due to the long lifetime of the  $b$  quark. The other light quarks coming from  $W$  bosons will hadronise to prompt jets. Neutrinos

and graviton KK states will provide missing transverse energy (MET). Depending on the decay channels of the two  $W$  bosons, then, we can predict three possible final states, viz.

1.  $\ell^+\ell^- + \text{jets} + \text{MET}$ ,
2.  $\ell^\pm + \text{jets} + \text{MET}$ ,
3.  $\text{jets} + \text{MET}$

where  $\ell^\pm$  can be an electron ( $e$ ), a muon ( $\mu$ ) or a tau ( $\tau$ ) lepton. The  $b$ -quark jets can be tagged, with an efficiency which can be as high as 70%, and the  $t$ -quarks, if the initial  $t$  energy is high enough, would lead to a fat jet which can be tagged as a  $t$ -jet reasonably efficiently (40 – 50%) using jet substructure-based methods [159].

The main SM backgrounds for the above final states will come from the events with  $t\bar{t}$  and  $t\bar{t}Z(\nu\bar{\nu})$  final states when, in the latter case,  $Z$  decays invisibly to a pair of neutrinos. Sketches

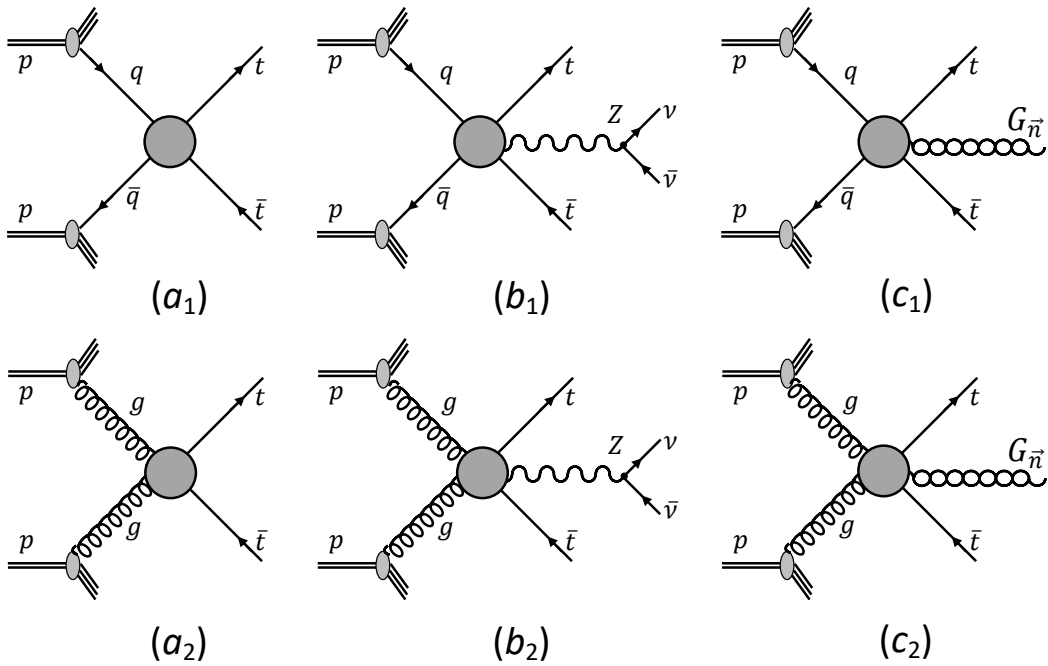


Figure 5.2: Figure shows diagrams of the signal and background processes at the LHC.

of the signal and background processes are shown in Figure 5.2. The top panel consisting of three diagrams ( $a_1$ ), ( $b_1$ ) and ( $c_1$ ) represents quark-initiated processes while the bottom ones ( $a_2$ ), ( $b_2$ ) and ( $c_2$ ) are for gluon-initiated processes. If we divide the figure vertically then the right most panel consisting of diagrams ( $c_1$ ) and ( $c_2$ ) represents the sketches for  $t\bar{t}G_{\vec{n}}$  signal. The left most panel containing diagrams ( $a_1$ ) and ( $a_2$ ) are for  $t\bar{t}$  background and the central panel containing ( $b_1$ ) and ( $b_2$ ) diagrams are for  $t\bar{t}Z$  background processes. The amplitudes for these processes are given in Appendix A. Computation of the signal cross-section is analytically and numerically challenging, as it involves 7 quark-initiated and 21 gluon-initiated Feynman

diagrams. Similarly, computation of the  $t\bar{t}Z$  background involves 12 diagrams. As the cross-section formulae are very long, they had to be calculated piecemeal to prevent fatal roundoff errors in the numerical analysis. The final results were then subjected to stringent tests to ensure that they were, indeed, free from such errors. The calculation is slightly more difficult than a typical cross-section calculation since we need to sum over all the KK graviton processes by approximating the sum as an integration with a proper density-of-states as described in Chapter 2.

The decays of the top quarks of the  $t\bar{t}$  and  $t\bar{t}Z$  background then lead to exactly the same three kinds of final states as listed above. However, the cross-section, particularly for the  $t\bar{t}$  is orders of magnitude larger than the signal cross-section, suppressed as it is by values of  $M_D$  larger than 4 TeV. We have, therefore, made a kinematic cut-based analysis optimised to enhance the signal with respect to the backgrounds.

The cuts are based on the following kinematic considerations. In the SM top-pair production process, where no third particle is present in the final state, the  $\vec{p}_T$  of top and anti-top will be the same but opposite in direction. Produced leptons after decay of a top and then further decay of a  $W^+$  will also be highly boosted, and hence, will emerge in almost the same direction as the original top. However, if a third particle is produced with the  $t\bar{t}$  pair, in most cases the  $p_T$ -balance will be lost and this will be reflected as a significant deviation from the SM  $\not{p}_T$  distribution of top-pair production in any channel. For the  $t\bar{t}$  background to dilepton events,  $\not{p}_T$  will almost be nil as the two neutrinos will emerge practically back-to-back in the transverse plane. In the purely hadronic case, we expect almost no missing  $p_T$  from the  $t\bar{t}$  background. The invisible gravitons will, therefore, in every case, enhance the missing  $p_T$ . The  $t\bar{t}Z$  background, however, will be, at some level, irreducible, because a massive  $Z$  boson, decaying invisibly, is not so different from a massive KK graviton mode, also invisible. However, the mass of the  $Z$  is fixed whereas there is a continuous spectrum of graviton masses, ranging from the near massless to a few TeV. This makes for *some* kinematic differences, which we have exploited through kinematic cuts. In each of the three types of final states, the best set of cuts were found by considering  $10^3$  sets of random cuts and optimising for the signal significance and the number of signal events. This has been done in the following way. A set of kinematic cuts was first chosen which matches closely with experimental top quark searches at hadron colliders and was possible to implement in a parton-level study. Maximum ranges of these cuts were assigned, using the acceptance criteria, and then a random values of these cuts was generated using a simple pseudorandom number generator. These kinematic cuts were applied to the final states and signal significance  $S/\sqrt{B}$ , where  $S$  is number of signal event and  $B$  is number of background events with a given luminosity, was calculated. The procedure was repeated 1000 times, and the optimal set of cuts was chosen as the set that yielded at least 10 events for  $3 \text{ ab}^{-1}$  luminosity and gave the best signal significance. As the actual numbers came out to be fractional, they were rounded off to the nearest plausible value.

Before going into the details of the results we have obtained, we may note the tools and procedures adopted for the study. We used the Feynman Rules given in the appendix of Ref. [11] to calculate the diagrams in the ADD Model and standard SM Feynman Rules consistent with Ref. [11] for calculating the SM background processes. For the trace calculations we used the

public domain tool `Form` [160]. The cross-section calculation and differential distribution of the event variables were obtained by an author-developed Monte-Carlo integrator built around the CERN library package `SAMPLE`, which uses an importance sampling algorithm. In each case, in the integrator, depending upon the convergence rate,  $10^6$  to  $10^7$  sample points were taken to calculate cross-sections and to generate differential distributions by numerical integration. The estimates for SM backgrounds were also obtained by the same integrator in order to be consistent with the estimates for signal. With such numbers, we felt confident that tails of the kinematic distributions were well estimated.

For all the cross-section calculation in this chapter we used the `CTEQ6M` [161] PDF sets, which uses standard MSbar scheme to calculate PDF values at Next to Leading Order (NLO), with the factorization scale set at the centre-of-mass ( $\sqrt{\hat{s}}$ ) of the parton-level hard scattering process. For the SM background estimates, we estimated NLO QCD effects by a short cut, i.e. we multiplied the LO cross-section by a  $\sqrt{\hat{s}}$ -dependent scale factor ( $K$ -factor), calculated using Ref. [162] for parton-level heavy quark production process at NLO. For the parton-level hard processes, the value of  $\alpha_S$  was also taken to be the usual  $\sqrt{\hat{s}}$ -dependent running value with five flavours and  $\alpha_S(M_Z) = 0.118$  [10].

### 5.3.1 Dilepton final states

At the LHC, the cleanest of these three channels is the final state with 2 leptons, viz.  $\ell^+\ell^- + \mathbf{jets} + \text{MET}$  final state, since the efficiency for detecting leptons is almost 100%. The efficiency of tau-lepton tagging is slightly less  $\sim 80\%$ . In the analysis, we, therefore, assume the efficiency of detecting electron and muon to be 100% while the efficiency for tau to be 80%. The  $b$ -tagging efficiency was taken to be 70%. With these assumptions, we carried out a kinematic cut-based analysis on the parton level events.

In Table 5.2, we show the principal cuts and their effects on the signal as well as background. The different sets of cuts in Table 5.2 may be characterised as follows. Set A is essentially the minimal set of cuts, mostly dictated by fiducial considerations. Set B contains the selection cuts – except for the cut on  $\cancel{p}_T$  – which optimise the signal-to-background ratio. The ‘Final’ set then adds a lower cut on missing  $p_T$ . The LHC being a hadron collider, the QCD background is also very large, but it can be reduced greatly with lower cuts on the  $p_T$  of the final states.

The cross-sections in the third, fourth and fifth columns of Table 5.2 tell their own story. The enormous  $t\bar{t}$  backgrounds are removed almost completely by the cuts, and the  $t\bar{t}Z$  background is reduced around 120 times, at a cost to the signal of a reduction to about 20%. To further illustrate the effect of these cuts, we have plotted the distribution of  $\cancel{p}_T$  in events with  $\ell^+\ell^- + \mathbf{jets} + \text{MET}$  final states in the left panel of Figure 5.3 for  $n = 6$  in the ADD model with  $M_D = 4.8$  TeV, which represents the current lower bound on  $M_D$  from the LHC data at  $\sqrt{s} = 13$  TeV machine energy by the ATLAS Collaboration [157] as listed in Table 5.1. For this plot, the integrated luminosity has been taken to be  $3000 \text{ fb}^{-1}$ . For number of extra dimensions less than 6, distribution patterns will be similar but cross-sections are different.

In Figure 5.3, the black histograms correspond to the  $t\bar{t}$  background process. It is immediately clear that for the  $t\bar{t}Z(\nu\bar{\nu})$  and  $t\bar{t}G_{\bar{n}}$  processes, shown as blue and red histograms respectively,

Set	Cuts	$\sigma_{t\bar{t}}$ [fb]	$\sigma_{t\bar{t}Z}$ [fb]	$\sum_n \sigma_{t\bar{t}G_n}$ [fb]
A	$\eta_\ell < 3, \eta_j < 3$ $\Delta R_{\ell j} > 0.4, \Delta R_{\ell_1 \ell_2} > 0.2, \Delta R_{j_1 j_2} > 0.7$ $p_{T\ell} > 20$ GeV, $p_{Tj} > 20$ GeV, $\cancel{p}_T > 20$ GeV	17590.2	5.1997	0.0716
B	Set A + $\eta_\ell < 2.2, \eta_j < 2.5$ $p_{T\ell_1} > 80$ GeV, $p_{T\ell_2} > 30$ GeV $p_{Tj_1} > 35$ GeV, $p_{Tj_2} > 25$ GeV $\Delta R_{j_1 j_2} < 3.0, \Delta R_{\ell_1 \ell_2} < 2.2$	940.41	0.4151	0.0237
Final	Set B + $\cancel{p}_T > 360$ GeV	0.0028	0.0444	0.0145

**Table 5.2:** List of sets of cuts for  $\ell^+\ell^- + \text{jets} + \text{MET}$  signal and their effects on the cross-sections at  $\sqrt{s} = 13$  TeV. The signal is computed for  $n = 6$  and  $M_D = 4.8$  TeV.

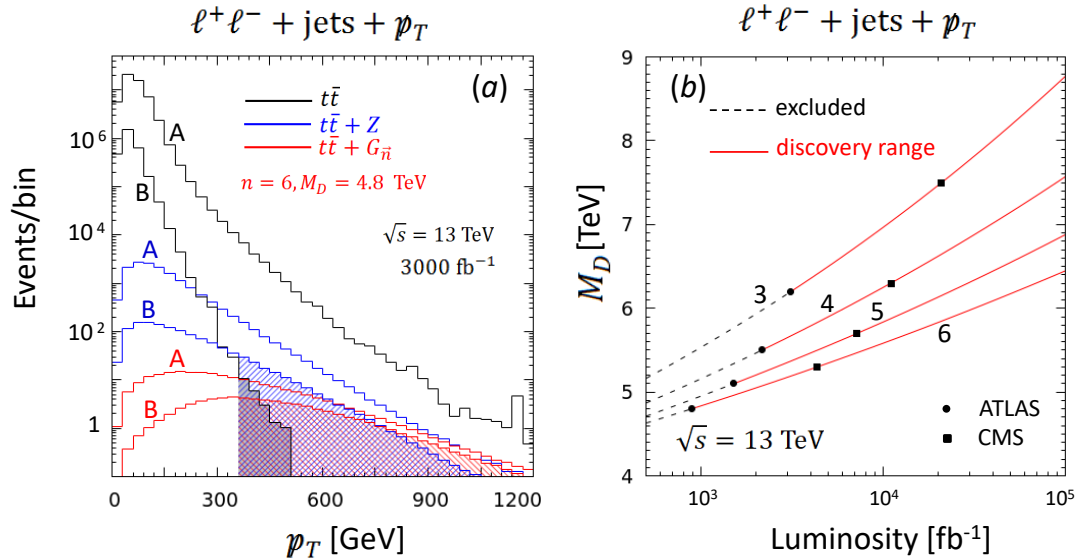


**Figure 5.3:** Analysis of the  $\ell^+\ell^- + \text{jets} + \text{MET}$  vis-à-vis background at the LHC. The left panel (a) shows the  $\cancel{p}_T$  distribution of signal vs.  $t\bar{t}$  and  $t\bar{t}Z$  backgrounds, represented by red, black and blue histograms respectively. The cuts sets indicated in Table 5.2 are marked alongside the relevant histograms in the same colour. The hatched regions indicate the final set of cuts. The right panel (b) shows the 95% discovery plot (red lines) as a function of integrated luminosity, where the numbers of extra dimensions are indicated next to the curves. The dashed parts are already excluded by the LHC [157].

the  $\cancel{p}_T$  distributions are shifted toward the right, indicative of increased missing  $p_T$ . Our results corresponding to sets ‘A’ and ‘B’ are marked alongside the corresponding histograms. The Final Set, which has a lower cut on  $\cancel{p}_T$ , has not been labelled in the plot but is represented by the hatched regions with the same colour scheme as used for the histogram plots.

The right panel of Figure 5.3 shows discovery limits at 95% C.L. of the above-mentioned signal for the ADD model in the plane of  $M_D$  versus the machine luminosity. Each curve corresponds to a signal significance of 95% C.L. for different numbers of extra dimensions indicated by the numbers marked next to the lines. The dashed lines terminating at black circular dots indicate ranges of  $M_D$  already excluded by ATLAS [157] at the LHC. The black square dots on the lines indicate the current LHC bounds on  $M_D$  by CMS [158]. The corresponding abscissa indicates

the integrated luminosity required to obtain a 95% C.L. signal at the LHC. As it can be seen in the figure, for  $n = 5, 6$ , a luminosity of  $\approx 1000 \text{ fb}^{-1}$  is needed in order to reach the current lower bound on  $M_D$  given by ATLAS. For  $n = 3, 4$ , the luminosity requirement is slightly more  $\approx 3000 \text{ fb}^{-1}$ .

### 5.3.2 Single lepton final states

Though dilepton signal is the cleanest channel, the advantage is weakened by the smallness of branching ratio of leptonic decays of  $W$  compared to its hadronic branching fraction. This increase in branching ratio increases the signal significance more effectively. In fact, as we will see that  $\ell^\pm + \text{jets} + \text{MET}$  signal gives us the best sensitivity among all the three signals. Here again we carried out a kinematic cut-based analysis similar to the case of dilepton final state. The sets of cuts are listed in Table 5.3. In this case, the huge  $t\bar{t}$  background is completely removed by the choice of cuts. In addition to the  $t\bar{t}$  and  $t\bar{t}Z$  background,  $t\bar{b}$  production, with top

Set	Cuts	$\sigma_{t\bar{t}}$ [fb]	$\sigma_{t\bar{b}}$ [fb]	$\sigma_{t\bar{t}Z}$ [fb]	$\sum_n \sigma_{t\bar{t}G_n}$ [fb]
A	$\eta_\ell < 3, \eta_j < 3$ $\Delta R_{\ell j} > 0.4, \Delta R_{j_1 j_2} > 0.7$ $p_{T\ell} > 20 \text{ GeV}, p_{Tj} > 20 \text{ GeV},$ $\cancel{p}_T > 20 \text{ GeV}$	104,805.3	440.59	33.4049	0.4949
B	Set A + $p_{T\ell} > 40, \eta_\ell < 2.5, \eta_j < 2.5$ $0.4 < \Delta R_{\ell j} < 2.2, 0.7 < \Delta R_{j_1 j_2} < 2.7$	565.09	3.4336	1.0985	0.1558
Final	Set B + $\cancel{p}_T > 480 \text{ GeV}$	0.0	0.0	0.1535	0.0980

**Table 5.3:** List of sets of cuts for  $\ell^\pm + \text{jets} + \text{MET}$  signal and their effects on the cross-sections at  $\sqrt{s} = 13 \text{ TeV}$ . The signal is computed for  $n = 6$  and  $M_D = 4.8 \text{ TeV}$ .

decaying leptonically, gives a non-negligible contribution to the background for  $\ell^\pm + \text{jets} + \text{MET}$  signal<sup>2</sup>. However, like the  $t\bar{t}$  background,  $t\bar{b}$  can also be removed completely with a proper choice of cuts. This is clearly evident from the last entry in the column of Table 5.3 marked as  $\sigma_{t\bar{b}}$ . Only irreducible background is that is coming from  $t\bar{t}Z$ .

Like the previous case, the effect of the cuts has been shown graphically in the left panel of Figure 5.4 using notations and conventions similar to that of Figure 5.3. The new addition in Figure 5.4(a) is the green histogram representing the  $t\bar{b}$  background which goes to zero after imposing the Final set of cuts. As the cross-sections for  $t\bar{t}$  and  $t\bar{b}$  backgrounds are effectively zero after the final cut, the black and the green hatched regions are absent. In Figure 5.4(b), the discovery limit at 95% C.L. is plotted following the convention set in Figure 5.3(b). We see that the luminosity requirement in this case is almost a tenth with respect to that in the case of dilepton signal.

<sup>2</sup>Here  $t\bar{b}$  represents all the single top production signals, viz.  $tb, t\bar{b}, \bar{t}b$  and  $\bar{t}\bar{b}$ , but contribution for  $t\bar{b}$  is the largest.

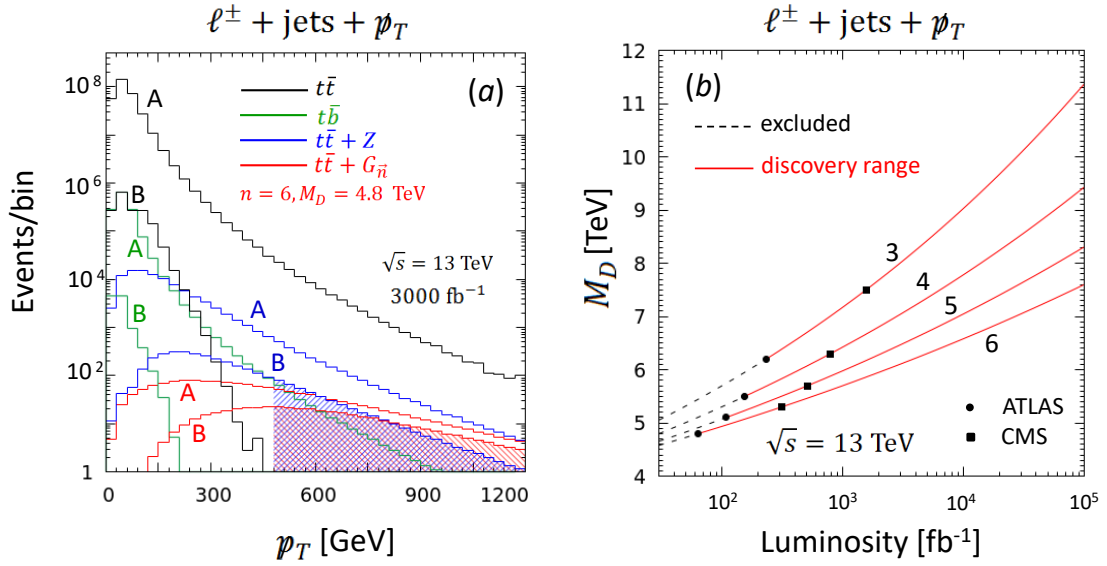


**Figure 5.4:** Analysis of the  $\ell^\pm + \text{jets} + \text{MET}$  signal vis-à-vis background at the LHC. The left panel (a) shows the  $p_T$  distribution of signal vs.  $t\bar{t}$ ,  $t\bar{t}b$  and  $t\bar{t}Z$  backgrounds and the right panel (b) shows the 95% discovery plot as a function of integrated luminosity. The notations and conventions are exactly as in Figure 5.3.

### 5.3.3 Hadronic final states

Since the hadronic branching ratio for a  $W$  is bigger than its leptonic branching ratio, we made similar kinematic cut-based analysis in the hadronic channel. Energy of the collider being high enough, the LHC can produce energetic top quarks, if decay hadronically, can be tagged quite effectively with  $\sim (40 - 50)\%$  efficiency by boosted top technique [159]. However, the cross-section for the signal as well as for the backgrounds will be small. This can be seen from the last three columns of Table 5.4 where the cut sets are also listed in the second column. The notations and conventions for the cut sets are very similar to Table 5.2. In this case, we demand at least 2 jets in the process, one of which has to be tagged as a top quark. This helps to reduce the QCD background, at the cost of a top quark efficiency factor which is 40% or less.

Set	Cuts	$\sigma_{t\bar{t}}$ [fb]	$\sigma_{t\bar{t}Z}$ [fb]	$\sum_n \sigma_{t\bar{t}G_n}$ [fb]
A	$N_j \geq 2, \eta_j < 3, p_{Tj} > 20 \text{ GeV}, \cancel{p}_T > 20 \text{ GeV}$	0.0669	0.9342	0.0795
B	Set A + $20 \text{ GeV} < p_{Tj_2} < 220 \text{ GeV}, \eta_j < 2.7,$ $\Delta R_{j_1j_2} < 2.7$	0.0012	0.1954	0.0460
Final	Set B + $\cancel{p}_T > 660 \text{ GeV}$	0.0000	0.0738	0.0317

**Table 5.4:** List of sets of cuts for  $\text{jets} + \text{MET}$  signal and their effects on the cross-sections at  $\sqrt{s} = 13$  TeV. The signal is computed for  $n = 6$  and  $M_D = 4.8$  TeV.

In this case, we can see that  $t\bar{t}$  background has much smaller cross-section compared to  $t\bar{t}Z$  background. It may be noted that the zero value in the table is not strictly zero, but indicates that it is smaller than the number of decimal places shown. This smallness in cross-section in  $t\bar{t}$  background is because cross-section of high missing- $p_T$  in  $t\bar{t}$  event is very small. The reason is there is no hard source of  $\cancel{p}_T$  in a fully hadronic event, unlike the case of  $t\bar{t}Z$  background, where  $Z$  decaying to neutrinos is invisible. In fact, the only source of missing  $p_T$  in an actual event

mainly comes from the detector effect, i.e. when a final state hadron is not detected by the detectors due to its small momentum or due to its production in forward or backward direction which is outside the detector coverage. As we have not done a detector simulation, we do not have an exact estimate for this, but it is unlikely that these effects can produce  $\cancel{p}_T$  greater than a few GeV at most. That is why selection cut with  $\cancel{p}_T > 20$  GeV gives very small number of events and this result is quite robust. When we include the top-quark tagging efficiency, the background is further diminished, but, of course, the signal is also similarly affected, and that is why we tag only one top quark instead of both the top quarks.

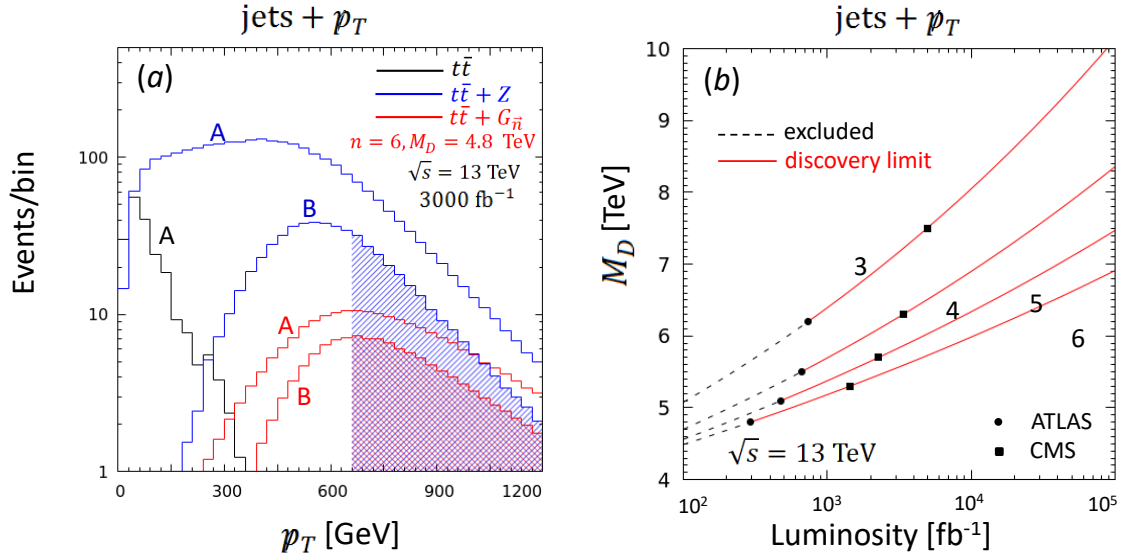


**Figure 5.5:** Analysis of the jets+MET signal vis-à-vis background at the LHC. The left panel (a) shows the  $\cancel{p}_T$  distribution of signal vs.  $t\bar{t}$ ,  $t\bar{t}Z$  backgrounds and the right panel (b) shows the 95% discovery plot as a function of integrated luminosity. The notations and conventions are exactly as in Figure 5.3.

Figure 5.5(a) shows the distribution of the signal and background events. The number of events are very small since we demanded one top to be tagged. The  $t\bar{t}$  background is removed to almost zero even in the set 'B'. Figure 5.5(b) shows 95% C.L. discovery limit with this signal. This signal does better than the dilepton signal but slightly worse than the monolepton signal. With better top tagging efficiency, the signal sensitivity can be improved further.

Before going to the next section, it is worth mentioning one important aspect of the projected limits on  $M_D$  presented in this chapter of the thesis. This is that the bounds on  $M_D$  can be as low as 4.5 TeV, whereas the beam energies at the LHC are as high as 6.5 TeV. In the usual ADD formalism, the sum over Kaluza-Klein modes diverges as  $\sqrt{s} \rightarrow M_D$  and above the scale  $M_D$  we may expect new physics in which strong gravity (with perhaps stringy states) plays an important role. Thus, if there are events which have a partonic centre-of-mass energy above  $M_D$ , we do not know how to calculate the cross-section, and this, at first glance, would seem to make our results invalid. On deeper reflection, however, it may be seen that these effects, if any, must be very small and hence, our results are reasonably robust. The reasons for this are as follows.

If  $M_D$  is taken to be the higher-dimensional Planck scale, it enters the cross-section from two sources. One is from the density of states, where it is used to replace the radius of curvature

$R_c$  of the compact dimensions. The other is as a cutoff for the sum over KK states, which appears when we sum over graviton states. The cutoff in the latter may actually be somewhat smaller than  $M_D$ , and hence, the value of  $M_D$  used in our computations is not quite the higher-dimensional Planck scale. This is a level of inaccuracy which we share with all the existing literature, including the experimental bounds. It may be noted, however, that as  $M_D$  appears as the fourth power, and factor in the cross-section will change it only by the fourth root, and this may not be very significant.

Of more importance is the fact that when we consider energies as high as 4.5 TeV at the LHC, the PDF factors, especially for gluon-induced processes, become very small, and hence, the probability of having events with energy greater than  $M_D = 4.5$  TeV is quite negligible. We do not expect the parton-level cross-sections in the unknown theory above  $M_D$  to have enormous values since the full theory is supposed to maintain unitarity. Therefore, multiplication by the very small PDF factors leads to negligible cross-section. The only exception to this would be if we have *resonant* states at or around  $M_D$ , such as, for example, stringy states of the full theory (if it is a string theory). However, such high-mass resonant states would most probably have been already discovered at the LHC, and in any case, they would certainly affect the LED discovery process with a monojet and missing energy. We may, then, safely assume, for the present, that such resonant states are absent at or around  $M_D$ . If, at a later stage, some weak resonant states are indeed discovered, this work may have to be suitably modified.

It may be mentioned in passing that in the experimental papers by ATLAS [157] and CMS [158], a factor of  $M_D^4/\hat{s}^2$  is multiplied in the simulated events whenever  $\sqrt{\hat{s}} > M_D$  to suppress any extra contributions. Moreover, in Ref [157], it is shown that the bounds obtained are independent of this dampening condition for Monojet +  $\cancel{p}_T$  signal in the same model. However, this dampening condition is completely ad hoc, and hence we did not implement any dampening condition in any of our analyses. We did, however, check that if we had implemented it, our results would have changed only very slightly.

## 5.4 Correlation between monojet + MET and $t\bar{t}$ + MET

It has already been stated that the process  $pp \rightarrow gG_{\vec{n}}$ , leading to a signal with a monojet and large  $\cancel{p}_T$  is the leading process at the LHC and is the source of the dots indicating ATLAS and CMS constraints [157, 158] in Figures 5.3(b), 5.4(b) and 5.5(b) with an integrated luminosity around  $35 \text{ fb}^{-1}$ , which is far more efficient than the process considered here which requires at  $100 \text{ fb}^{-1}$  or more to reach the same bounds. However, the usefulness of this process will become apparent when we consider a *correlation* between the two processes, viz. **monojet + MET** and  $\ell^\pm + \text{jets} + \text{MET}$  which gives the best discovery limit at 95% C.L. Figure 5.6 shows just such a correlation plot between **monojet +  $\cancel{p}_T$**  vs.  $\ell^\pm + \text{jets} + \cancel{p}_T$  event numbers at 13 TeV with  $3 \text{ ab}^{-1}$  luminosity. The lines in the plot are generated by varying the string scale  $M_D$ , increasing towards the bottom left corner. The colour convention of the lines are similar to that of the plot in the right panel of Figure 5.3. The grey shaded region is the 95% C.L. fluctuation of SM background. This immediately tells that  $M_D$  corresponding to the lines inside the shaded region will not be probed upto 95% C.L. by either of the processes. There are, however, substantial parts of the correlation lines which are outside the shaded box, and hence *can* be probed by

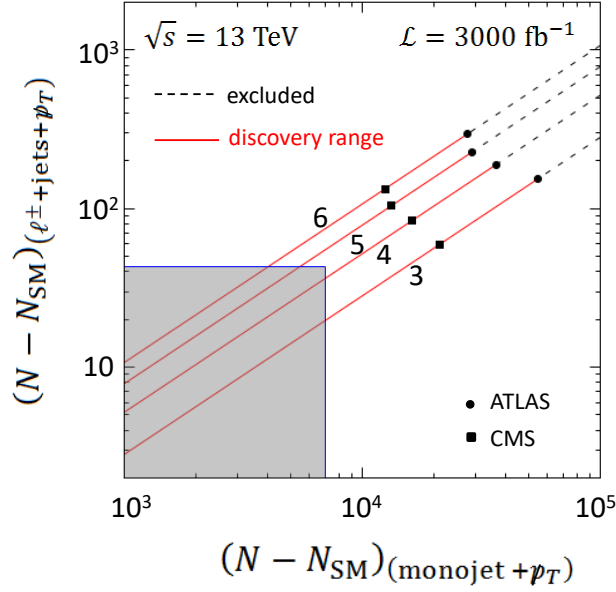


**Figure 5.6:** Correlation plot showing events numbers for  $\text{monojet} + p_T$  vs.  $\ell^\pm + \text{jets} + p_T$  events at 13 TeV with  $3 \text{ ab}^{-1}$  luminosity. The lines varying string scale  $M_D$ , increasing in a south-west direction. The colour convention of the lines are similar to Figure 5.3(b). The shaded region represents the 95% C.L. fluctuation of the SM background.

the 13 TeV LHC at  $3 \text{ ab}^{-1}$  luminosity. What is interesting about this plot, however, is that if the observed numbers of events do fall outside the grey-shaded region, one can at once tell if the cause of this deviation is due to LED or some other model, and if it is LED, the number of extra dimensions can simply be read off from the curve to which the experimental point is in closest proximity.

## 5.5 Summary and Outlook

The ADD model of Large Extra Dimensions provides one of the most elegant solution to the Hierarchy problem in the SM. The bulk graviton in this model is seen as a collection of KK gravitons in the 4-dimensional brane where SM fields are confined. These KK states can be produced as final state particles in processes at the currently running hadron collider, the LHC, with observable strength. Two such graviton emission processes have been studied in this work, with the monojet process being already available in the literature and the study of  $t\bar{t}$  states constituting a new study.

Expecting that the LHC will continue to run for few more years and will collect sizeable data to probe for new physics, we have studied real graviton emission process in association with the production of a pair of top quarks. This graviton emission process with top quark pair, gives rise to 3 types of final states, namely  $\ell^+\ell^- + \text{jets} + \text{MET}$ ,  $\ell^\pm + \text{jets} + \text{MET}$  and  $\text{jets} + \text{MET}$ . The final state with single lepton gives the best signal for this process since it has advantages from cleaner signal from leptonic final state and higher branching fraction from the hadronic side. Purely hadronic final state with a top being tagged is also useful since the background can be reduced greatly in this case.

At a hadron collider, the best signal for ADD model is `monojet+MET` signal. This process already puts fairly stringent bounds on the bulk Planck scale  $M_D$  from LHC data. However, a correlation between the `monojet+MET` signal and the `t $\bar{t}$ +MET`, studied in this work, will help to probe the ADD model at the LHC. Though the bounds from `monojet+MET` is the best signal to look for at the LHC, one may search for `t $\bar{t}$ +MET` process as a confirmatory process. Moreover, if the errors are small enough, we can read the number of extra dimensions  $n$  off from a single correlation plot, something which cannot be done by considering a single process.

It is natural to ask about the prospects of the process at higher energy hadron collider such as VLHC which will be running at 27 TeV or 100 TeV. It is difficult to answer this question offhand for a very high energy hadron machine because the analysis strategy is likely to be quite different at a very high energy machine due to the enormous boost all Standard Model particles will have. A future study of this is certainly to be desired.

Another important issue at a very high energy machine is that the machine energy could lie far above the string scale  $M_D$  of a few TeV which we have considered in the study. At such energies, gravity would be strong and the underlying physics could be quite different, unless, of course,  $M_D$  is even higher — but that would lead to a *little hierarchy problem* in the Higgs boson mass, removing the strongest motivation for LED.

The other kind of proposed future colliders are  $e^+e^-$  colliders. We will focus on a similar process at the future  $e^+e^-$  colliders in the next chapter.



## CHAPTER 6

---

# Missing $p_T$ Signals for LED at $e^+e^-$ Colliders

---

### 6.1 Introduction

The discovery of the Higgs boson at the LHC, and the lack of further signal for new particles and interactions has provided strong motivation for precision measurement of the parameters of the Standard Model. Precision measurement at a hadron collider, like the LHC, is not efficient due to the uncertainties arising from strong interactions. It is, therefore, natural to look for other types of colliders where precision measurement will be more effective. It has long been known that linear colliders with colliding electrons and positrons are more useful for precision measurements. Thus, the Linear Collider Collaboration (LCC) has proposed the construction of two linear colliders. One is the International Linear Collider (ILC) which will start operating in a few years at a centre-of-mass energy of 500 GeV initially and will then be upgraded to 1 TeV [163]. The other one is the Compact Linear Collider (CLIC) which will start at 380 GeV and will go upto 3 TeV in its final stage of run [164]. This is expected to come somewhat later, perhaps as the LHC is finishing its run.

Though the primary goal for the proposed  $e^+e^-$  colliders is precision measurement, they also provide an excellent opportunity for searches for new physics beyond the SM. In the previous chapter, we see that the study of the LED model at the LHC shows the moderate usefulness of a hadron collider. We, therefore, study an analogous process in the context of proposed linear colliders.

In this chapter, we describe our studies of the signal for LED at the two proposed  $e^+e^-$  colliders, using the analogous process  $e^+e^- \rightarrow t\bar{t}G_{\tilde{\pi}}^1$ . As in a hadron collider, however, the dominant process will be  $e^+e^- \rightarrow \gamma G_{\tilde{\pi}}$ , leading to a final state with an isolated photon and large missing  $p_T$ . At projected ILC centre-of-mass energies like 250 GeV and 500 GeV, the cross-sections with  $M_D \sim 5$  TeV are so low even for this dominant process that nothing will be detectable above the SM background from  $e^+e^- \rightarrow \gamma\nu\bar{\nu}$ . However, for machine energies like 1 TeV at the final run of ILC or 3 TeV at the CLIC, cross-sections will be sizeable and may prove enough to probe the model.

---

<sup>1</sup>KK gravitons, denoted as  $\tilde{h}_{\mu\nu}^{(\tilde{\pi})}$  in Chapter 2, will be denoted as  $G_{\tilde{\pi}}$  in this chapter.

Though the analysis techniques in this work are very similar to those described in the previous section, important differences arise because of the nature of the machine. At a hadron collider like the LHC, the available centre-of-mass energy is variable from event to event and is also, for all practical purposes, considerably less than the machine energy. On the other hand, at an  $e^+e^-$  machine, the centre-of-mass energy is constant and equal to the machine energy. Thus, even a 1 TeV  $e^+e^-$  collider could lead (for a very high luminosity) to observable signals, and a 3 TeV machine can actually improve on the 13 TeV LHC projections even with moderate luminosity.

## 6.2 $t\bar{t}G_{\bar{n}}$ signal at the ILC

At the ILC, the proposed energy for initial run is 500 GeV with an option of upgrading it to 1 TeV. With machine energy as low as 500 GeV, the ILC will not be very effective to search for LED signals with  $M_D \gtrsim 5$  TeV which is the current lower bound on  $M_D$  from LHC monojet + MET searches [157, 158]. Therefore, we start our analysis assuming  $\sqrt{s} = 1$  TeV at the ILC.

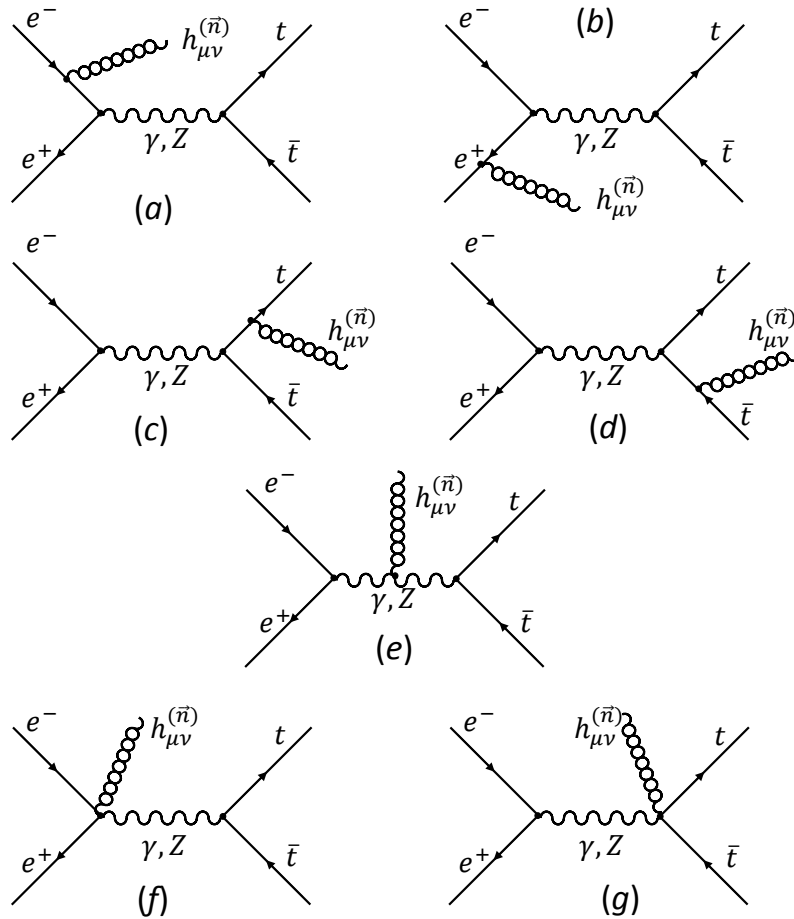


Figure 6.1: Tree-level Feynman diagrams for the process  $e^+e^- \rightarrow t\bar{t}G_{\bar{n}}$ .

We have considered the process

$$e^+e^- \longrightarrow t\bar{t}G_{\bar{n}}$$

The tree-level Feynman diagrams for the process can easily be drawn from the SM diagrams for  $e^+e^- \rightarrow t\bar{t}$  process. Since KK graviton couples to all the matter particles irrespective of their spin, flavour or colour, we obtain diagrams for the process with a graviton emitted from one of the legs or the propagators or the vertices. The tree-level Feynman diagrams for the process are shown in Figure 6.1. There are total 14 diagrams with 7 diagrams for photon mediated and 7 for  $Z$  mediated. The calculation is considerably simpler than the hadronic production since we have 14 diagrams instead of 28. The amplitudes for the process are given in Appendix B. The principal backgrounds are again  $t\bar{t}$  production and  $t\bar{t}Z(\nu\bar{\nu})$  production, the latter arising from 9 Feynman diagrams. Once again the results were subjected to different analytic and numerical checks to ensure their correctness.

Depending upon the decay mode of top-pair, as described before in Chapter 5, we will again have three types of final states viz.  $\ell^+\ell^- + \text{jets} + \text{MET}$ ,  $\ell^\pm + \text{jets} + \text{MET}$ , and  $\text{jets} + \text{MET}$ . Here again we made a cut-based analysis to increase signal significance. As in the analysis for LHC, at 1 TeV, we found a useful set of kinematic cuts by searching over  $10^3$  random sets and optimising for signal significance and a reasonable number of events.

### 6.2.1 Dilepton final states

The signal cross-sections at a 1 TeV machine are rather poor, and the dilepton signal, though clear, is doubly suppressed by the leptonic branching ratio of the  $W$ . In our cut-based analysis, we divided these cuts into four different sets more-or-less according to the conventions established in Chapter 5. Once again,  $p_T$  cuts on visible final state particles are less effective than angular cuts, but a lower cut on  $\cancel{p}_T$  is very effective in background suppression. These results are shown in Table 6.1 which is analogous, for the  $\ell^+\ell^- + \text{jets} + \text{MET}$  signal, to Table 5.3 in the previous chapter.

Set	Cuts	$\sigma_{t\bar{t}}$ [ab]	$\sigma_{t\bar{t}Z}$ [ab]	$\sum_n \sigma_{t\bar{t}G_n}$ [ab]
A	$\eta_\ell < 3, \eta_j < 3.5$ $\Delta R_{\ell j} > 0.4, \Delta R_{\ell_1 \ell_2} > 0.2, \Delta R_{j_1 j_2} > 0.7$ $p_{T\ell_1} > 20 \text{ GeV}, p_{T\ell_2} > 20 \text{ GeV}, p_{Tj} > 20 \text{ GeV}$ $\cancel{p}_T > 20 \text{ GeV}$	4329.4	26.029	0.7552
B	Set A + $p_{T\ell_1} < 250 \text{ GeV}$ $p_{T\ell_2} < 200 \text{ GeV}, p_{Tj} < 250 \text{ GeV}$	2564.1	22.746	0.7212
C	Set B + $\Delta R_{j_1 j_2} < 2.0, \Delta R_{\ell_1 \ell_2} < 2.2$	1.4740	1.6125	0.1777
Final	Set C + $\cancel{p}_T > 150 \text{ GeV}$	0.4872	1.0917	0.1437

**Table 6.1:** List of sets of cuts for  $\ell^+\ell^- + \text{jets} + \text{MET}$  signal and their effects on the cross-sections at  $\sqrt{s} = 1$  TeV. The signal is computed for  $n = 3$  and  $M_D = 6.2$  TeV.

The cuts in Table 6.1 are slightly less effective than those in Table 5.3, for the reduction in the  $t\bar{t}$  and  $t\bar{t}Z$  backgrounds are by factors around 9,000 and 25 respectively, whereas the signal is reduced by a factor of 5, as before. The significance can certainly be improved by making the cuts more stringent, but this would completely remove the already vanishingly-small signal. The effectiveness of these cuts are represented graphically in the left panel of the Figure 6.2. The

notations and conventions of this figure closely follow those of Figure 5.4. It may be seen from

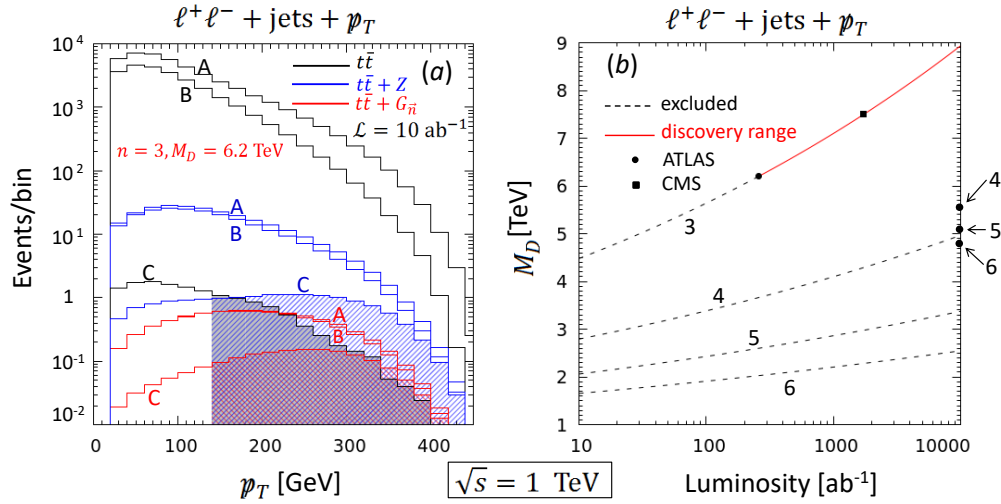


**Figure 6.2:** Analysis of the  $\ell^+\ell^- + \text{jets} + \text{MET}$  signal vis-à-vis background at a 1 TeV  $e^+e^-$  collider. The left panel (a) shows the  $p_T$  distribution of signal vs.  $t\bar{t}$  and  $t\bar{t}Z$  backgrounds and the right panel (b) shows the 95% discovery plot as a function of integrated luminosity. The notations and conventions are exactly as in Figure 5.3.

the left panel (a) that the signal, after imposing all the cuts, is well below the irreducible  $t\bar{t}Z$  background. Observation of such a small signal is difficult unless one can achieve the enormous value of  $\sim 100$  ab $^{-1}$  luminosity at a 1 TeV machine. This is apparent from the right panel (b) showing the 95% C.L. discovery limit of  $M_D$  as a function of integrated luminosity for different (marked) numbers of extra dimensions.

### 6.2.2 Single lepton final states

The mono-lepton signal is also very poor although we gain a factor of 3 from the hadronic branching ratio of  $W$ . Unlike the LHC case where the mono-lepton signal was the best signal, here it is slightly less useful than the dilepton final state. In Table 6.2, we show the sets of cuts. The conventions and notations are exactly the same as those of Table 6.1. In this case, the  $t\bar{t}$

Set	Cuts	$\sigma_{t\bar{t}}$ [ab]	$\sigma_{t\bar{t}Z}$ [ab]	$\sum_n \sigma_{t\bar{t}G_n}$ [ab]
A	$\eta_\ell < 3, \eta_j < 3.5, \Delta R_{\ell j} > 0.4, \Delta R_{j_1 j_2} > 0.7$ $p_{T\ell} > 20$ GeV, $p_{Tj} > 30$ GeV, $p_T > 20$ GeV	10164.1	84.783	2.3646
B	Set A + $40$ GeV $< p_{T\ell} < 225$ GeV $30$ GeV $< p_{Tj_1} < 180$ GeV $30$ GeV $< p_{Tj_i} < 110$ GeV ( $i = 2, 3, 4$ )	1807.2	29.51	1.0926
C	Set B + $0.4 < \Delta R_{\ell j} < 3.0, 0.7 < \Delta R_{j_1 j_2} < 3.0$	0.8738	8.4515	0.6954
Final	Set C + $p_T > 200$ GeV	0.0	2.7763	0.3952

**Table 6.2:** List of sets of cuts for  $\ell^\pm + \text{jets} + \text{MET}$  signal and their effects on the cross-sections at  $\sqrt{s} = 1$  TeV. The signal is computed for  $n = 3$  and  $M_D = 6.2$  TeV.

background is removed almost completely, but  $t\bar{t}Z$  remains as an irreducible background.

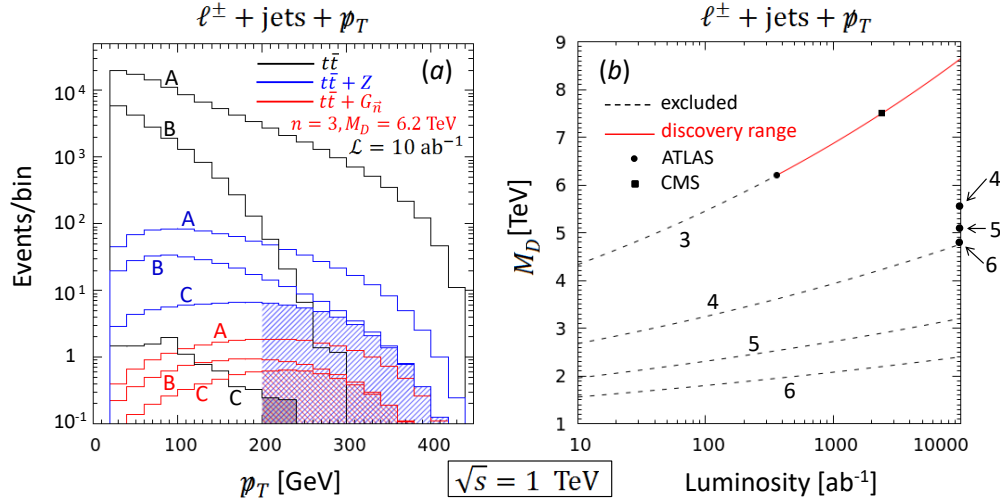


**Figure 6.3:** Analysis of the  $\ell^\pm + \text{jets} + \text{MET}$  signal vis-à-vis background at a 1 TeV  $e^+e^-$  collider. The left panel (a) shows the  $p_T$  distribution of signal vs.  $t\bar{t}$  and  $t\bar{t}Z$  backgrounds and the right panel (b) shows the 95% discovery plot as a function of integrated luminosity. The notations and conventions are exactly as in Figure 6.2.

In Figure 6.3(a), we show the effect of the cuts for  $\ell^\pm + \text{jets} + \text{MET}$  final state events following the conventions of Figure 6.2. As we see from the figure that the blue histogram corresponding to  $t\bar{t}Z$  background remains as an irreducible background. Figure 6.3(b) shows discovery limit at 95% C.L. above the SM background. It can be seen that the luminosity requirement for this channel is almost the same as the dilepton channel. The advantage due to hadronic decay of one of the  $W$  does not remain effective due to lower efficiency in the jet tagging.

### 6.2.3 Hadronic final states

For hadronic final states, although we gain from the hadronic branching fraction, we do not get much to be observed within few  $\text{ab}^{-1}$  of luminosity. The cross-section is rather poor due to the low machine energy. With the same convention as set in Table 6.1, we list in Table 6.3 the kinematic sets of cuts that gives best significance with  $10 \text{ ab}^{-1}$  luminosity. Since there is no source for  $\cancel{p}_T$  in case of pure hadronic decay of  $t\bar{t}$  background, the  $t\bar{t}$  background events have  $\cancel{p}_T$  smaller than 60 GeV. Hence, in this case, slightly hard lower cut on missing  $p_T$  removes the  $t\bar{t}$  background completely. However, background events from  $t\bar{t}Z$  process will remain irreducible. Though the signal significance is small, the effects of the sets of cuts is very apparent from the cross-section listed in the table.

Set	Cuts	$\sigma_{t\bar{t}}$ [ab]	$\sigma_{t\bar{t}Z}$ [ab]	$\sum_n \sigma_{t\bar{t}G_n}$ [ab]
A	$N_j \geq 2, \eta_j < 3.5$ $p_{Tj} > 20 \text{ GeV}, \cancel{p}_T > 20 \text{ GeV}$	213.5	91.65	2.832
B	Set A + $20 \text{ GeV} < p_{Tj} < 200 \text{ GeV}$	160.8	57.71	1.945
C	Set B + $\Delta R_{j_1 j_2} < 2.5$	6.129	24.02	1.532
Final	Set C + $\cancel{p}_T > 200 \text{ GeV}$	0.0	9.178	0.9775

**Table 6.3:** List of sets of cuts for  $\text{jets} + \text{MET}$  signal and their effects on the cross-sections at  $\sqrt{s} = 1 \text{ TeV}$ . The signal is computed for  $n = 3$  and  $M_D = 6.2 \text{ TeV}$ .

The effect of the cuts can be seen graphically in Figure 6.4(a). The reduction in  $t\bar{t}$  background is high, but signal is too low to be observed above the background fluctuation at  $10 \text{ ab}^{-1}$  luminosity. However, this is the best signal among all three at a 1 TeV  $e^+e^-$  collider. This can be seen in the right panel of Figure 6.4(b). The conventions for this plot same as those of Figure 6.2.

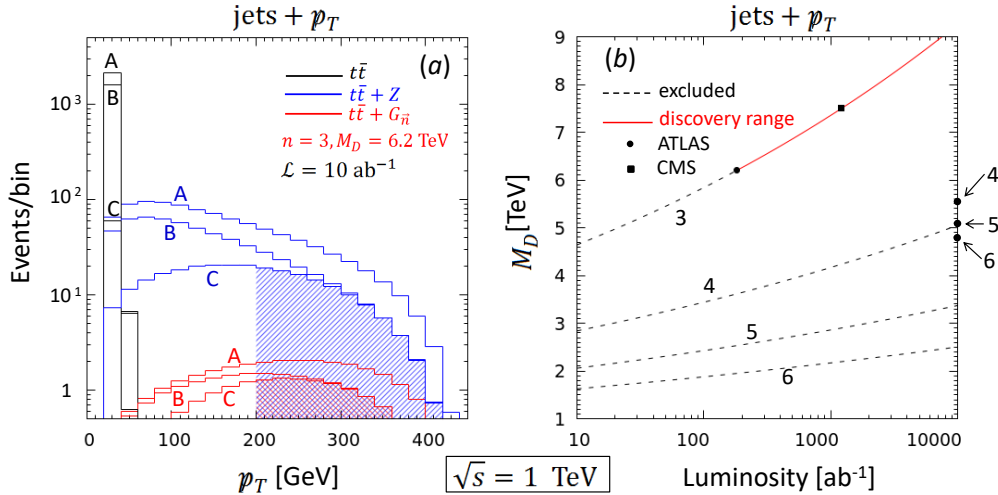


**Figure 6.4:** Analysis of the jets + MET signal vis-à-vis background at a 1 TeV  $e^+e^-$  collider. The left panel (a) shows the  $p_T$  distribution of signal vs.  $t\bar{t}$  and  $t\bar{t}Z$  backgrounds and the right panel (b) shows the 95% discovery plot as a function of integrated luminosity. The notations and conventions are exactly as in Figure 6.2.

It is quite clear from the above analyses that for  $n = 3$ , a string scale up to 7 TeV may be observable — provided one can achieve the absurdly high luminosity of  $\sim 10^3 \text{ ab}^{-1}$ . The signals for  $n \geq 4$  are impossible to observe at a 1 TeV machine. This is not unexpected, but our analysis simply makes precise what can be guessed qualitatively. In effect, there will be no observable signals for gravitons in top-quark pair production at the ILC. However, the story is very different at a 3 TeV machine.

### 6.3 $t\bar{t}G_{\tilde{n}}$ Signals at the CLIC

Given that LED signals are typically suppressed by a factor  $(s/M_D^2)^{n/2}$ , it is easy to see that the rise in centre-of-mass energy from 1 TeV to 3 TeV will improve the cross-section by a factor that varies from around 27 to 729 as  $n$  changes from 3 to 6. Accordingly, projections for LED at a 3 TeV machine like the CLIC will be far more optimistic than at a 1 TeV machine. This is borne out by our detailed analysis.

Once again, our choice of cuts and total cross-sections after imposing these for all three types of final states are shown in Table 6.4 which is analogous, in all respects, to the two previous ones. However, in this case, the cuts are very effective in reducing the  $t\bar{t}$  background, but the  $t\bar{t}Z$  background is reduced only about 10 times. Nevertheless, the signal drops only marginally, to about half, so the significance is still good. Moreover, the signal is much larger, as expected.

The larger signal emboldens us to take, in all the panels of Figure 6.5, a higher value of  $M_D = 15 \text{ TeV}$ , which may well be the experimental limit by the time a 3 TeV machine could become

$\ell^+\ell^- + \mathbf{jets} + \cancel{p}_T$ 

Set	Cuts	$\sigma_{t\bar{t}}$ [ab]	$\sigma_{t\bar{t}Z}$ [ab]	$\sum_n \sigma_{t\bar{t}G_n}$ [ab]
A	$\eta_\ell < 3, \eta_j < 3.5$ $\Delta R_{\ell j} > 0.4, \Delta R_{\ell_1 \ell_2} > 0.2, \Delta R_{j_1 j_2} > 0.7$ $p_{T\ell} > 50 \text{ GeV}, p_{Tj} > 50 \text{ GeV}, \cancel{p}_T > 50 \text{ GeV}$	151.84	4.732	8.696
B	Set A + $p_{T\ell_1} < 1000 \text{ GeV}, p_{T\ell_2} < 800 \text{ GeV}$ $p_{Tj} < 800 \text{ GeV}$	132.18	4.543	8.601
C	Set B + $\Delta R_{j_1 j_2} < 2.5, \Delta R_{\ell_1 \ell_2} < 2.5$	0.0	0.6241	5.717
Final	Set C + $\cancel{p}_T > 400 \text{ GeV}$	0.0	0.5146	5.134

 $\ell^\pm + \mathbf{jets} + \cancel{p}_T$ 

Set	Cuts	$\sigma_{t\bar{t}}$ [ab]	$\sigma_{t\bar{t}Z}$ [ab]	$\sum_n \sigma_{t\bar{t}G_n}$ [ab]
A	$\eta_\ell < 3, \eta_j < 3.5, \Delta R_{\ell j} > 0.4, \Delta R_{j_1 j_2} > 0.7$ $p_{T\ell} > 50 \text{ GeV}, p_{Tj} > 30 \text{ GeV}, \cancel{p}_T > 20 \text{ GeV}$	692.2	14.41	20.670
B	Set A + $50 \text{ GeV} < p_{T\ell} < 800 \text{ GeV}$ $30 \text{ GeV} < p_{Tj_1} < 800 \text{ GeV}$ $30 \text{ GeV} < p_{Tj_i} < 600 \text{ GeV} (i = 2, 3, 4)$	186.5	6.490	12.085
C	Set B + $0.4 < \Delta R_{\ell j} < 3.0, 0.7 < \Delta R_{j_1 j_2} < 3.0$	0.0	1.402	10.147
Final	Set C + $\cancel{p}_T > 500 \text{ GeV}$	0.0	1.043	8.866

 $t\bar{t} + \cancel{p}_T$ 

Set	Cuts	$\sigma_{t\bar{t}}$ [ab]	$\sigma_{t\bar{t}Z}$ [ab]	$\sum_n \sigma_{t\bar{t}G_n}$ [ab]
A	$N_j \geq 2, \eta_j < 3.5, p_{Tj} > 20 \text{ GeV}$	775.8	11.13	4.991
B	Set A + $20 \text{ GeV} < p_{Tj_1} < 1300 \text{ GeV}$ $20 \text{ GeV} < p_{Tj_i} < 1000 \text{ GeV} (i > 1)$	160.8	7.859	4.887
C	Set B + $\Delta R_{j_1 j_2} < 3.0$	0.0	1.834	4.441
Final	Set C + $\cancel{p}_T > 600 \text{ GeV}$	0.0	1.174	3.646

**Table 6.4:** List of sets of cuts and their effects on the cross-sections at  $\sqrt{s} = 3 \text{ TeV}$  for three types of final states. The signals are computed for  $n = 3$  and  $M_D = 15 \text{ TeV}$ .

operational, assuming that the LHC continues to find results consistent with the SM. Even with this higher value of  $M_D$ , the signal at 3 TeV is significantly larger than the  $t\bar{t}Z$  background. This happy state of affairs is reflected in Figure 6.6, where for all the values of  $n$ , the discovery range would clearly be better than the current LHC bounds even with very modest values of integrated luminosity.

It appears, then, that if there are large extra dimensions, and the value of the string scale lies somewhere in the range of 10 – 20 TeV, a 3 TeV  $e^+e^-$  collider like the proposed CLIC, would be an ideal machine to search for such LED effects as studied above. However, one would then expect even larger signals for the dominant  $e^+e^- \rightarrow \gamma G_{\bar{n}}$  channel. Thus, as at the LHC, the

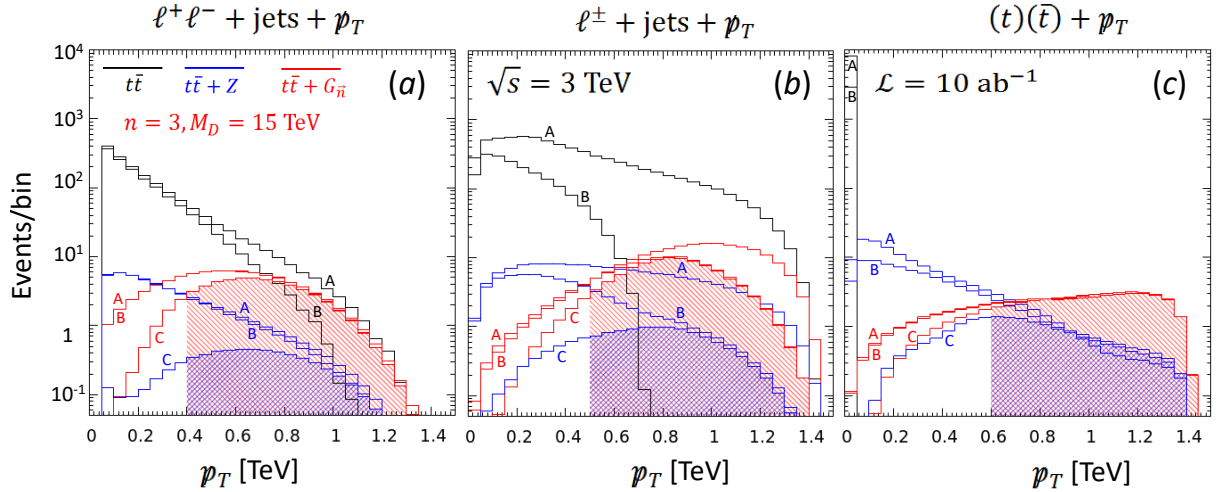


Figure 6.5: The  $p_T$  distributions of signal vs.  $t\bar{t}$  and  $t\bar{t}Z$  backgrounds are shown for (a)  $\ell^+\ell^- + \text{jets} + \cancel{p}_T$ , (b)  $\ell^\pm + \text{jets} + \cancel{p}_T$  and (c)  $\text{jets} + \cancel{p}_T$  signals. The notations and conventions are exactly as in Figure 6.2(a).

$t\bar{t}G_{\bar{n}}$  process should only be thought of as a confirmatory process. We now take up this issue in more detail.

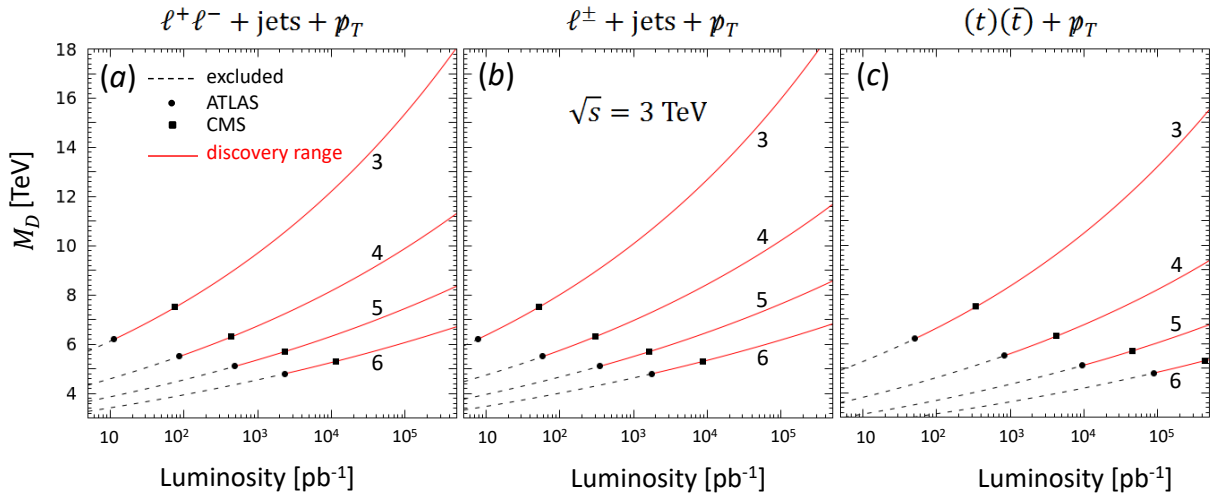


Figure 6.6: Analysis of the signal vis-à-vis background at a 3 TeV  $e^+e^-$  collider. The 95% discovery plots as a function of integrated luminosity are shown (a)  $\ell^+\ell^- + \text{jets} + \cancel{p}_T$ , (b)  $\ell^\pm + \text{jets} + \cancel{p}_T$  and (c)  $\text{jets} + \cancel{p}_T$  signals. The notations and conventions are exactly as in Figure 6.2(b).

## 6.4 Correlation between mono-photon + MET and $t\bar{t}$ + MET

In Chapter 5, it was shown that the usefulness of the  $t\bar{t}G_{\bar{n}}$  final states becomes apparent when we make a correlation plot of its cross-section against that of the monojet process. In the present case, similar results may be obtained by plotting against the mono-photon process.

These are shown in Figure 6.7, where we have chosen the signals which gives the best significance at two different energies, i.e.  $\text{jets} + \cancel{p}_T$  signal at 1 TeV machine and  $\ell^\pm + \text{jets} + \cancel{p}_T$  signal for 3 TeV machine. The left panel, i.e. Figure 6.7(a) shows the correlation between  $\gamma + \cancel{p}_T$  vs.  $\text{jets} + \cancel{p}_T$  events at 1 TeV with  $100 \text{ ab}^{-1}$  luminosity. The right panel, on the other hand, shows the correlation between  $\gamma + \cancel{p}_T$  vs.  $\ell^\pm + \text{jets} + \cancel{p}_T$  events at 3 TeV with  $1 \text{ ab}^{-1}$  luminosity.

The colour convention is the same as Figure 5.6. The figure clearly illustrates the difficulty of identifying LED signals at 1 TeV and the comparative ease of doing the same at 3 TeV.

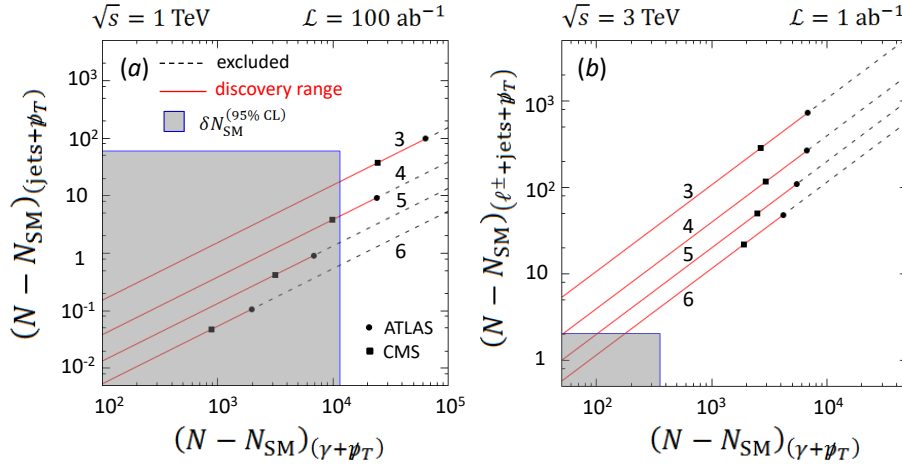


**Figure 6.7:** Correlation plots showing event numbers for (a) mono-photon +  $p_T$  vs. jets +  $p_T$  events at 1 TeV with  $100 \text{ ab}^{-1}$  luminosity, and for (b) mono-photon +  $p_T$  vs.  $\ell^\pm + \text{jets} + \text{MET}$  events at 3 TeV with  $1 \text{ ab}^{-1}$  luminosity. All notations and conventions are identical to Figure 5.6.

## 6.5 LED Signals at Very High Energy $e^+e^-$ Colliders

After the analysis at 1 TeV and 3 TeV  $e^+e^-$  colliders, it is natural to explore for ADD signals at a very high energy linear collider. Unlike a hadron collider, an  $e^+e^-$  machine has two advantages. First, unitarity guarantees us that the cross-sections for SM background processes decrease with machine energy and thereby less SM background at higher energies. Secondly, the cross-sections for signals increase with machine energy as it approaches to the cutoff scale of the theory after which the perturbativity is no longer applied to the processes. This is because gravitons couple to the energy-momentum of the initial and final states, and these grow larger as the energy increases. Even within the perturbative region, the cross-section increases dramatically with the energy. Unitarity is not an issue since this is just a low-energy effective theory of some (presumably UV-complete) theory beyond the cutoff.

The results of our first attempt at a numerical analysis are shown in Figure 6.8. In the three panels of Figure 6.8, we have plotted the signal cross-section in red for different values of extra dimensions written alongside the curves. The three panels from left to right are for (a)  $\ell^+\ell^- + \text{jets} + \text{MET}$ , (b)  $\ell^\pm + \text{jets} + \text{MET}$  and (c) jets + MET final state processes. The SM  $t\bar{t}$  and  $t\bar{t}Z$  backgrounds are plotted in black and blue respectively. The signals and backgrounds are computed with cuts  $p_{T_l}, p_{T_j}, p_{T_{\text{mis}}} > 100 \text{ GeV}$  and  $\eta_{l,j} < 3.0$  and  $M_D = 50 \text{ TeV}$ .

Of course, as expected, for  $\sqrt{s} = 1$  and 3 TeV, the signals are much smaller than the SM backgrounds (we must note that the cuts applied here are minimal and not optimised for background elimination). As machine energy increases, the signal increases rapidly with a typical scaling  $(s/M_D^2)^{n/2}$  and SM backgrounds decrease as  $1/s$ .

These figures make it quite clear that a high energy  $e^+e^-$  collider will be more effective in finding ADD signal than a corresponding high energy hadron collider.

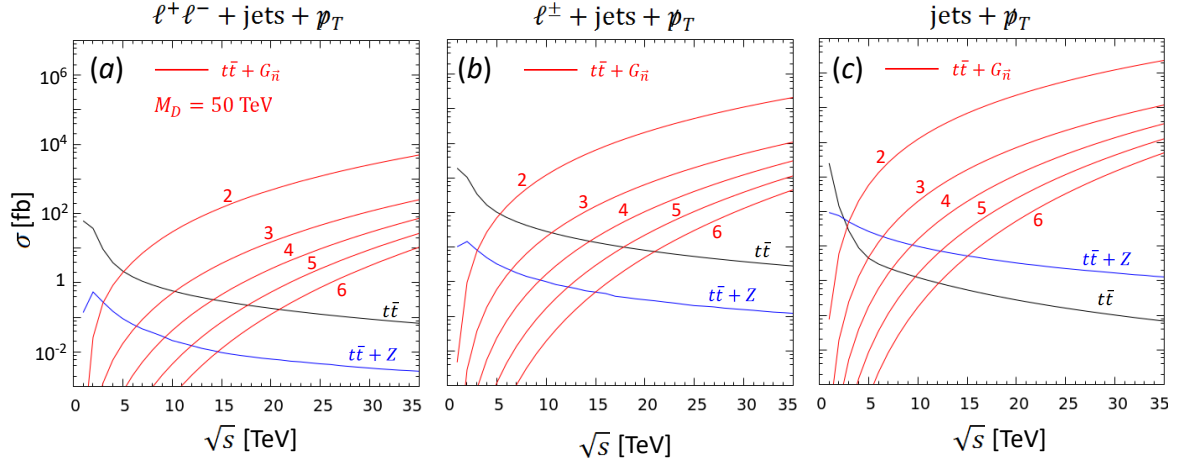


**Figure 6.8:** Variation of cross-section as a function of machine energy for (a)  $\ell^+\ell^- + \text{jets} + \text{MET}$ , (b)  $\ell^\pm + \text{jets} + \text{MET}$  and (c)  $\text{jets} + \text{MET}$  signals (in red),  $t\bar{t}$  (in black) and  $t\bar{t}Z$  (in blue) backgrounds. The number alongside the red curves indicates the number of extra dimensions for signal processes. The signals and backgrounds are computed with cuts  $p_{T_l}, p_{T_j}, p_{T_{\text{mis}}} > 100$  GeV and  $\eta_{l,j} < 3.0$  and  $M_D = 50$  TeV.

## 6.6 Summary

In this chapter we have investigated the prospects of probing the TeV-range bulk Planck scale  $M_D$  at the proposed linear colliders, viz. ILC and CLIC.

We have studied missing energy signal of the process  $e^+e^- \rightarrow t\bar{t}G_{\bar{n}}$  at the ILC and CLIC. The process will give rise to three types of final states viz.  $\ell^+\ell^- + \text{jets} + \text{MET}$ ,  $\ell^\pm + \text{jets} + \text{MET}$  and  $\text{jets} + \text{MET}$ . At the 1 TeV ILC machine, the signal for ADD in all the three types of final states is very poor. For  $n = 3$ , luminosity requirement is more than  $100 \text{ ab}^{-1}$  to reach the current bounds from the LHC on  $M_D$  even for best signal of  $\text{jets} + \text{MET}$  in the process. Signals for  $n = 4, 5$  and  $6$  are almost impossible to observe even with this impossibly large projected luminosity. This implies that there is almost no possibility of finding ADD effects in top-antitop processes at the ILC at 1 TeV.

At the 3 TeV CLIC, however, much better results can be obtained, even with moderate luminosity. The results at the CLIC are better than the LHC result since each event at the CLIC has a centre-of-mass energy of 3 TeV, but it is generally much lower in the case of the LHC. The luminosity requirement is less than  $1 \text{ fb}^{-1}$  to reach current LHC bounds for  $n = 3, 4, 5$  and  $6$ . A correlated study between  $e^+e^- \rightarrow \gamma G_{\bar{n}}$  vs.  $e^+e^- \rightarrow t\bar{t}G_{\bar{n}}$  has also been done in this work. This correlation, though not very effective at 1 TeV ILC, gives a very good resolution to probe ADD model at the 3 TeV CLIC.

We also made a simple study of the same processes at very high energy  $e^+e^-$  colliders. The study shows that a very high energy  $e^+e^-$  collider is better to search for ADD model with higher bulk Planck scale  $M_D$ . The advantages in high energy linear collider are because (a) SM backgrounds decrease at high energies and (b) cross-sections for the signals increase since the collider energy approaches to cutoff scale. It also suggests that a linear collider will be better to look for ADD signals than a hadron collider.

# CHAPTER 7

---

## Summary and Conclusions

---

Models with extra spatial dimensions remain one of the most elegant explanations to address the hierarchy problem of the Standard Model. This thesis made some collider studies of two well-known types of model with extra dimensions.

The RS model of warped extra dimension of topology  $\mathbb{S}^1/\mathbb{Z}_2$  has two branes situated at the two fixed points. One of which is called the IR brane where the SM fields remain confined and the other is the UV brane where gravitational interactions become strong. The stabilisation of the inter-brane distance is the key to its success to solve the hierarchy problem. The stabilisation is achieved via a Goldberger-Wise mechanism. The minimal RS model stabilized by GW mechanism predicts a light dilatonic scalar called radion. This radion, which interacts with the 4D SM fields via the trace of the energy-momentum tensor can, in principle, mix with the Higgs boson of the SM. While a pure radion is constrained from LHC data, a mixed radion has some room in the parameter space. We investigated direct and indirect signals for a mixed radion state, with kinetic mixing with the SM Higgs, occurring through a parameter  $\xi$ . Constraints on this from measurement of the properties of the observed 125 GeV scalar are not very strong, but non-observation of the counterpart heavy scalar puts stringent constraint on the parameter space of the study. A 13-14 TeV machine will rule out a significant part of the parameter space if a heavy scalar is not found.

An interesting region of the parameter space in the mixed-radion case, called the ‘conformal point’, is where the tree-level couplings of the heavy scalar to SM particles vanish except for the couplings with the gauge bosons of the Standard Model which have extra contributions from the trace anomaly term. This region is very weakly constrained by current measurements by both ATLAS and CMS. Interestingly, an explanation for the highly-exotic 750 GeV proto-resonance in  $\gamma\gamma$  final states at the LHC could have been in terms of the heavy scalar at the conformal point. However, with the demise of the 750 GeV ‘resonance’, this explanation is now purely academic.

The model with Large Extra Dimensions considers more than one extra compact spatial dimensions. The large size of the extra dimensions reduces the fundamental scale of gravity in the bulk to as low as the scale of the electroweak interaction. In the ADD framework, the SM fields are confined to a single brane and the gravity can propagate to the bulk. Here, only the graviton

has massive KK states and they form a quasi-continuum of masses. These KK gravitons, being weakly coupled to the SM fields, are not detectable individually in an experiment, and hence, contribute to the missing transverse energy and momentum in the collider experiments. We investigated, successively, direct signals in MET in ADD model in processes where a graviton is produced along with a top-quark pair at the currently-running 13 TeV hadron collider, viz. the LHC. It turns out that the LHC may verify the signal at 95% C.L. in the near future with  $300 \text{ fb}^{-1}$  of luminosity. A comparative study with the `monojet + MET` signal would also be useful to confirm the ADD signal.

We further studied an analogous process at the future  $e^+e^-$  colliders. At a 1 TeV  $e^+e^-$  collider, the machine energy is too low to yield good signal significance and the signal is difficult to observe beyond the current lower bound from the LHC. However, at a 3 TeV machine, there are good chances of observing this signal, along with others. A high energy  $e^+e^-$  collider will be more useful to observe the ADD signal since the cross-section for the signal increases and that of the SM backgrounds decrease with the increase of machine energy.

Although this thesis primarily focuses on the extra dimensional models, it focusses on some specific studies. There is, of course, scope for many more studies of extra dimensional models in the context of colliders or other experiments. In the case of RS model of warped extra dimension, there is an interesting possibility of allowing the SM fields to access the bulk. These bulk fields will have their own KK modes. Direct and indirect signatures for these KK modes are an interesting area of new physics searches. On the other hand, the study of signature for ADD model from astrophysical observations is also interesting. The possibility that LED model can provide an explanation for small masses of neutrino, the study of the signatures of this possibility also remains an interesting region to look for. Another possibility, where the hierarchy problem is not addressed, is the *universal extra dimensions* (UED) class of models, where there is an extra dimension of the form  $\mathbb{S}_1/\mathbb{Z}_2$  which can be accessed by all fields.

Extra dimensional models are interesting theoretically, but the fate of the models relies heavily on the current and future collider experiments. Though the LHC runs, with their negative results for all physics beyond the Standard Model, have pushed the constraints on models with extra dimensions to the edge, so far as the LHC is concerned, these models are still very much viable, when more data accumulate. If and when a high-energy  $e^+e^-$  collider is built, we can also get information about such models. It may be hoped that, with more data from the LHC as well as the running of proposed linear colliders, some of the works presented in this thesis will become useful to study the models with extra dimensions.

# APPENDIX A

## Amplitudes for LED Signals at the LHC

### A.1 Radiated tensor graviton KK modes :

$$P(k_1) + P(k_2) \rightarrow t(P_1) + \bar{t}(P_2) + h_{\alpha\beta}^{(\tilde{n})}(P_3)$$

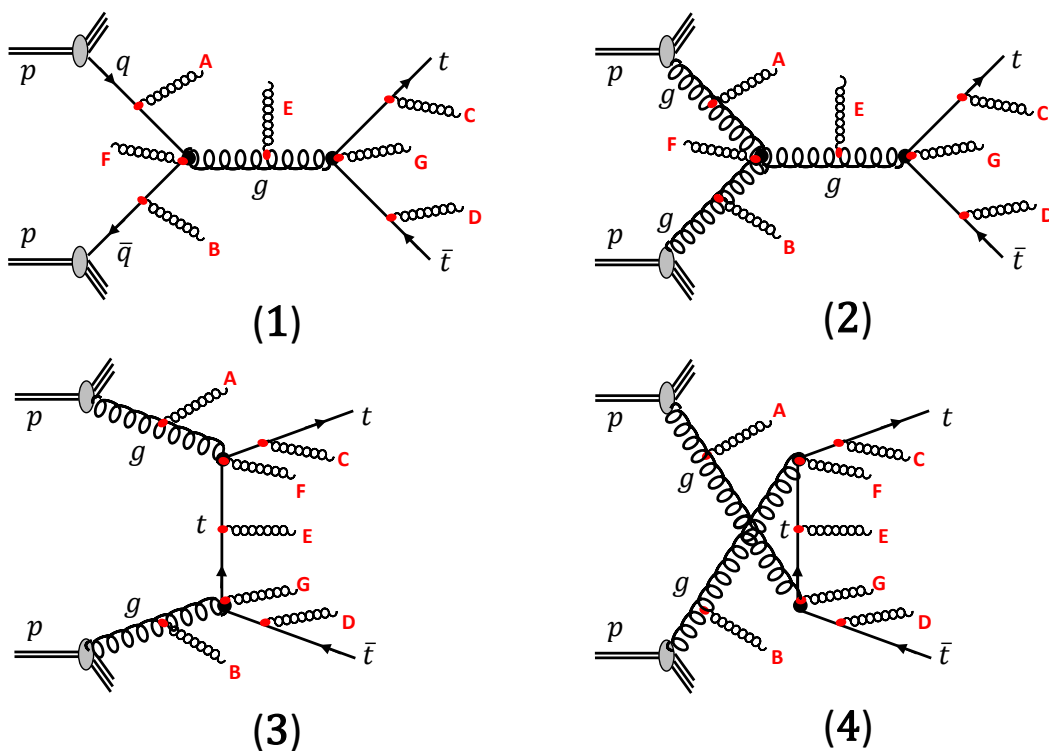


Figure A.1: Figure shows diagrams of the signal processes at the LHC.

where, for quark-initiated processes,

$$\mathcal{M}_2 = \left( \mathcal{M}_{2A}^{(1)} + \mathcal{M}_{2B}^{(1)} + \mathcal{M}_{2C}^{(1)} + \mathcal{M}_{2D}^{(1)} + \mathcal{M}_{2E}^{(1)} + \mathcal{M}_{2F}^{(1)} + \mathcal{M}_{2G}^{(1)} \right) \quad (\text{A.1})$$

and for gluon-initiated processes,

$$\mathcal{M}_2 = \sum_{i=2}^4 \left( \mathcal{M}_{2A}^{(i)} + \mathcal{M}_{2B}^{(i)} + \mathcal{M}_{2C}^{(i)} + \mathcal{M}_{2D}^{(i)} + \mathcal{M}_{2E}^{(i)} + \mathcal{M}_{2F}^{(i)} + \mathcal{M}_{2G}^{(i)} \right) \quad (\text{A.2})$$

where the indices  $A$  to  $G$  refer to the diagrams in Figure A.1. The label should be read only one of the  $A$  to  $G$ . The individual terms are listed below.

**For quark-initiated processes :**

$$\begin{aligned} \mathcal{M}_{2A}^{(1)} &= \frac{i\kappa g_s^2}{8} [T_c]_{nm} [T_c]_{ij} \frac{1}{q'^2 (k_1 - P_3)^2} \epsilon^{\alpha\beta} (P_3)^* \\ &\times \bar{v}_n(k_2) \gamma_\rho (\not{k}_1 - \not{P}_3) \left[ \gamma_\alpha (2k_1 - P_3)_\beta + \gamma_\beta (2k_1 - P_3)_\alpha \right] u_m(k_1) \\ &\times \bar{u}_i(P_1) \gamma^\rho v_j(P_2) \end{aligned} \quad (\text{A.3})$$

$$\begin{aligned} \mathcal{M}_{2B}^{(1)} &= \frac{i\kappa g_s^2}{8} [T_c]_{nm} [T_c]_{ij} \frac{1}{q'^2 (k_2 - P_3)^2} \epsilon^{\alpha\beta} (P_3)^* \\ &\times \bar{v}_n(k_2) \left[ \gamma_\alpha (2k_2 - P_3)_\beta + \gamma_\beta (2k_2 - P_3)_\alpha \right] (\not{k}_2 - \not{P}_3) \gamma_\rho u_m(k_1) \\ &\times \bar{u}_i(P_1) \gamma^\rho v_j(P_2) \end{aligned} \quad (\text{A.4})$$

$$\begin{aligned} \mathcal{M}_{2C}^{(1)} &= \frac{i\kappa g_s^2}{8} [T_c]_{nm} [T_c]_{ij} \frac{1}{q^2 [(P_1 + P_3)^2 - m_t^2]} \epsilon^{\alpha\beta} (P_3)^* \\ &\times \bar{v}_n(k_2) \gamma_\rho u_m(k_1) \\ &\times \bar{u}_i(P_1) \left[ \gamma_\alpha (2P_1 + P_3)_\beta + \gamma_\beta (2P_1 + P_3)_\alpha \right] (\not{P}_1 + \not{P}_3 + m_t) \gamma^\rho v_j(P_2) \end{aligned} \quad (\text{A.5})$$

$$\begin{aligned} \mathcal{M}_{2D}^{(1)} &= \frac{i\kappa g_s^2}{8} [T_c]_{nm} [T_c]_{ij} \frac{1}{q^2 [(P_2 + P_3)^2 - m_t^2]} \epsilon^{\alpha\beta} (P_3)^* \\ &\times \bar{v}_n(k_2) \gamma_\rho u_m(k_1) \\ &\times \bar{u}_i(P_1) \gamma^\rho (\not{P}_2 + \not{P}_3 - m_t) \left[ \gamma_\alpha (2P_2 + P_3)_\beta + \gamma_\beta (2P_2 + P_3)_\alpha \right] v_j(P_2) \end{aligned} \quad (\text{A.6})$$

$$\begin{aligned} \mathcal{M}_{2E}^{(1)} &= \frac{i\kappa g_s^2}{2} [T_c]_{nm} [T_c]_{ij} \frac{1}{q^2 q'^2} \epsilon^{\alpha\beta} (P_3)^* \left[ q \cdot q' C_{\alpha\beta,\rho\sigma} + D_{\alpha\beta,\rho\sigma}(q, q') \right] \\ &\times \bar{v}_n(k_2) \gamma^\rho u_m(k_1) \\ &\times \bar{u}_i(P_1) \gamma^\sigma v_j(P_2) \end{aligned} \quad (\text{A.7})$$

$$\begin{aligned} \mathcal{M}_{2F}^{(1)} &= -\frac{i\kappa g_s^2}{4} [T_c]_{nm} [T_c]_{ij} \frac{1}{q'^2} \epsilon^{\alpha\beta} (P_3)^* \left[ C_{\alpha\beta,\rho\sigma} - \eta_{\alpha\beta} \eta_{\rho\sigma} \right] \\ &\times \bar{v}_n(k_2) \gamma^\sigma u_m(k_1) \\ &\times \bar{u}_i(P_1) \gamma^\rho v_j(P_2) \end{aligned} \quad (\text{A.8})$$

$$\begin{aligned} \mathcal{M}_{2G}^{(1)} &= -\frac{i\kappa g_s^2}{4} [T_c]_{nm} [T_c]_{ij} \frac{1}{q^2} \epsilon^{\alpha\beta} (P_3)^* \left[ C_{\alpha\beta,\rho\sigma} - \eta_{\alpha\beta} \eta_{\rho\sigma} \right] \\ &\times \bar{v}_n(k_2) \gamma^\rho u_m(k_1) \\ &\times \bar{u}_i(P_1) \gamma^\sigma v_j(P_2) \end{aligned} \quad (\text{A.9})$$

For gluon-initiated processes :

$$\begin{aligned}
\mathcal{M}_{2A}^{(2)} = & -\frac{\kappa g_s^2}{2} f^{abc} [T_c]_{ij} \frac{1}{(k_1 - P_3)^2 q'^2} \epsilon_a^\mu(k_1) \epsilon_b^\nu(k_2) \epsilon^{\alpha\beta}(P_3)^* \eta^{\rho\sigma} \\
& \times \left[ k_1 \cdot (P_3 - k_1) C_{\alpha\beta,\mu\lambda} + D_{\alpha\beta,\mu\lambda}(k_1, P_3 - k_1) \right] \\
& \times \left[ \eta_{\lambda\nu} (k_1 - P_3 - k_2)_\rho + \eta_{\nu\rho} (k_2 + q')_\lambda + \eta_{\rho\lambda} (-q' - k_1 + P_3)_\nu \right] \\
& \times \bar{u}_i(P_1) \gamma_\sigma v_j(P_2)
\end{aligned} \tag{A.10}$$

$$\begin{aligned}
\mathcal{M}_{2B}^{(2)} = & -\frac{\kappa g_s^2}{2} f^{abc} [T_c]_{ij} \frac{1}{(k_2 - P_3)^2 q'^2} \epsilon_a^\mu(k_1) \epsilon_b^\nu(k_2) \epsilon^{\alpha\beta}(P_3)^* \eta^{\rho\sigma} \\
& \times \left[ k_2 \cdot (P_3 - k_2) C_{\alpha\beta,\nu\lambda} + D_{\alpha\beta,\nu\lambda}(k_2, P_3 - k_2) \right] \\
& \times \left[ \eta_{\lambda\rho} (k_2 - P_3 + q')_\mu + \eta_{\rho\mu} (-q' - k_1)_\lambda + \eta_{\mu\lambda} (k_1 - k_2 + P_3)_\rho \right] \\
& \times \bar{u}_i(P_1) \gamma_\sigma v_j(P_2)
\end{aligned} \tag{A.11}$$

$$\begin{aligned}
\mathcal{M}_{2C}^{(2)} = & \frac{\kappa g_s^2}{8} f^{abc} [T_c]_{ij} \frac{1}{[(P_1 + P_3)^2 - m_t^2] q^2} \epsilon_a^\mu(k_1) \epsilon_b^\nu(k_2) \epsilon^{\alpha\beta}(P_3)^* \eta^{\rho\sigma} \\
& \times \left[ \eta_{\mu\nu} (k_1 - k_2)_\rho + \eta_{\nu\rho} (k_2 + q)_\mu + \eta_{\rho\mu} (-q - k_1)_\nu \right] \\
& \times \bar{u}_i(P_1) \left[ \gamma_\alpha(2P_1 + P_3)_\beta + \gamma_\beta(2P_1 + P_3)_\alpha \right] (\not{P}_1 + \not{P}_3 + m_t) \gamma_\sigma v_j(P_2)
\end{aligned} \tag{A.12}$$

$$\begin{aligned}
\mathcal{M}_{2D}^{(2)} = & \frac{\kappa g_s^2}{8} f^{abc} [T_c]_{ij} \frac{1}{[(P_2 + P_3)^2 - m_t^2] q^2} \epsilon_a^\mu(k_1) \epsilon_b^\nu(k_2) \epsilon^{\alpha\beta}(P_3)^* \eta^{\rho\sigma} \\
& \times \left[ \eta_{\mu\nu} (k_1 - k_2)_\rho + \eta_{\nu\rho} (k_2 + q)_\mu + \eta_{\rho\mu} (-q - k_1)_\nu \right] \\
& \times \bar{u}_i(P_1) (\not{P}_2 + \not{P}_3 - m_t) \left[ \gamma_\alpha(2P_2 + P_3)_\beta + \gamma_\beta(2P_2 + P_3)_\alpha \right] \gamma_\sigma v_j(P_2)
\end{aligned} \tag{A.13}$$

$$\begin{aligned}
\mathcal{M}_{2E}^{(2)} = & -\frac{\kappa g_s^2}{2} f^{abc} [T_c]_{ij} \frac{1}{q^2 q'^2} \epsilon_a^\mu(k_1) \epsilon_b^\nu(k_2) \epsilon^{\alpha\beta}(P_3)^* \\
& \times \left[ \eta_{\mu\nu} (k_1 - k_2)_\rho + \eta_{\nu\rho} (k_2 + q)_\mu + \eta_{\rho\mu} (-q - k_1)_\nu \right] \\
& \times \left[ -q \cdot q' C_{\alpha\beta,\rho\sigma} + D_{\alpha\beta,\rho\sigma}(q, -q') \right] \\
& \times \bar{u}_i(P_1) \gamma^\sigma v_j(P_2)
\end{aligned} \tag{A.14}$$

$$\begin{aligned}
\mathcal{M}_{2F}^{(2)} = & -\frac{\kappa g_s^2}{2} f^{abc} [T_c]_{ij} \frac{1}{q'^2} \epsilon_a^\mu(k_1) \epsilon_b^\nu(k_2) \epsilon^{\alpha\beta}(P_3)^* \eta^{\rho\sigma} \\
& \times \left[ C_{\alpha\beta,\mu\nu} (k_1 - k_2)_\rho + C_{\alpha\beta,\nu\rho} (k_2 + q')_\mu + C_{\alpha\beta,\rho\mu} (-q' - k_1)_\nu + F_{\alpha\beta,\rho\nu\mu}(-q', k_2, k_1) \right] \\
& \times \left[ -q \cdot q' C_{\alpha\beta,\rho\sigma} + D_{\alpha\beta,\rho\sigma}(q, -q') \right] \\
& \times \bar{u}_i(P_1) \gamma_\sigma v_j(P_2)
\end{aligned} \tag{A.15}$$

$$\begin{aligned}
\mathcal{M}_{2G}^{(2)} = & -\frac{\kappa g_s^2}{4} f^{abc} [T_c]_{ij} \frac{1}{q^2} \epsilon_a^\mu(k_1) \epsilon_b^\nu(k_2) \epsilon^{\alpha\beta}(P_3)^* \eta^{\rho\sigma} (C_{\alpha\beta,\sigma\lambda} - \eta_{\alpha\beta} \eta_{\sigma\lambda}) \\
& \times \left[ \eta_{\mu\nu} (k_1 - k_2)_\rho + \eta_{\nu\rho} (k_2 + q)_\mu + \eta_{\rho\mu} (-q - k_1)_\nu \right] \\
& \times \bar{u}_i(P_1) \gamma^\lambda v_j(P_2)
\end{aligned} \tag{A.16}$$

$$\begin{aligned}
\mathcal{M}_{2A}^{(3)} &= \frac{i \kappa g_s^2}{2} [T_a T_b]_{ij} \frac{1}{(k_1 - P_3)^2 [(k_2 - P_2)^2 - m_t^2]} \epsilon_a^\mu(k_1) \epsilon_b^\nu(k_2) \epsilon^{\alpha\beta}(P_3)^* \\
&\times \left[ k_1 \cdot (P_3 - k_1) C_{\alpha\beta,\mu\lambda} + D_{\alpha\beta,\mu\lambda}(k_1, P_3 - k_1) \right] \\
&\times \bar{u}_i(P_1) \gamma^\lambda (\not{k}_2 - \not{P}_2 + m_t) \gamma_\nu v_j(P_2)
\end{aligned} \tag{A.17}$$

$$\begin{aligned}
\mathcal{M}_{2B}^{(3)} &= \frac{i \kappa g_s^2}{2} [T_a T_b]_{ij} \frac{1}{(k_2 - P_3)^2 [(k_1 - P_1)^2 - m_t^2]} \epsilon_a^\mu(k_1) \epsilon_b^\nu(k_2) \epsilon^{\alpha\beta}(P_3)^* \\
&\times \left[ k_2 \cdot (P_3 - k_2) C_{\alpha\beta,\nu\lambda} + D_{\alpha\beta,\nu\lambda}(k_2, P_3 - k_2) \right] \\
&\times \bar{u}_i(P_1) \gamma_\mu (\not{P}_1 - \not{k}_1 + m_t) \gamma^\lambda v_j(P_2)
\end{aligned} \tag{A.18}$$

$$\begin{aligned}
\mathcal{M}_{2C}^{(3)} &= -\frac{i \kappa g_s^2}{8} [T_a T_b]_{ij} \frac{1}{[(P_1 + P_3)^2 - m_t^2] [(k_2 - P_2)^2 - m_t^2]} \epsilon_a^\mu(k_1) \epsilon_b^\nu(k_2) \epsilon^{\alpha\beta}(P_3)^* \\
&\times \bar{u}_i(P_1) \left[ \gamma_\alpha (2P_1 + P_3)_\beta + \gamma_\beta (2P_1 + P_3)_\alpha \right] \\
&\times (\not{P}_1 + \not{P}_3 + m_t) \gamma_\mu (\not{k}_2 - \not{P}_2 + m_t) \gamma_\nu v_j(P_2)
\end{aligned} \tag{A.19}$$

$$\begin{aligned}
\mathcal{M}_{2D}^{(3)} &= -\frac{i \kappa g_s^2}{8} [T_a T_b]_{ij} \frac{1}{[(P_2 + P_3)^2 - m_t^2] [(k_1 - P_1)^2 - m_t^2]} \epsilon_a^\mu(k_1) \epsilon_b^\nu(k_2) \epsilon^{\alpha\beta}(P_3)^* \\
&\times \bar{u}_i(P_1) \gamma_\mu (\not{P}_1 - \not{k}_1 + m_t) \gamma_\nu (\not{P}_2 + \not{P}_3 - m_t) \\
&\times \left[ \gamma_\alpha (2P_2 + P_3)_\beta + \gamma_\beta (2P_2 + P_3)_\alpha \right] v_j(P_2)
\end{aligned} \tag{A.20}$$

$$\begin{aligned}
\mathcal{M}_{2E}^{(3)} &= -\frac{i \kappa g_s^2}{8} [T_a T_b]_{ij} \frac{1}{[(P_1 - k_1)^2 - m_t^2] [(k_2 - P_2)^2 - m_t^2]} \epsilon_a^\mu(k_1) \epsilon_b^\nu(k_2) \epsilon^{\alpha\beta}(P_3)^* \\
&\times \bar{u}_i(P_1) \gamma_\mu (\not{P}_1 - \not{k}_1 + m_t) \left[ \gamma_\alpha (2P_1 - 2k_1 + P_3)_\beta + \gamma_\beta (2P_1 - 2k_1 + P_3)_\alpha \right] \\
&(\not{k}_2 - \not{P}_2 + m_t) \gamma_\nu v_j(P_2)
\end{aligned} \tag{A.21}$$

$$\begin{aligned}
\mathcal{M}_{2F}^{(3)} &= \frac{i \kappa g_s^2}{4} [T_a T_b]_{ij} \frac{1}{[(k_2 - P_2)^2 - m_t^2]} \epsilon_a^\mu(k_1) \epsilon_b^\nu(k_2) \epsilon^{\alpha\beta}(P_3)^* \\
&\times (C_{\alpha\beta,\mu\rho} - \eta_{\alpha\beta} \eta_{\mu\rho}) \\
&\times \bar{u}_i(P_1) \gamma^\rho (\not{k}_2 - \not{P}_2 + m_t) \gamma_\nu v_j(P_2)
\end{aligned} \tag{A.22}$$

$$\begin{aligned}
\mathcal{M}_{2G}^{(3)} &= \frac{i \kappa g_s^2}{4} [T_a T_b]_{ij} \frac{1}{[(P_1 - k_1)^2 - m_t^2]} \epsilon_a^\mu(k_1) \epsilon_b^\nu(k_2) \epsilon^{\alpha\beta}(P_3)^* \\
&\times (C_{\alpha\beta,\nu\rho} - \eta_{\alpha\beta} \eta_{\nu\rho}) \\
&\times \bar{u}_i(P_1) \gamma_\mu (\not{P}_1 - \not{k}_1 + m_t) \gamma^\rho v_j(P_2)
\end{aligned} \tag{A.23}$$

$$\begin{aligned}
\mathcal{M}_{2A}^{(4)} &= \frac{i \kappa g_s^2}{2} [T_b T_a]_{ij} \frac{1}{(k_1 - P_3)^2 [(P_1 - k_2)^2 - m_t^2]} \epsilon_a^\mu(k_1) \epsilon_b^\nu(k_2) \epsilon^{\alpha\beta}(P_3)^* \\
&\times \left[ k_1 \cdot (P_3 - k_1) C_{\alpha\beta,\mu\lambda} + D_{\alpha\beta,\mu\lambda}(k_1, P_3 - k_1) \right] \\
&\times \bar{u}_i(P_1) \gamma_\nu (\not{P}_1 - \not{k}_2 + m_t) \gamma^\lambda v_j(P_2)
\end{aligned} \tag{A.24}$$

$$\begin{aligned}
\mathcal{M}_{2B}^{(4)} &= \frac{i \kappa g_s^2}{2} [T_b T_a]_{ij} \frac{1}{(k_2 - P_3)^2 [(k_1 - P_2)^2 - m_t^2]} \epsilon_a^\mu(k_1) \epsilon_b^\nu(k_2) \epsilon^{\alpha\beta}(P_3)^* \\
&\times \left[ k_2 \cdot (P_3 - k_2) C_{\alpha\beta,\nu\lambda} + D_{\alpha\beta,\nu\lambda}(k_2, P_3 - k_2) \right] \\
&\times \bar{u}_i(P_1) \gamma^\lambda (\not{k}_1 - \not{P}_2 + m_t) \gamma_\mu v_j(P_2)
\end{aligned} \tag{A.25}$$

$$\begin{aligned}
\mathcal{M}_{2C}^{(4)} &= -\frac{i \kappa g_s^2}{8} [T_b T_a]_{ij} \frac{1}{[(P_1 + P_3)^2 - m_t^2][(k_1 - P_2)^2 - m_t^2]} \epsilon_a^\mu(k_1) \epsilon_b^\nu(k_2) \epsilon^{\alpha\beta}(P_3)^* \\
&\times \bar{u}_i(P_1) \left[ \gamma_\alpha(2P_1 + P_3)_\beta + \gamma_\beta(2P_1 + P_3)_\alpha \right] \\
&\times (\not{P}_1 + \not{P}_3 + m_t) \gamma_\nu (\not{k}_1 - \not{P}_2 + m_t) \gamma_\mu v_j(P_2)
\end{aligned} \tag{A.26}$$

$$\begin{aligned}
\mathcal{M}_{2D}^{(4)} &= -\frac{i \kappa g_s^2}{8} [T_b T_a]_{ij} \frac{1}{[(P_2 + P_3)^2 - m_t^2][(k_2 - P_1)^2 - m_t^2]} \epsilon_a^\mu(k_1) \epsilon_b^\nu(k_2) \epsilon^{\alpha\beta}(P_3)^* \\
&\times \bar{u}_i(P_1) \gamma_\nu (\not{P}_1 - \not{k}_2 + m_t) \gamma_\mu (\not{P}_2 + \not{P}_3 - m_t) \\
&\times \left[ \gamma_\alpha(2P_2 + P_3)_\beta + \gamma_\beta(2P_2 + P_3)_\alpha \right] v_j(P_2)
\end{aligned} \tag{A.27}$$

$$\begin{aligned}
\mathcal{M}_{2E}^{(4)} &= -\frac{i \kappa g_s^2}{8} [T_b T_a]_{ij} \frac{1}{[(P_1 - k_2)^2 - m_t^2][(k_1 - P_2)^2 - m_t^2]} \epsilon_a^\mu(k_1) \epsilon_b^\nu(k_2) \epsilon^{\alpha\beta}(P_3)^* \\
&\times \bar{u}_i(P_1) \gamma_\nu (\not{P}_1 - \not{k}_2 + m_t) \left[ \gamma_\alpha(2P_1 - 2k_2 + P_3)_\beta + \gamma_\beta(2P_1 - 2k_2 + P_3)_\alpha \right] \\
&\times (\not{k}_1 - \not{P}_2 + m_t) \gamma_\mu v_j(P_2)
\end{aligned} \tag{A.28}$$

$$\begin{aligned}
\mathcal{M}_{2F}^{(4)} &= \frac{i \kappa g_s^2}{4} [T_b T_a]_{ij} \frac{1}{[(P_1 - k_2)^2 - m_t^2]} \epsilon_a^\mu(k_1) \epsilon_b^\nu(k_2) \epsilon^{\alpha\beta}(P_3)^* \\
&\times (C_{\alpha\beta,\mu\rho} - \eta_{\alpha\beta} \eta_{\mu\rho}) \\
&\times \bar{u}_i(P_1) \gamma_\nu (\not{P}_1 - \not{k}_2 + m_t) \gamma^\rho v_j(P_2)
\end{aligned} \tag{A.29}$$

$$\begin{aligned}
\mathcal{M}_{2G}^{(4)} &= \frac{i \kappa g_s^2}{4} [T_b T_a]_{ij} \frac{1}{[(k_1 - P_2)^2 - m_t^2]} \epsilon_a^\mu(k_1) \epsilon_b^\nu(k_2) \epsilon^{\alpha\beta}(P_3)^* \\
&\times (C_{\alpha\beta,\nu\rho} - \eta_{\alpha\beta} \eta_{\nu\rho}) \\
&\times \bar{u}_i(P_1) \gamma^\rho (\not{k}_1 - \not{P}_2 + m_t) \gamma_\mu v_j(P_2)
\end{aligned} \tag{A.30}$$

where  $q = k_1 + k_2$  and  $q' = P_1 + P_2$  and the graviton couplings include the tensors

$$C^{\mu\nu,\alpha\beta} = \eta^{\mu\alpha} \eta^{\nu\beta} + \eta^{\mu\beta} \eta^{\nu\alpha} - \eta^{\mu\nu} \eta^{\alpha\beta} \tag{A.31}$$

$$D^{\mu\nu,\alpha\beta}(k_1, k_2) = \eta^{\mu\nu} k_1^\beta k_2^\alpha - \left\{ \left( \eta^{\mu\beta} k_1^\nu k_2^\alpha + \eta^{\mu\alpha} k_1^\beta k_2^\nu - \eta^{\alpha\beta} k_1^\mu k_2^\nu \right) + (\mu \leftrightarrow \nu) \right\} \tag{A.32}$$

$$F^{\mu\nu,\alpha\beta\gamma}(k_1, k_2, k_3) = \eta^{\mu\alpha} \eta^{\beta\gamma} (k_2 - k_3)_\nu + \eta^{\mu\beta} \eta^{\alpha\gamma} (k_3 - k_1)_\nu \tag{A.33}$$

$$+ \eta^{\mu\gamma} \eta^{\alpha\beta} (k_3 - k_1)_\nu + (\mu \leftrightarrow \nu) \tag{A.34}$$

Finally, the sum over graviton polarisations will be

$$P^{\mu\nu,\alpha\beta}(p_3) = \Pi^{\mu\alpha} \Pi^{\nu\beta} + \Pi^{\mu\beta} \Pi^{\nu\alpha} - \frac{2}{3} \Pi^{\mu\nu} \Pi^{\alpha\beta} \tag{A.35}$$

where  $\Pi^{\mu\nu} = \eta^{\mu\nu} - p_3^\mu p_3^\nu / M_{\tilde{n}}^2$ .

## A.2 Radiated Z boson :

$$\mathbf{P}(\mathbf{k}_1) + \mathbf{P}(\mathbf{k}_2) \rightarrow \mathbf{t}(\mathbf{P}_1) + \bar{\mathbf{t}}(\mathbf{P}_2) + \mathbf{Z}_\alpha^{(\tilde{n})}(\mathbf{P}_3)$$

where, for quark-initiated processes,

$$\mathcal{M}_1 = \left( \mathcal{M}_{2A}^{(1)} + \mathcal{M}_{2B}^{(1)} + \mathcal{M}_{2C}^{(1)} + \mathcal{M}_{2D}^{(1)} \right) \tag{A.36}$$

and for gluon-initiated processes,

$$\mathcal{M}_2 = \left( \mathcal{M}_{2A}^{(2)} + \mathcal{M}_{2B}^{(2)} + \mathcal{M}_{2A}^{(1)} + \mathcal{M}_{2B}^{(1)} + \mathcal{M}_{2C}^{(1)} + \mathcal{M}_{2A}^{(1)} + \mathcal{M}_{2B}^{(1)} + \mathcal{M}_{2C}^{(1)} \right) \quad (\text{A.37})$$

where the indices  $A$  to  $D$  refer to the diagrams in Figure A.2. The label should be read only one of the  $A$  upto  $D$ . The individual terms are listed below.

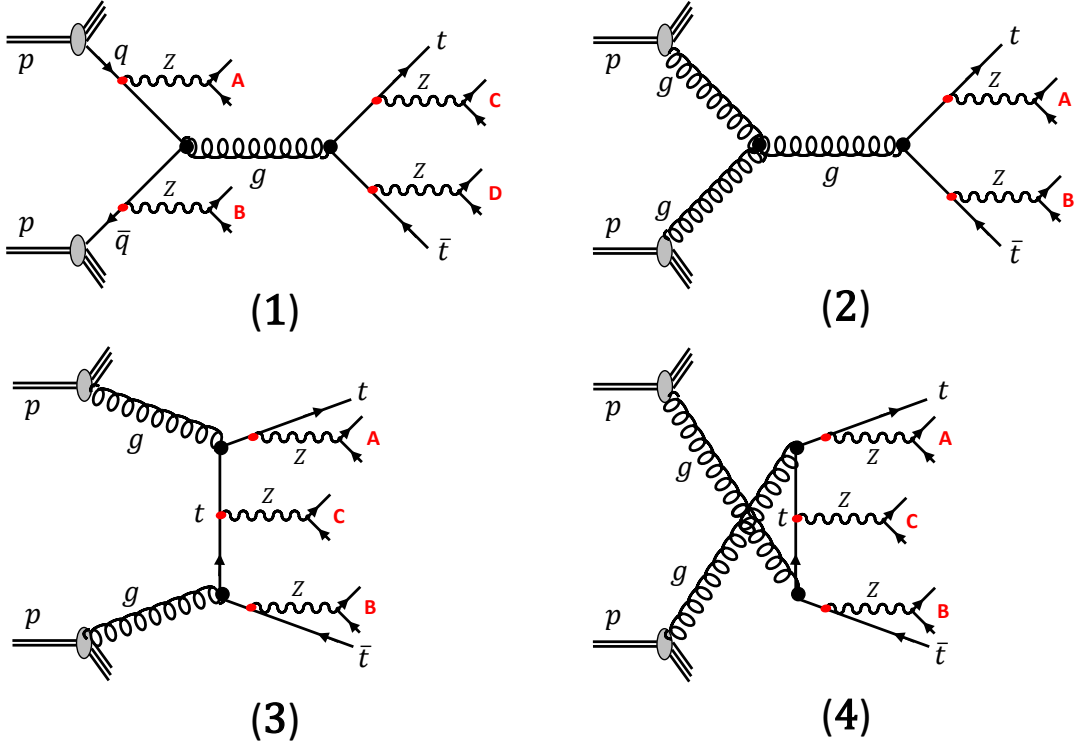


Figure A.2: Figure shows diagrams of the signal and background processes at the LHC.

**For quark-initiated processes :**

$$\begin{aligned} \mathcal{M}_{1A}^{(1)} &= ig g_s^2 [T_c]_{nm} [T_c]_{ij} \frac{1}{q^2 (k_1 - P_3)^2} \epsilon^\alpha(P_3)^* \\ &\times \bar{v}_n(k_2) \gamma_\rho (\not{k}_1 - \not{P}_3) \gamma_\alpha (A_q + B_q \gamma_5) u_m(k_1) \\ &\times \bar{u}_i(P_1) \gamma^\rho v_j(P_2) \end{aligned} \quad (\text{A.38})$$

$$\begin{aligned} \mathcal{M}_{1B}^{(1)} &= ig g_s^2 [T_c]_{nm} [T_c]_{ij} \frac{1}{q^2 (k_2 - P_3)^2} \epsilon^\alpha(P_3)^* \\ &\times \bar{v}_n(k_2) \gamma_\alpha (A_q + B_q \gamma_5) (\not{P}_3 - \not{k}_2) \gamma_\rho u_m(k_1) \\ &\times \bar{u}_i(P_1) \gamma^\rho v_j(P_2) \end{aligned} \quad (\text{A.39})$$

$$\begin{aligned} \mathcal{M}_{1C}^{(1)} &= ig g_s^2 [T_c]_{nm} [T_c]_{ij} \frac{1}{q^2 [(P_1 + P_3)^2 - m_t^2]} \epsilon^\alpha(P_3)^* \\ &\times \bar{v}_n(k_2) \gamma_\rho u_m(k_1) \\ &\times \bar{u}_i(P_1) \gamma_\alpha (A_t + B_t \gamma_5) (\not{P}_1 + \not{P}_3 + m_t) \gamma^\rho v_j(P_2) \end{aligned} \quad (\text{A.40})$$

$$\begin{aligned}
\mathcal{M}_{1D}^{(1)} &= ig g_s^2 [T_c]_{nm} [T_c]_{ij} \frac{1}{q^2 [(P_2 + P_3)^2 - m_t^2]} \epsilon^\alpha(P_3)^* \\
&\quad \times \bar{v}_n(k_2) \gamma_\rho u_m(k_1) \\
&\quad \times \bar{u}_i(P_1) \gamma^\rho (-\not{P}_1 - \not{P}_3 + m_t) \gamma_\alpha (A_t + B_t \gamma_5) v_j(P_2)
\end{aligned} \tag{A.41}$$

For gluon-initiated processes :

$$\begin{aligned}
\mathcal{M}_{1A}^{(2)} &= g g_s^2 f^{abc} [T_c]_{ij} \frac{1}{q^2 [(P_1 + P_3)^2 - m_t^2]} \epsilon_a^\mu(k_1) \epsilon_b^\nu(k_2) \epsilon^\alpha(P_3)^* \\
&\quad \times \left[ \eta_{\mu\nu} (k_1 - k_2)_\rho + \eta_{\nu\rho} (k_2 + q)_\mu + \eta_{\rho\mu} (-q - k_1)_\nu \right] \\
&\quad \times \bar{u}_i(P_1) \gamma_\alpha (A_t + B_t \gamma_5) (\not{P}_1 + \not{P}_3 + m_t) \gamma^\rho v_j(P_2)
\end{aligned} \tag{A.42}$$

$$\begin{aligned}
\mathcal{M}_{1B}^{(2)} &= -g g_s^2 f^{abc} [T_c]_{ij} \frac{1}{q^2 [(P_2 + P_3)^2 - m_t^2]} \epsilon_a^\mu(k_1) \epsilon_b^\nu(k_2) \epsilon^\alpha(P_3)^* \\
&\quad \times \left[ \eta_{\mu\nu} (k_1 - k_2)_\rho + \eta_{\nu\rho} (k_2 + q)_\mu + \eta_{\rho\mu} (-q - k_1)_\nu \right] \\
&\quad \times \bar{u}_i(P_1) \gamma^\rho (\not{P}_2 + \not{P}_3 + m_t) \gamma_\alpha (A_t + B_t \gamma_5) v_j(P_2)
\end{aligned} \tag{A.43}$$

$$\begin{aligned}
\mathcal{M}_{1A}^{(3)} &= -ig g_s^2 [T_a T_b]_{ij} \frac{1}{[(P_1 + P_3)^2 - m_t^2] [(k_2 - P_2)^2 - m_t^2]} \epsilon_a^\mu(k_1) \epsilon_b^\nu(k_2) \epsilon^\alpha(P_3)^* \\
&\quad \times \bar{u}_i(P_1) \gamma_\alpha (A_t + B_t \gamma_5) (\not{P}_1 + \not{P}_3 + m_t) \gamma_\mu (\not{k}_2 - \not{P}_2 + m_t) \gamma_\nu v_j(P_2)
\end{aligned} \tag{A.44}$$

$$\begin{aligned}
\mathcal{M}_{1B}^{(3)} &= -ig g_s^2 [T_a T_b]_{ij} \frac{1}{[(P_2 + P_3)^2 - m_t^2] [(k_1 - P_1)^2 - m_t^2]} \epsilon_a^\mu(k_1) \epsilon_b^\nu(k_2) \epsilon^\alpha(P_3)^* \\
&\quad \times \bar{u}_i(P_1) \gamma_\mu (\not{k}_1 - \not{P}_1 - m_t) \gamma_\nu (\not{P}_2 + \not{P}_3 - m_t) \gamma_\alpha (A_t + B_t \gamma_5) v_j(P_2)
\end{aligned} \tag{A.45}$$

$$\begin{aligned}
\mathcal{M}_{1C}^{(3)} &= -ig g_s^2 [T_a T_b]_{ij} \frac{1}{[(k_2 - P_2)^2 - m_t^2] [(k_1 - P_1)^2 - m_t^2]} \epsilon_a^\mu(k_1) \epsilon_b^\nu(k_2) \epsilon^\alpha(P_3)^* \\
&\quad \times \bar{u}_i(P_1) \gamma_\mu (\not{P}_1 - \not{k}_1 + m_t) \gamma_\alpha (A_t + B_t \gamma_5) (\not{k}_2 - \not{P}_2 + m_t) \gamma_\nu v_j(P_2)
\end{aligned} \tag{A.46}$$

$$\begin{aligned}
\mathcal{M}_{1A}^{(4)} &= -ig g_s^2 [T_b T_a]_{ij} \frac{1}{[(P_1 + P_3)^2 - m_t^2] [(k_1 - P_2)^2 - m_t^2]} \epsilon_a^\mu(k_1) \epsilon_b^\nu(k_2) \epsilon^\alpha(P_3)^* \\
&\quad \times \bar{u}_i(P_1) \gamma_\alpha (A_t + B_t \gamma_5) (\not{P}_1 + \not{P}_3 + m_t) \gamma_\nu (\not{k}_1 - \not{P}_2 + m_t) \gamma_\mu v_j(P_2)
\end{aligned} \tag{A.47}$$

$$\begin{aligned}
\mathcal{M}_{1B}^{(4)} &= -ig g_s^2 [T_b T_a]_{ij} \frac{1}{[(P_2 + P_3)^2 - m_t^2] [(k_2 - P_1)^2 - m_t^2]} \epsilon_a^\mu(k_1) \epsilon_b^\nu(k_2) \epsilon^\alpha(P_3)^* \\
&\quad \times \bar{u}_i(P_1) \gamma_\nu (\not{k}_2 - \not{P}_1 - m_t) \gamma_\mu (\not{P}_2 + \not{P}_3 - m_t) \gamma_\alpha (A_t + B_t \gamma_5) v_j(P_2)
\end{aligned} \tag{A.48}$$

$$\begin{aligned}
\mathcal{M}_{1C}^{(4)} &= -ig g_s^2 [T_b T_a]_{ij} \frac{1}{[(k_1 - P_2)^2 - m_t^2] [(k_2 - P_1)^2 - m_t^2]} \epsilon_a^\mu(k_1) \epsilon_b^\nu(k_2) \epsilon^\alpha(P_3)^* \\
&\quad \times \bar{u}_i(P_1) \gamma_\nu (\not{P}_1 - \not{k}_2 + m_t) \gamma_\alpha (A_t + B_t \gamma_5) (\not{k}_1 - \not{P}_2 + m_t) \gamma_\mu v_j(P_2)
\end{aligned} \tag{A.49}$$

where the gauge boson couplings are the SM ones, as shown below.

$q =$	$A_q$	$B_q$
$u, c, t$	$-\frac{1 - \frac{8}{3} \sin^2 \theta_W}{4 \cos \theta_W}$	$\frac{1}{4 \cos \theta_W}$
$d, s, b$	$\frac{1 - \frac{4}{3} \sin^2 \theta_W}{4 \cos \theta_W}$	$-\frac{1}{4 \cos \theta_W}$

## APPENDIX B

---

# Amplitudes for LED Signals at $e^+e^-$ Colliders

---

### B.1 Radiated tensor graviton KK modes:

$$e^-(\mathbf{p}_1) + e^+(\mathbf{p}_2) \rightarrow h_{\mu\nu}^{(\tilde{n})}(\mathbf{p}_3) + \mathbf{t}(\mathbf{p}_4) + \bar{\mathbf{t}}(\mathbf{p}_5)$$

where

$$\mathcal{M}_2 = \sum_{V=\gamma,Z} \left( \mathcal{M}_{2a}^{(V)} + \mathcal{M}_{2b}^{(V)} + \mathcal{M}_{2c}^{(V)} + \mathcal{M}_{2d}^{(V)} + \mathcal{M}_{2e}^{(V)} + \mathcal{M}_{2f}^{(V)} + \mathcal{M}_{2g}^{(V)} \right) \quad (\text{B.1})$$

where the indices  $a$  to  $g$  refer to the diagrams in Figure 6.1. The individual terms are listed below.

$$\begin{aligned} \mathcal{M}_{2a}^{(V)} &= \bar{v}_e(p_2) (-ig) \gamma^\lambda \left( A_e^{(V)} + B_e^{(V)} \gamma_5 \right) \frac{i}{\not{p}_1 - \not{p}_3} \left( \frac{-i\kappa}{8} \right) \{ (2p_1 - p_3)^\mu \gamma^\nu + (2p_1 - p_3)^\nu \gamma^\mu \} u_e(p_1) \\ &\times \frac{-i\eta_{\lambda\rho}}{(p_4 + p_5)^2 - M_V^2 + iM_V\Gamma_V} \bar{u}_t(p_4) (-ig) \gamma^\rho \left( A_t^{(V)} + B_t^{(V)} \gamma_5 \right) v_t(p_5) \varepsilon_{\mu\nu}^{(\tilde{n})}(p_3)^* \end{aligned} \quad (\text{B.2})$$

$$\begin{aligned} \mathcal{M}_{2b}^{(V)} &= \bar{v}_e(p_2) \left( \frac{-i\kappa}{8} \right) \{ (-2p_2 + p_3)^\mu \gamma^\nu + (-2p_2 + p_3)^\nu \gamma^\mu \} \frac{-i}{\not{p}_2 - \not{p}_3} (-ig) \gamma^\lambda \left( A_e^{(V)} + B_e^{(V)} \gamma_5 \right) u_e(p_1) \\ &\times \frac{-i\eta_{\lambda\rho}}{(p_4 + p_5)^2 - M_V^2 + iM_V\Gamma_V} \bar{u}_t(p_4) (-ig) \gamma^\rho \left( A_t^{(V)} + B_t^{(V)} \gamma_5 \right) v_t(p_5) \varepsilon_{\mu\nu}^{(\tilde{n})}(p_3)^* \end{aligned} \quad (\text{B.3})$$

$$\begin{aligned} \mathcal{M}_{2c}^{(V)} &= \bar{u}_t(p_4) \left( \frac{-i\kappa}{8} \right) \{ (p_3 + 2p_4)^\mu \gamma^\nu + (p_3 + 2p_4)^\nu \gamma^\mu \} \frac{i}{\not{p}_3 + \not{p}_4 - m_t} (-ig) \gamma^\rho \left( A_t^{(V)} + B_t^{(V)} \gamma_5 \right) v_t(p_5) \\ &\times \frac{-i\eta_{\lambda\rho}}{(p_1 + p_2)^2 - M_V^2 + iM_V\Gamma_V} \bar{v}_e(p_2) (-ig) \gamma^\lambda \left( A_e^{(V)} + B_e^{(V)} \gamma_5 \right) u_e(p_1) \varepsilon_{\mu\nu}^{(\tilde{n})}(p_3)^* \end{aligned} \quad (\text{B.4})$$

$$\begin{aligned} \mathcal{M}_{2d}^{(V)} &= \bar{u}_t(p_4) (-ig) \gamma^\rho \left( A_t^{(V)} + B_t^{(V)} \gamma_5 \right) \frac{-i}{\not{p}_3 + \not{p}_5 + m_t} \left( \frac{-i\kappa}{8} \right) \{ (-p_3 - 2p_5)^\mu \gamma^\nu + (-p_3 - 2p_5)^\nu \gamma^\mu \} v_t(p_5) \\ &\times \frac{-i\eta_{\lambda\rho}}{(p_1 + p_2)^2 - M_V^2 + iM_V\Gamma_V} \bar{v}_e(p_2) (-ig) \gamma^\lambda \left( A_e^{(V)} + B_e^{(V)} \gamma_5 \right) u_e(p_1) \varepsilon_{\mu\nu}^{(\tilde{n})}(p_3)^* \end{aligned} \quad (\text{B.5})$$

$$\begin{aligned}
\mathcal{M}_{2e}^{(V)} &= \bar{v}_e(p_2) (-ig) \gamma^\lambda \left( A_e^{(V)} + B_e^{(V)} \gamma_5 \right) u_e(p_1) \frac{-i\eta_{\lambda\alpha}}{(p_1 + p_2)^2 - M_V^2 + iM_V \Gamma_V} \\
&\times \left( \frac{-i\kappa}{2} \right) \left[ \{ M_V^2 + (p_1 + p_2) \cdot (-p_4 - p_5) \} C^{\mu\nu,\alpha\beta} + D^{\mu\nu,\alpha\beta}(p_1 + p_2, -p_4 - p_5) \right] \\
&\times \frac{-i\eta_{\beta\rho}}{(p_4 + p_5)^2 - M_V^2 + iM_V \Gamma_V} \bar{u}_t(p_4) (-ig) \gamma^\rho \left( A_t^{(V)} + B_t^{(V)} \gamma_5 \right) v_t(p_5) \varepsilon_{\mu\nu}^{(\vec{n})}(p_3)^* \quad (\text{B.6})
\end{aligned}$$

$$\begin{aligned}
\mathcal{M}_{2f}^{(V)} &= \bar{v}_e(p_2) \left( \frac{ig\kappa}{4} \right) (C^{\mu\nu,\lambda\sigma} - \eta^{\mu\nu} \eta^{\lambda\sigma}) \gamma_\sigma \left( A_e^{(V)} + B_e^{(V)} \gamma_5 \right) u_e(p_1) \\
&\times \frac{-i\eta_{\lambda\rho}}{(p_4 + p_5)^2 - M_V^2 + iM_V \Gamma_V} \bar{u}_t(p_4) (-ig) \gamma^\rho \left( A_t^{(V)} + B_t^{(V)} \gamma_5 \right) v_t(p_5) \varepsilon_{\mu\nu}^{(\vec{n})}(p_3)^* \quad (\text{B.7})
\end{aligned}$$

$$\begin{aligned}
\mathcal{M}_{2g}^{(V)} &= \bar{v}_e(p_2) (-ig) \gamma^\lambda \left( A_e^{(V)} + B_e^{(V)} \gamma_5 \right) u_e(p_1) \frac{-i\eta_{\lambda\rho}}{(p_1 + p_2)^2 - M_V^2 + iM_V \Gamma_V} \\
&\times \bar{u}_t(p_4) \left( \frac{ig\kappa}{4} \right) (C^{\mu\nu,\rho\sigma} - \eta^{\mu\nu} \eta^{\rho\sigma}) \gamma_\sigma \left( A_t^{(V)} + B_t^{(V)} \gamma_5 \right) v_t(p_5) \varepsilon_{\mu\nu}^{(\vec{n})}(p_3)^* \quad (\text{B.8})
\end{aligned}$$

where the gauge boson couplings are the SM ones, as shown below.

$V =$	$M_V$	$\Gamma_V$	$A_e^{(V)}$	$B_e^{(V)}$	$A_t^{(V)}$	$B_t^{(V)}$
$\gamma$	0	0	$\sin \theta_W$	0	$-\frac{2}{3} \sin \theta_W$	0
$Z$	$M_Z$	$\Gamma_Z$	$\frac{1 - 4 \sin^2 \theta_W}{4 \cos \theta_W}$	$-\frac{1}{4 \cos \theta_W}$	$-\frac{1 - \frac{8}{3} \sin^2 \theta_W}{4 \cos \theta_W}$	$\frac{1}{4 \cos \theta_W}$

and the graviton couplings include the tensors

$$C^{\mu\nu,\alpha\beta} = \eta^{\mu\alpha} \eta^{\nu\beta} + \eta^{\mu\beta} \eta^{\nu\alpha} - \eta^{\mu\nu} \eta^{\alpha\beta} \quad (\text{B.9})$$

$$D^{\mu\nu,\alpha\beta}(k, \ell) = \eta^{\mu\nu} k^\beta \ell^\alpha - \left\{ \left( \eta^{\mu\beta} k^\nu \ell^\alpha + \eta^{\mu\alpha} k^\beta \ell^\nu - \eta^{\alpha\beta} k^\mu \ell^\nu \right) + (\mu \leftrightarrow \nu) \right\} \quad (\text{B.10})$$

Finally, the sum over graviton polarisations will be

$$P^{\mu\nu,\alpha\beta}(p_3) = \Pi^{\mu\alpha} \Pi^{\nu\beta} + \Pi^{\mu\beta} \Pi^{\nu\alpha} - \frac{2}{3} \Pi^{\mu\nu} \Pi^{\alpha\beta} \quad (\text{B.11})$$

where  $\Pi^{\mu\nu} = \eta^{\mu\nu} - p_3^\mu p_3^\nu / M_n^2$ .

## B.2 Radiated Z boson:

$$e^-(\mathbf{p}_1) + e^+(\mathbf{p}_2) \rightarrow \mathbf{Z}_\mu(\mathbf{p}_3) + \mathbf{t}(\mathbf{p}_4) + \bar{\mathbf{t}}(\mathbf{p}_5)$$

where

$$\mathcal{M}_1 = \sum_{V=\gamma,Z} \left( \mathcal{M}_{1a}^{(V)} + \mathcal{M}_{1b}^{(V)} + \mathcal{M}_{1c}^{(V)} + \mathcal{M}_{1d}^{(V)} + \mathcal{M}_{1e}^{(V)} \right) \quad (\text{B.12})$$

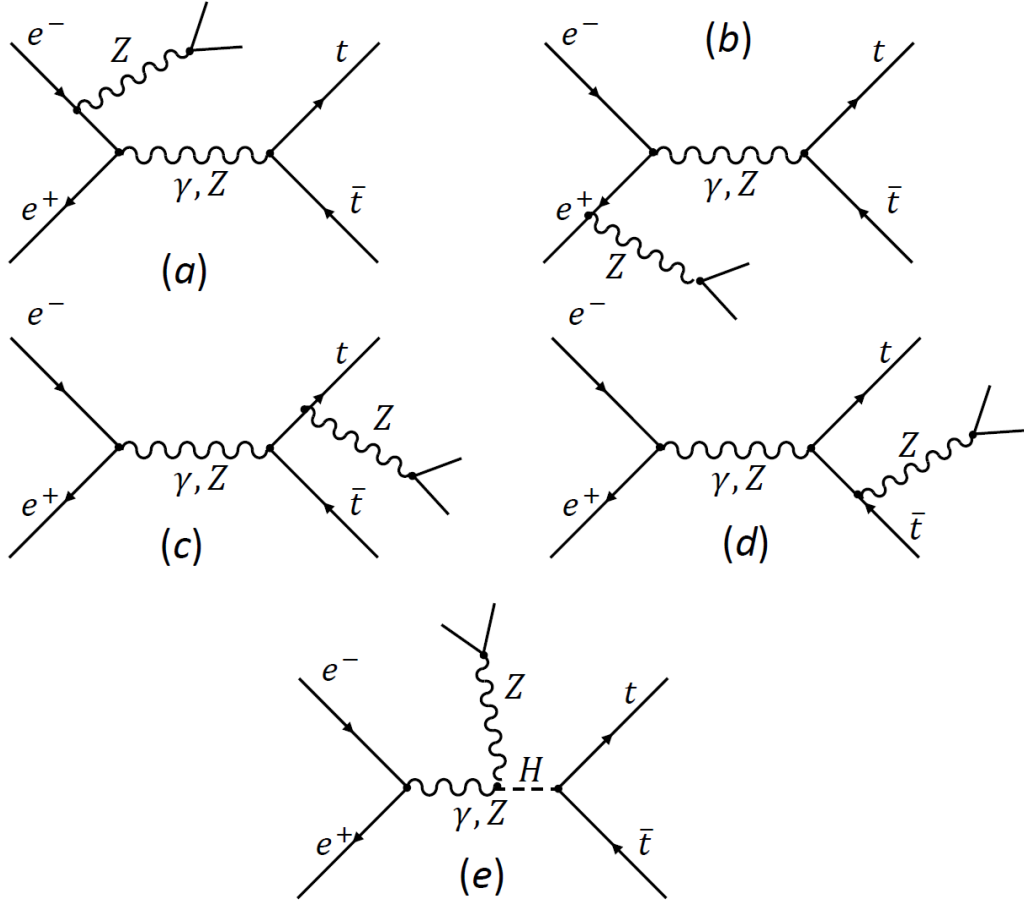


**Figure B.1:** Figure shows diagrams of the  $t\bar{t}Z$  background processes at an  $e^+e^-$  collider.

where

$$\begin{aligned} \mathcal{M}_{1a}^{(V)} &= \bar{v}_e(p_2) (-ig) \gamma^\lambda (A_e^{(V)} + B_e^{(V)} \gamma_5) \frac{i}{\not{p}_1 - \not{p}_3} (-ig) \gamma^\mu (A_e^{(Z)} + B_e^{(Z)} \gamma_5) u_e(p_1) \\ &\quad \times \frac{-i\eta_{\lambda\rho}}{(p_4 + p_5)^2 - M_V^2 + iM_V\Gamma_V} \bar{u}_t(p_4) (-ig) \gamma^\rho (A_t^{(V)} + B_t^{(V)} \gamma_5) v_t(p_5) \varepsilon_\mu(p_3)^* \end{aligned} \quad (\text{B.13})$$

$$\begin{aligned} \mathcal{M}_{1b}^{(V)} &= \bar{v}_e(p_2) (-ig) \gamma^\mu (A_e^{(Z)} + B_e^{(Z)} \gamma_5) \frac{-i}{\not{p}_2 - \not{p}_3} (-ig) \gamma^\lambda (A_e^{(V)} + B_e^{(V)} \gamma_5) u_e(p_1) \\ &\quad \times \frac{-i\eta_{\lambda\rho}}{(p_4 + p_5)^2 - M_V^2 + iM_V\Gamma_V} \bar{u}_t(p_4) (-ig) \gamma^\rho (A_t^{(V)} + B_t^{(V)} \gamma_5) v_t(p_5) \varepsilon_\mu(p_3)^* \end{aligned} \quad (\text{B.14})$$

$$\begin{aligned} \mathcal{M}_{1c}^{(V)} &= \bar{u}_t(p_4) (-ig) \gamma^\mu (A_t^{(Z)} + B_t^{(Z)} \gamma_5) \frac{i}{\not{p}_3 + \not{p}_4 - m_t} (-ig) \gamma^\rho (A_t^{(V)} + B_t^{(V)} \gamma_5) v_t(p_5) \\ &\quad \times \frac{-i\eta_{\lambda\rho}}{(p_1 + p_2)^2 - M_V^2 + iM_V\Gamma_V} \bar{v}_e(p_2) (-ig) \gamma^\lambda (A_e^{(V)} + B_e^{(V)} \gamma_5) u_e(p_1) \varepsilon_\mu(p_3)^* \end{aligned} \quad (\text{B.15})$$

$$\begin{aligned} \mathcal{M}_{1d}^{(V)} &= \bar{u}_t(p_4) (-ig) \gamma^\rho (A_t^{(V)} + B_t^{(V)} \gamma_5) \frac{-i}{\not{p}_3 + \not{p}_5 + m_t} (-ig) \gamma^\mu (A_t^{(Z)} + B_t^{(Z)} \gamma_5) v_t(p_5) \\ &\quad \times \frac{-i\eta_{\lambda\rho}}{(p_1 + p_2)^2 - M_V^2 + iM_V\Gamma_V} \bar{v}_e(p_2) (-ig) \gamma^\lambda (A_e^{(V)} + B_e^{(V)} \gamma_5) u_e(p_1) \varepsilon_\mu(p_3)^* \end{aligned} \quad (\text{B.16})$$

$$\begin{aligned} \mathcal{M}_{1e}^{(V)} &= \bar{v}_e(p_2) (-ig) \gamma^\lambda (A_e^{(V)} + B_e^{(V)} \gamma_5) u_e(p_1) \frac{-i\eta_{\lambda\alpha}}{(p_1 + p_2)^2 - M_V^2 + iM_V\Gamma_V} \delta_{VZ} (ig) \frac{M_Z^2}{M_W} \eta^{\alpha\mu} \\ &\quad \times \frac{i}{(p_4 + p_5)^2 - M_H^2 + iM_H\Gamma_H} \bar{u}_t(p_4) \left( \frac{-ig}{2} \frac{m_t}{M_W} \right) v_t(p_5) \varepsilon_\mu(p_3)^* \end{aligned} \quad (\text{B.17})$$



# Bibliography

---

- [1] G. Nordström, *Relativitätsprinzip und Gravitation*, *Phys. Zeit.* **13** (1912) 1126–1129.
- [2] G. Nordström, *On the possibility of unifying the electromagnetic and the gravitational fields*, *Phys. Z.* **15** (1914) 504–506, [[physics/0702221](#)].
- [3] T. Kaluza, *On the Problem of Unity in Physics*, *Sitzungsber. Preuss. Akad. Wiss. Berlin (Math. Phys.)* **1921** (1921) 966–972.
- [4] O. Klein, *Quantentheorie und fünfdimensionale Relativitätstheorie*, *Zeitschrift für Physik* **37** (Dec, 1926) 895–906.
- [5] S. Raychaudhuri and K. Sridhar, *Particle Physics of Brane Worlds and Extra Dimensions*. Cambridge University Press, 2016.
- [6] N. Arkani-Hamed, S. Dimopoulos, and G. R. Dvali, *The Hierarchy problem and new dimensions at a millimeter*, *Phys. Lett.* **B429** (1998) 263–272, [[hep-ph/9803315](#)].
- [7] I. Antoniadis, N. Arkani-Hamed, S. Dimopoulos, and G. R. Dvali, *New dimensions at a millimeter to a Fermi and superstrings at a TeV*, *Phys. Lett.* **B436** (1998) 257–263, [[hep-ph/9804398](#)].
- [8] L. Randall and R. Sundrum, *A Large mass hierarchy from a small extra dimension*, *Phys. Rev. Lett.* **83** (1999) 3370–3373, [[hep-ph/9905221](#)].
- [9] L. Randall and R. Sundrum, *An Alternative to compactification*, *Phys. Rev. Lett.* **83** (1999) 4690–4693, [[hep-th/9906064](#)].
- [10] **Particle Data Group** Collaboration, C. Patrignani et al., *Review of Particle Physics*, *Chin. Phys.* **C40** (2016), no. 10 100001.
- [11] T. Han, J. D. Lykken, and R.-J. Zhang, *On Kaluza-Klein states from large extra dimensions*, *Phys. Rev.* **D59** (1999) 105006, [[hep-ph/9811350](#)].
- [12] S. Hannestad and G. G. Raffelt, *Stringent neutron star limits on large extra dimensions*, *Phys. Rev. Lett.* **88** (2002) 071301, [[hep-ph/0110067](#)].
- [13] V. D. Barger, T. Han, C. Kao, and R.-J. Zhang, *Astrophysical constraints on large extra dimensions*, *Phys. Lett.* **B461** (1999) 34–42, [[hep-ph/9905474](#)].

- [14] C. Csaki, *TASI lectures on extra dimensions and branes*, in *From fields to strings: Circumnavigating theoretical physics. Ian Kogan memorial collection (3 volume set)*, pp. 605–698, 2004. [hep-ph/0404096](#). [[967\(2004\)](#)].
- [15] T. Gherghetta, *A Holographic View of Beyond the Standard Model Physics*, in *Physics of the large and the small, TASI 09, proceedings of the Theoretical Advanced Study Institute in Elementary Particle Physics, Boulder, Colorado, USA, 1-26 June 2009*, pp. 165–232, 2011. [arXiv:1008.2570](#).
- [16] W. D. Goldberger and M. B. Wise, *Modulus stabilization with bulk fields*, *Phys. Rev. Lett.* **83** (1999) 4922–4925, [[hep-ph/9907447](#)].
- [17] Z. Chacko, R. K. Mishra, and D. Stolarski, *Dynamics of a Stabilized Radion and Duality*, *JHEP* **09** (2013) 121, [[arXiv:1304.1795](#)].
- [18] B. Bellazzini, C. Csaki, J. Hubisz, J. Serra, and J. Terning, *A Higgslike Dilaton*, *Eur. Phys. J.* **C73** (2013), no. 2 2333, [[arXiv:1209.3299](#)].
- [19] Z. Chacko, R. K. Mishra, D. Stolarski, and C. B. Verhaaren, *Interactions of a Stabilized Radion and Duality*, *Phys. Rev.* **D92** (2015), no. 5 056004, [[arXiv:1411.3758](#)].
- [20] D. Elander and M. Piai, *Calculable mass hierarchies and a light dilaton from gravity duals*, *Phys. Lett.* **B772** (2017) 110–114, [[arXiv:1703.09205](#)].
- [21] G. F. Giudice, R. Rattazzi, and J. D. Wells, *Graviscalars from higher dimensional metrics and curvature Higgs mixing*, *Nucl. Phys.* **B595** (2001) 250–276, [[hep-ph/0002178](#)].
- [22] C. Csaki, M. L. Graesser, and G. D. Kribs, *Radion dynamics and electroweak physics*, *Phys. Rev.* **D63** (2001) 065002, [[hep-th/0008151](#)].
- [23] D. Dominici, B. Grzadkowski, J. F. Gunion, and M. Toharia, *The Scalar sector of the Randall-Sundrum model*, *Nucl. Phys.* **B671** (2003) 243–292, [[hep-ph/0206192](#)].
- [24] S. J. Huber and Q. Shafi, *Fermion masses, mixings and proton decay in a Randall-Sundrum model*, *Phys. Lett.* **B498** (2001) 256–262, [[hep-ph/0010195](#)].
- [25] T. Gherghetta and A. Pomarol, *Bulk fields and supersymmetry in a slice of AdS*, *Nucl. Phys.* **B586** (2000) 141–162, [[hep-ph/0003129](#)].
- [26] Y. Grossman and M. Neubert, *Neutrino masses and mixings in nonfactorizable geometry*, *Phys. Lett.* **B474** (2000) 361–371, [[hep-ph/9912408](#)].
- [27] K. Agashe, R. Contino, L. Da Rold, and A. Pomarol, *A Custodial symmetry for  $Zb\bar{b}$* , *Phys. Lett.* **B641** (2006) 62–66, [[hep-ph/0605341](#)].
- [28] A. M. Iyer, K. Sridhar, and S. K. Vempati, *Bulk Randall-Sundrum models, electroweak precision tests, and the 125 GeV Higgs*, *Phys. Rev.* **D93** (2016), no. 7 075008, [[arXiv:1502.06206](#)].
- [29] C. Csaki, J. Hubisz, and S. J. Lee, *Radion phenomenology in realistic warped space models*, *Phys. Rev.* **D76** (2007) 125015, [[arXiv:0705.3844](#)].

- [30] K.-m. Cheung, *Phenomenology of radion in Randall-Sundrum scenario*, *Phys. Rev.* **D63** (2001) 056007, [[hep-ph/0009232](#)].
- [31] M. Chaichian, A. Datta, K. Huitu, and Z.-h. Yu, *Radion and Higgs mixing at the LHC*, *Phys. Lett.* **B524** (2002) 161–169, [[hep-ph/0110035](#)].
- [32] A. Datta and K. Huitu, *Hunting radions at linear colliders*, *Phys. Lett.* **B578** (2004) 376–383, [[hep-ph/0306241](#)].
- [33] P. K. Das, S. K. Rai, and S. Raychaudhuri, *On distinguishing radions from Higgs bosons*, *Phys. Lett.* **B618** (2005) 221–228, [[hep-ph/0410244](#)].
- [34] H. de Sandes and R. Rosenfeld, *Radion-Higgs mixing effects on bounds from LHC Higgs Searches*, *Phys. Rev.* **D85** (2012) 053003, [[arXiv:1111.2006](#)].
- [35] V. Barger, M. Ishida, and W.-Y. Keung, *Differentiating the Higgs boson from the dilaton and the radion at hadron colliders*, *Phys. Rev. Lett.* **108** (2012) 101802, [[arXiv:1111.4473](#)].
- [36] H. Kubota and M. Nojiri, *Radion-higgs mixing state at the LHC with the KK contributions to the production and decay*, *Phys. Rev.* **D87** (2013) 076011, [[arXiv:1207.0621](#)].
- [37] G.-C. Cho, D. Nomura, and Y. Ohno, *Constraints on radion in a warped extra dimension model from Higgs boson searches at the LHC*, *Mod. Phys. Lett.* **A28** (2013) 1350148, [[arXiv:1305.4431](#)].
- [38] N. Desai, U. Maitra, and B. Mukhopadhyaya, *An updated analysis of radion-higgs mixing in the light of LHC data*, *JHEP* **10** (2013) 093, [[arXiv:1307.3765](#)].
- [39] P. Cox, A. D. Medina, T. S. Ray, and A. Spray, *Radion/Dilaton-Higgs Mixing Phenomenology in Light of the LHC*, *JHEP* **02** (2014) 032, [[arXiv:1311.3663](#)].
- [40] J. Cao, Y. He, P. Wu, M. Zhang, and J. Zhu, *Higgs Phenomenology in the Minimal Dilaton Model after Run I of the LHC*, *JHEP* **01** (2014) 150, [[arXiv:1311.6661](#)].
- [41] D.-W. Jung and P. Ko, *Higgs-dilaton(radion) system confronting the LHC Higgs data*, *Phys. Lett.* **B732** (2014) 364–372, [[arXiv:1401.5586](#)].
- [42] H. Kubota and M. Nojiri, *Prospect for a study of Randall-Sundrum models from Higgs bosons decay at future colliders*, *Phys. Rev.* **D90** (2014), no. 3 035006, [[arXiv:1404.3013](#)].
- [43] E. Boos, S. Keizerov, E. Rahmetov, and K. Svirina, *Higgs boson-radion similarity in production processes involving off-shell fermions*, *Phys. Rev.* **D90** (2014), no. 9 095026, [[arXiv:1409.2796](#)].
- [44] S. Bhattacharya, M. Frank, K. Huitu, U. Maitra, B. Mukhopadhyaya, and S. K. Rai, *Probing the light radion through diphotons at the Large Hadron Collider*, *Phys. Rev.* **D91** (2015) 016008, [[arXiv:1410.0396](#)].

- [45] P. R. Archer, M. Carena, A. Carmona, and M. Neubert, *Higgs Production and Decay in Models of a Warped Extra Dimension with a Bulk Higgs*, *JHEP* **01** (2015) 060, [[arXiv:1408.5406](#)].
- [46] A. Efrati, E. Kuflik, S. Nussinov, Y. Soreq, and T. Volansky, *Constraining the Higgs-Dilaton with LHC and Dark Matter Searches*, *Phys. Rev.* **D91** (2015), no. 5 055034, [[arXiv:1410.2225](#)].
- [47] E. E. Boos, V. E. Bunichev, M. A. Perfilov, M. N. Smolyakov, and I. P. Volobuev, *Higgs-radion mixing in stabilized brane world models*, *Phys. Rev.* **D92** (2015), no. 9 095010, [[arXiv:1505.05892](#)].
- [48] J. F. Gunion, M. Toharia, and J. D. Wells, *Precision electroweak data and the mixed Radion-Higgs sector of warped extra dimensions*, *Phys. Lett.* **B585** (2004) 295–306, [[hep-ph/0311219](#)].
- [49] **ATLAS, CMS Collaboration**, G. Aad et al., *Measurements of the Higgs boson production and decay rates and constraints on its couplings from a combined ATLAS and CMS analysis of the LHC pp collision data at  $\sqrt{s} = 7$  and 8 TeV*, *JHEP* **08** (2016) 045, [[arXiv:1606.02266](#)].
- [50] **CMS Collaboration**, C. Collaboration, *Updated measurements of Higgs boson production in the diphoton decay channel at  $\sqrt{s} = 13$  TeV in pp collisions at CMS.*, CMS-PAS-HIG-16-020.
- [51] **ATLAS Collaboration**, T. A. collaboration, *Measurement of fiducial, differential and production cross sections in the  $H \rightarrow \gamma\gamma$  decay channel with  $13.3 \text{ fb}^{-1}$  of 13 TeV proton-proton collision data with the ATLAS detector*, ATLAS-CONF-2016-067.
- [52] **CMS Collaboration**, C. Collaboration, *Measurements of properties of the Higgs boson decaying into four leptons in pp collisions at  $\sqrt{s} = 13$  TeV*, CMS-PAS-HIG-16-041.
- [53] **ATLAS Collaboration**, T. A. collaboration, *Search for the Standard Model Higgs boson produced in association with a vector boson and decaying to a  $b\bar{b}$  pair in pp collisions at 13 TeV using the ATLAS detector*, ATLAS-CONF-2016-091.
- [54] **CMS Collaboration**, V. Khachatryan et al., *Search for diphoton resonances in the mass range from 150 to 850 GeV in pp collisions at  $\sqrt{s} = 8$  TeV*, *Phys. Lett.* **B750** (2015) 494–519, [[arXiv:1506.02301](#)].
- [55] **ATLAS Collaboration**, T. A. collaboration, *Search for scalar diphoton resonances with  $15.4 \text{ fb}^{-1}$  of data collected at  $\sqrt{s}=13$  TeV in 2015 and 2016 with the ATLAS detector*, ATLAS-CONF-2016-059.
- [56] **CMS Collaboration**, C. Collaboration, *Search for resonant production of high mass photon pairs using  $12.9 \text{ fb}^{-1}$  of proton-proton collisions at  $\sqrt{s} = 13$  TeV and combined interpretation of searches at 8 and 13 TeV*, CMS-PAS-EXO-16-027.
- [57] **ATLAS Collaboration**, G. Aad et al., *Search for a high-mass Higgs boson decaying to a W boson pair in pp collisions at  $\sqrt{s} = 8$  TeV with the ATLAS detector*, *JHEP* **01** (2016) 032, [[arXiv:1509.00389](#)].

- [58] **CMS** Collaboration, V. Khachatryan et al., *Search for a Higgs boson in the mass range from 145 to 1000 GeV decaying to a pair of W or Z bosons*, *JHEP* **10** (2015) 144, [[arXiv:1504.00936](#)].
- [59] **ATLAS** Collaboration, T. A. collaboration, *Search for diboson resonance production in the  $lvqq$  final state using  $pp$  collisions at  $\sqrt{s} = 13$  TeV with the ATLAS detector at the LHC*, ATLAS-CONF-2016-062.
- [60] **CMS** Collaboration, C. Collaboration, *Search for high mass Higgs to WW with fully leptonic decays using 2015 data*, CMS-PAS-HIG-16-023.
- [61] **ATLAS** Collaboration, G. Aad et al., *Search for an additional, heavy Higgs boson in the  $H \rightarrow ZZ$  decay channel at  $\sqrt{s} = 8$  TeV in  $pp$  collision data with the ATLAS detector*, *Eur. Phys. J.* **C76** (2016), no. 1 45, [[arXiv:1507.05930](#)].
- [62] **ATLAS** Collaboration, T. A. collaboration, *Study of the Higgs boson properties and search for high-mass scalar resonances in the  $H \rightarrow ZZ^* \rightarrow 4\ell$  decay channel at  $\sqrt{s} = 13$  TeV with the ATLAS detector*, ATLAS-CONF-2016-079.
- [63] **CMS** Collaboration, C. Collaboration, *Measurements of properties of the Higgs boson and search for an additional resonance in the four-lepton final state at  $\sqrt{s} = 13$  TeV*, CMS-PAS-HIG-16-033.
- [64] **ATLAS** Collaboration, G. Aad et al., *Search for neutral Higgs bosons of the minimal supersymmetric standard model in  $pp$  collisions at  $\sqrt{s} = 8$  TeV with the ATLAS detector*, *JHEP* **11** (2014) 056, [[arXiv:1409.6064](#)].
- [65] **CMS** Collaboration, C. Collaboration, *Search for additional neutral Higgs bosons decaying to a pair of tau leptons in  $pp$  collisions at  $\sqrt{s} = 7$  and 8 TeV*, CMS-PAS-HIG-14-029.
- [66] **ATLAS** Collaboration, T. A. collaboration, *Search for Minimal Supersymmetric Standard Model Higgs Bosons  $H/A$  in the  $\tau\tau$  final state in up to  $13.3 \text{ fb}^{-1}$  of  $pp$  collisions at  $\sqrt{s} = 13$  TeV with the ATLAS Detector*, ATLAS-CONF-2016-085.
- [67] **CMS** Collaboration, C. Collaboration, *Search for a neutral MSSM Higgs boson decaying into  $\tau\tau$  at 13 TeV*, CMS-PAS-HIG-16-006.
- [68] **ATLAS** Collaboration, G. Aad et al., *Search For Higgs Boson Pair Production in the  $\gamma\gamma b\bar{b}$  Final State using  $pp$  Collision Data at  $\sqrt{s} = 8$  TeV from the ATLAS Detector*, *Phys. Rev. Lett.* **114** (2015), no. 8 081802, [[arXiv:1406.5053](#)].
- [69] **ATLAS** Collaboration, G. Aad et al., *Search for Higgs boson pair production in the  $b\bar{b}b\bar{b}$  final state from  $pp$  collisions at  $\sqrt{s} = 8$  TeV with the ATLAS detector*, *Eur. Phys. J.* **C75** (2015), no. 9 412, [[arXiv:1506.00285](#)].
- [70] **ATLAS** Collaboration, G. Aad et al., *Searches for Higgs boson pair production in the  $hh \rightarrow b\bar{b}\tau\tau, \gamma\gamma WW^*, \gamma\gamma b\bar{b}, b\bar{b}b\bar{b}$  channels with the ATLAS detector*, *Phys. Rev.* **D92** (2015) 092004, [[arXiv:1509.04670](#)].

- [71] **CMS** Collaboration, V. Khachatryan et al., *Search for resonant pair production of Higgs bosons decaying to two bottom quark-antiquark pairs in proton-proton collisions at 8 TeV*, *Phys. Lett.* **B749** (2015) 560–582, [[arXiv:1503.04114](#)].
- [72] **CMS** Collaboration, V. Khachatryan et al., *Search for two Higgs bosons in final states containing two photons and two bottom quarks in proton-proton collisions at 8 TeV*, *Phys. Rev.* **D94** (2016), no. 5 052012, [[arXiv:1603.06896](#)].
- [73] **CMS** Collaboration, C. Collaboration, *Model independent search for Higgs boson pair production in the  $b\bar{b}\tau^+\tau^-$  final state*, CMS-PAS-HIG-15-013.
- [74] **ATLAS** Collaboration, T. A. collaboration, *Search for Higgs boson pair production in the  $b\bar{b}\gamma\gamma$  final state using pp collision data at  $\sqrt{s} = 13$  TeV with the ATLAS detector*, ATLAS-CONF-2016-004.
- [75] **ATLAS** Collaboration, T. A. collaboration, *Search for pair production of Higgs bosons in the  $b\bar{b}b\bar{b}$  final state using proton-proton collisions at  $\sqrt{s} = 13$  TeV with the ATLAS detector*, ATLAS-CONF-2016-017.
- [76] **CMS** Collaboration, C. Collaboration, *Search for resonant pair production of Higgs bosons decaying to two bottom quark-antiquark pairs in proton-proton collisions at 13 TeV*, CMS-PAS-HIG-16-002.
- [77] **CMS** Collaboration, C. Collaboration, *Search for  $H(bb)H(\gamma\gamma)$  decays at 13TeV*, CMS-PAS-HIG-16-032.
- [78] **CMS** Collaboration, C. Collaboration, *Search for pair production of Higgs bosons in the two tau leptons and two bottom quarks final state using proton-proton collisions at  $\sqrt{s} = 13$  TeV*, CMS-PAS-HIG-17-002.
- [79] **CMS** Collaboration, C. Collaboration, *Search for a narrow heavy decaying to bottom quark pairs in the 13 TeV data sample*, CMS-PAS-HIG-16-025.
- [80] **ATLAS** Collaboration, T. A. collaboration, *Search for pair production of Higgs bosons in the  $b\bar{b}b\bar{b}$  final state using proton-proton collisions at  $\sqrt{s} = 13$  TeV with the ATLAS detector*, ATLAS-CONF-2016-049.
- [81] M. Frank, K. Huitu, U. Maitra, and M. Patra, *Probing Higgs-radion mixing in warped models through complementary searches at the LHC and the ILC*, *Phys. Rev.* **D94** (2016), no. 5 055016, [[arXiv:1606.07689](#)].
- [82] *Beyond Standard Model Higgs boson searches at a High-Luminosity LHC with ATLAS*, Tech. Rep. ATL-PHYS-PUB-2013-016, CERN, Geneva, Oct, 2013.
- [83] **CMS** Collaboration, C. Collaboration, *2HDM Neutral Higgs Future Analysis Studies*, CMS-PAS-FTR-13-024.
- [84] M. Toharia, *Higgs-Radion Mixing with Enhanced Di-Photon Signal*, *Phys. Rev.* **D79** (2009) 015009, [[arXiv:0809.5245](#)].

- [85] A. Ahmed, B. M. Dillon, B. Grzadkowski, J. F. Gunion, and Y. Jiang, *Implications of the absence of high-mass radion signals*, *Phys. Rev.* **D95** (2017), no. 9 095019, [[arXiv:1512.05771](#)].
- [86] D. Bardhan, D. Bhatia, A. Chakraborty, U. Maitra, S. Raychaudhuri, and T. Samui, *Radion Candidate for the LHC Diphoton Resonance*, [arXiv:1512.06674](#).
- [87] **ATLAS** Collaboration, T. A. collaboration, *Search for resonances decaying to photon pairs in  $3.2 \text{ fb}^{-1}$  of  $pp$  collisions at  $\sqrt{s} = 13 \text{ TeV}$  with the ATLAS detector*, ATLAS-CONF-2015-081.
- [88] **CMS** Collaboration, C. Collaboration, *Search for new physics in high mass diphoton events in proton-proton collisions at  $13\text{TeV}$* , CMS-PAS-EXO-15-004.
- [89] **ATLAS** Collaboration, G. Aad et al., *Combined search for the Standard Model Higgs boson using up to  $4.9 \text{ fb}^{-1}$  of  $pp$  collision data at  $\sqrt{s} = 7 \text{ TeV}$  with the ATLAS detector at the LHC*, *Phys. Lett.* **B710** (2012) 49–66, [[arXiv:1202.1408](#)].
- [90] **CMS** Collaboration, S. Chatrchyan et al., *Combined results of searches for the standard model Higgs boson in  $pp$  collisions at  $\sqrt{s} = 7 \text{ TeV}$* , *Phys. Lett.* **B710** (2012) 26–48, [[arXiv:1202.1488](#)].
- [91] **ATLAS** Collaboration, G. Aad et al., *Observation of a new particle in the search for the Standard Model Higgs boson with the ATLAS detector at the LHC*, *Phys. Lett.* **B716** (2012) 1–29, [[arXiv:1207.7214](#)].
- [92] **CMS** Collaboration, S. Chatrchyan et al., *Observation of a new boson at a mass of  $125 \text{ GeV}$  with the CMS experiment at the LHC*, *Phys. Lett.* **B716** (2012) 30–61, [[arXiv:1207.7235](#)].
- [93] L. D. Landau, *On the angular momentum of a system of two photons*, *Dokl. Akad. Nauk Ser. Fiz.* **60** (1948), no. 2 207–209.
- [94] C.-N. Yang, *Selection Rules for the Dematerialization of a Particle Into Two Photons*, *Phys. Rev.* **77** (1950) 242–245.
- [95] F. Englert and R. Brout, *Broken Symmetry and the Mass of Gauge Vector Mesons*, *Phys. Rev. Lett.* **13** (1964) 321–323. [,157(1964)].
- [96] G. S. Guralnik, C. R. Hagen, and T. W. B. Kibble, *Global Conservation Laws and Massless Particles*, *Phys. Rev. Lett.* **13** (1964) 585–587. [,162(1964)].
- [97] P. W. Higgs, *Broken symmetries, massless particles and gauge fields*, *Phys. Lett.* **12** (1964) 132–133.
- [98] P. W. Higgs, *Broken Symmetries and the Masses of Gauge Bosons*, *Phys. Rev. Lett.* **13** (1964) 508–509. [,160(1964)].
- [99] R. N. Mohapatra and J. C. Pati, *A Natural Left-Right Symmetry*, *Phys. Rev.* **D11** (1975) 2558.

- [100] G. Senjanovic and R. N. Mohapatra, *Exact Left-Right Symmetry and Spontaneous Violation of Parity*, *Phys. Rev.* **D12** (1975) 1502.
- [101] J. C. Pati and A. Salam, *Lepton Number as the Fourth Color*, *Phys. Rev.* **D10** (1974) 275–289. [Erratum: *Phys. Rev.*D11,703(1975)].
- [102] J. C. Pati and A. Salam, *Unified Lepton-Hadron Symmetry and a Gauge Theory of the Basic Interactions*, *Phys. Rev.* **D8** (1973) 1240–1251.
- [103] H. Georgi and S. L. Glashow, *Unity of All Elementary Particle Forces*, *Phys. Rev. Lett.* **32** (1974) 438–441.
- [104] R. D. Peccei and H. R. Quinn, *CP Conservation in the Presence of Instantons*, *Phys. Rev. Lett.* **38** (1977) 1440–1443. [,328(1977)].
- [105] A. H. Guth, *The Inflationary Universe: A Possible Solution to the Horizon and Flatness Problems*, *Phys. Rev.* **D23** (1981) 347–356. [Adv. Ser. Astrophys. Cosmol.3,139(1987)].
- [106] J. F. Gunion, H. E. Haber, G. L. Kane, and S. Dawson, *The Higgs Hunter’s Guide*, *Front. Phys.* **80** (2000) 1–404.
- [107] J. Jaeckel, M. Jankowiak, and M. Spannowsky, *LHC probes the hidden sector*, *Phys. Dark Univ.* **2** (2013) 111–117, [[arXiv:1212.3620](#)].
- [108] A. Angelescu, A. Djouadi, and G. Moreau, *Scenarii for interpretations of the LHC diphoton excess: two Higgs doublets and vector-like quarks and leptons*, *Phys. Lett.* **B756** (2016) 126–132, [[arXiv:1512.04921](#)].
- [109] R. S. Gupta, S. Jäger, Y. Kats, G. Perez, and E. Stamou, *Interpreting a 750 GeV Diphoton Resonance*, *JHEP* **07** (2016) 145, [[arXiv:1512.05332](#)].
- [110] S. Di Chiara, L. Marzola, and M. Raidal, *First interpretation of the 750 GeV diphoton resonance at the LHC*, *Phys. Rev.* **D93** (2016), no. 9 095018, [[arXiv:1512.04939](#)].
- [111] D. Buttazzo, A. Greljo, and D. Marzocca, *Knocking on new physics door with a scalar resonance*, *Eur. Phys. J.* **C76** (2016), no. 3 116, [[arXiv:1512.04929](#)].
- [112] D. Bečirević, E. Bertuzzo, O. Sumensari, and R. Zukanovich Funchal, *Can the new resonance at LHC be a CP-Odd Higgs boson?*, *Phys. Lett.* **B757** (2016) 261–267, [[arXiv:1512.05623](#)].
- [113] E. Megias, O. Pujolas, and M. Quiros, *On dilatons and the LHC diphoton excess*, *JHEP* **05** (2016) 137, [[arXiv:1512.06106](#)].
- [114] A. Pilaftsis, *Diphoton Signatures from Heavy Axion Decays at the CERN Large Hadron Collider*, *Phys. Rev.* **D93** (2016), no. 1 015017, [[arXiv:1512.04931](#)].
- [115] T. Higaki, K. S. Jeong, N. Kitajima, and F. Takahashi, *The QCD Axion from Aligned Axions and Diphoton Excess*, *Phys. Lett.* **B755** (2016) 13–16, [[arXiv:1512.05295](#)].
- [116] S. D. McDermott, P. Meade, and H. Ramani, *Singlet Scalar Resonances and the Diphoton Excess*, *Phys. Lett.* **B755** (2016) 353–357, [[arXiv:1512.05326](#)].

- [117] J. Ellis, S. A. R. Ellis, J. Quevillon, V. Sanz, and T. You, *On the Interpretation of a Possible  $\sim 750$  GeV Particle Decaying into  $\gamma\gamma$* , *JHEP* **03** (2016) 176, [[arXiv:1512.05327](#)].
- [118] B. Dutta, Y. Gao, T. Ghosh, I. Gogoladze, and T. Li, *Interpretation of the diphoton excess at CMS and ATLAS*, *Phys. Rev.* **D93** (2016), no. 5 055032, [[arXiv:1512.05439](#)].
- [119] A. Kobakhidze, F. Wang, L. Wu, J. M. Yang, and M. Zhang, *750 GeV diphoton resonance in a top and bottom seesaw model*, *Phys. Lett.* **B757** (2016) 92–96, [[arXiv:1512.05585](#)].
- [120] W. Chao, R. Huo, and J.-H. Yu, *The minimal scalar-vectorlike top interpretation of the diphoton excess*, *Eur. Phys. J. Plus* **132** (2017), no. 1 27, [[arXiv:1512.05738](#)].
- [121] S. Fichtel, G. von Gersdorff, and C. Royon, *Scattering light by light at 750 GeV at the LHC*, *Phys. Rev.* **D93** (2016), no. 7 075031, [[arXiv:1512.05751](#)].
- [122] P. Cox, A. D. Medina, T. S. Ray, and A. Spray, *Implications of diphoton searches for a Radion in the Bulk-Higgs Scenario*, *Int. J. Mod. Phys.* **A32** (2017), no. 04 1750020, [[arXiv:1512.05618](#)].
- [123] A. Falkowski, O. Slone, and T. Volansky, *Phenomenology of a 750 GeV Singlet*, *JHEP* **02** (2016) 152, [[arXiv:1512.05777](#)].
- [124] M. Low, A. Tesi, and L.-T. Wang, *A pseudoscalar decaying to photon pairs in the early LHC Run 2 data*, *JHEP* **03** (2016) 108, [[arXiv:1512.05328](#)].
- [125] A. Alves, A. G. Dias, and K. Sinha, *The 750 GeV S-cion: Where else should we look for it?*, *Phys. Lett.* **B757** (2016) 39–46, [[arXiv:1512.06091](#)].
- [126] R. Benbrik, C.-H. Chen, and T. Nomura, *Higgs singlet boson as a diphoton resonance in a vectorlike quark model*, *Phys. Rev.* **D93** (2016), no. 5 055034, [[arXiv:1512.06028](#)].
- [127] E. Gabrielli, K. Kannike, B. Mele, M. Raidal, C. Spethmann, and H. Veermäe, *A SUSY Inspired Simplified Model for the 750 GeV Diphoton Excess*, *Phys. Lett.* **B756** (2016) 36–41, [[arXiv:1512.05961](#)].
- [128] S. Matsuzaki and K. Yamawaki, *750 GeV Diphoton Signal from One-Family Walking Technipion*, *Mod. Phys. Lett.* **A31** (2016), no. 17 1630016, [[arXiv:1512.05564](#)].
- [129] K. Harigaya and Y. Nomura, *Composite Models for the 750 GeV Diphoton Excess*, *Phys. Lett.* **B754** (2016) 151–156, [[arXiv:1512.04850](#)].
- [130] Y. Bai, J. Berger, and R. Lu, *750 GeV dark pion: Cousin of a dark G-parity odd WIMP*, *Phys. Rev.* **D93** (2016), no. 7 076009, [[arXiv:1512.05779](#)].
- [131] E. Molinaro, F. Sannino, and N. Vignaroli, *Minimal Composite Dynamics versus Axion Origin of the Diphoton excess*, *Mod. Phys. Lett.* **A31** (2016), no. 26 1650155, [[arXiv:1512.05334](#)].

- [132] J. S. Kim, J. Reuter, K. Rolbiecki, and R. Ruiz de Austri, *A resonance without resonance: scrutinizing the diphoton excess at 750 GeV*, *Phys. Lett.* **B755** (2016) 403–408, [[arXiv:1512.06083](#)].
- [133] R. Franceschini, G. F. Giudice, J. F. Kamenik, M. McCullough, A. Pomarol, R. Rattazzi, M. Redi, F. Riva, A. Strumia, and R. Torre, *What is the  $\gamma\gamma$  resonance at 750 GeV?*, *JHEP* **03** (2016) 144, [[arXiv:1512.04933](#)].
- [134] Y. Mambrini, G. Arcadi, and A. Djouadi, *The LHC diphoton resonance and dark matter*, *Phys. Lett.* **B755** (2016) 426–432, [[arXiv:1512.04913](#)].
- [135] M. Backovic, A. Mariotti, and D. Redigolo, *Di-photon excess illuminates Dark Matter*, *JHEP* **03** (2016) 157, [[arXiv:1512.04917](#)].
- [136] R. Martinez, F. Ochoa, and C. F. Sierra, *Diphoton decay for a 750 GeV scalar boson in a  $U(1)_X$  model*, *Nucl. Phys.* **B913** (2016) 64–78, [[arXiv:1512.05617](#)].
- [137] Y. Nakai, R. Sato, and K. Tobioka, *Footprints of New Strong Dynamics via Anomaly and the 750 GeV Diphoton*, *Phys. Rev. Lett.* **116** (2016), no. 15 151802, [[arXiv:1512.04924](#)].
- [138] J. M. No, V. Sanz, and J. Setford, *See-saw composite Higgs model at the LHC: Linking naturalness to the 750 GeV diphoton resonance*, *Phys. Rev.* **D93** (2016), no. 9 095010, [[arXiv:1512.05700](#)].
- [139] C. Petersson and R. Torre, *750 GeV Diphoton Excess from the Goldstino Superpartner*, *Phys. Rev. Lett.* **116** (2016), no. 15 151804, [[arXiv:1512.05333](#)].
- [140] S. V. Demidov and D. S. Gorbunov, *On sgoldstino interpretation of the diphoton excess*, *JETP Lett.* **103** (2016), no. 4 219–222, [[arXiv:1512.05723](#)]. [*Pisma Zh. Eksp. Teor. Fiz.*103,no.4,241(2016)].
- [141] B. Bellazzini, R. Franceschini, F. Sala, and J. Serra, *Goldstones in Diphotons*, *JHEP* **04** (2016) 072, [[arXiv:1512.05330](#)].
- [142] L. M. Carpenter, R. Colburn, and J. Goodman, *Supersoft SUSY models and the 750 GeV diphoton excess, beyond effective operators*, *Phys. Rev.* **D94** (2016), no. 1 015016, [[arXiv:1512.06107](#)].
- [143] C. Csáki, J. Hubisz, and J. Terning, *Minimal model of a diphoton resonance: Production without gluon couplings*, *Phys. Rev.* **D93** (2016), no. 3 035002, [[arXiv:1512.05776](#)].
- [144] S. Knapen, T. Melia, M. Papucci, and K. Zurek, *Rays of light from the LHC*, *Phys. Rev.* **D93** (2016), no. 7 075020, [[arXiv:1512.04928](#)].
- [145] D. Curtin and C. B. Verhaaren, *Quirky Explanations for the Diphoton Excess*, *Phys. Rev.* **D93** (2016), no. 5 055011, [[arXiv:1512.05753](#)].
- [146] L. Bian, N. Chen, D. Liu, and J. Shu, *Hidden confining world on the 750 GeV diphoton excess*, *Phys. Rev.* **D93** (2016), no. 9 095011, [[arXiv:1512.05759](#)].
- [147] J. Bernon and C. Smith, *Could the width of the diphoton anomaly signal a three-body decay?*, *Phys. Lett.* **B757** (2016) 148–153, [[arXiv:1512.06113](#)].

- [148] J. Chakraborty, A. Choudhury, P. Ghosh, S. Mondal, and T. Srivastava, *Di-photon resonance around 750 GeV: shedding light on the theory underneath*, [arXiv:1512.05767](#).
- [149] D. Aloni, K. Blum, A. Dery, A. Efrati, and Y. Nir, *On a possible large width 750 GeV diphoton resonance at ATLAS and CMS*, *JHEP* **08** (2016) 017, [[arXiv:1512.05778](#)].
- [150] **ATLAS** Collaboration, G. Aad et al., *Search for new phenomena in the dijet mass distribution using  $p - p$  collision data at  $\sqrt{s} = 8$  TeV with the ATLAS detector*, *Phys. Rev. D* **91** (2015), no. 5 052007, [[arXiv:1407.1376](#)].
- [151] **LHC Higgs Cross Section Working Group** Collaboration.  
<http://twiki.cern.ch/twiki/bin/view/LHCPhysics/LHCHXSWG>.
- [152] Q.-H. Cao, Y. Liu, K.-P. Xie, B. Yan, and D.-M. Zhang, *A Boost Test of Anomalous Diphoton Resonance at the LHC*, [arXiv:1512.05542](#).
- [153] P. Agrawal, J. Fan, B. Heidenreich, M. Reece, and M. Strassler, *Experimental Considerations Motivated by the Diphoton Excess at the LHC*, *JHEP* **06** (2016) 082, [[arXiv:1512.05775](#)].
- [154] **CMS** Collaboration, S. Chatrchyan et al., *Measurement of Higgs boson production and properties in the  $WW$  decay channel with leptonic final states*, *JHEP* **01** (2014) 096, [[arXiv:1312.1129](#)].
- [155] G. F. Giudice, R. Rattazzi, and J. D. Wells, *Quantum gravity and extra dimensions at high-energy colliders*, *Nucl. Phys.* **B544** (1999) 3–38, [[hep-ph/9811291](#)].
- [156] E. A. Mirabelli, M. Perelstein, and M. E. Peskin, *Collider signatures of new large space dimensions*, *Phys. Rev. Lett.* **82** (1999) 2236–2239, [[hep-ph/9811337](#)].
- [157] **ATLAS** Collaboration, M. Aaboud et al., *Search for dark matter and other new phenomena in events with an energetic jet and large missing transverse momentum using the ATLAS detector*, *JHEP* **01** (2018) 126, [[arXiv:1711.03301](#)].
- [158] **CMS** Collaboration, A. M. Sirunyan et al., *Search for new physics in final states with an energetic jet or a hadronically decaying  $W$  or  $Z$  boson and transverse momentum imbalance at  $\sqrt{s} = 13$  TeV*, *Phys. Rev. D* **97** (2018), no. 9 092005, [[arXiv:1712.02345](#)].
- [159] D. E. Kaplan, K. Rehermann, M. D. Schwartz, and B. Tweedie, *Top Tagging: A Method for Identifying Boosted Hadronically Decaying Top Quarks*, *Phys. Rev. Lett.* **101** (2008) 142001, [[arXiv:0806.0848](#)].
- [160] J. A. M. Vermaseren, *New features of FORM*, [math-ph/0010025](#).
- [161] J. Pumplin, D. R. Stump, J. Huston, H. L. Lai, P. M. Nadolsky, and W. K. Tung, *New generation of parton distributions with uncertainties from global QCD analysis*, *JHEP* **07** (2002) 012, [[hep-ph/0201195](#)].
- [162] P. Nason, S. Dawson, and R. K. Ellis, *The Total Cross-Section for the Production of Heavy Quarks in Hadronic Collisions*, *Nucl. Phys.* **B303** (1988) 607–633.

- [163] **Linear Collider** Collaboration, L. Evans and S. Michizono, *The International Linear Collider Machine Staging Report 2017*, [arXiv:1711.00568](https://arxiv.org/abs/1711.00568).
- [164] M. Aicheler, P. Burrows, M. Draper, T. Garvey, P. Lebrun, K. Peach, N. Phinney, H. Schmickler, D. Schulte, and N. Toge, *A Multi-TeV Linear Collider Based on CLIC Technology*, .